Synchrony of carbon cycle fluctuations, volcanism and orbital forcing during the Early Cretaceous

Mathieu Martinez, Beatriz Aguirre-Urreta, Guillaume Dera, Marina Lescano, Julieta Omarini, Maisa Tunik, Luis O'Dogherty, Roque Aguado, Miguel Company, Stéphane Bodin

Synchrony of carbon cycle fluctuations, volcanism and orbital forcing during the Early Cretaceous

Mathieu Martinez, Beatriz Aguirre-Urreta, Guillaume Dera, Marina Lescano, Julieta Omarini, Maisa Tunik, Luis O'Dogherty, Roque Aguado, Miguel Company, Stéphane Bodin

PII: S0012-8252(23)00045-4

DOI: https://doi.org/10.1016/j.earscirev.2023.104356

Reference: EARTH 104356

To appear in: *Earth-Science Reviews*

Received date: 8 December 2021

Revised date: 7 February 2023

Accepted date: 8 February 2023

Please cite this article as: M. Martinez, B. Aguirre-Urreta, G. Dera, et al., Synchrony of carbon cycle fluctuations, volcanism and orbital forcing during the Early Cretaceous, *Earth-Science Reviews* (2023), https://doi.org/10.1016/j.earscirev.2023.104356

Synchrony of carbon cycle fluctuations, volcanism and orbital forcing during the Early Cretaceous

Mathieu Martinez[1*], Beatriz Aguirre-Urreta[2], Guillaume Dera[3], Marina Lescano[2], Julieta Omarini[4], Maisa Tunik[4], Luis O'Dogherty[5], Roque Aguado[6], Miguel Company[7], Stéphane Bodin[8]

[1]Univ Rennes, CNRS, Géosciences Rennes - UMR 6118, F-35000 Rennes, France

[2]Instituto de Estudios Andinos Don Pablo Groeber, CONICET & Universidad de Buenos Aires, Ciudad Universitaria, pabellón 2, 1428 Buenos Aires, Argentina

[3]GET, Université Paul Sabatier, CNRS UMR 5563, IRD, Toulouse, France

[4]Instituto de Investigación en Paleobiología y Geología, CONICET & Universidad de Río Negro, Sede Alto Valle, 8332 General Roca, Río Negro, Argentina

[5]Departamento Ciencias de la Tierra, Universidad de Cádiz, CASEM, 11510 Puerto Real, Spain

[6]Departamento de Geología y CEACTEMA, Universidad de Jaén, Campus Científico-Tecnológico de Linares, 23700 Linares, Spain

[7]Departamento de Estratigrafía y Paleontología, Universidad de Granada, 18002 Granada, Spain

[8]Department of Geoscience, Aarhus University, Høegh-Guldbergs Gade 2, 8000 Aarhus C, Denmark

[*]Corresponding author: mathieu.martinez@univ-rennes1.fr

Abstract

Episodes of Environmental Change (EECs) were times of accelerated hydrological cycle that punctuated the Early Cretaceous. Uncertainties in the geologic time scales however preclude full understanding of the onset, unfolding, and termination of EECs. Here, we reanalyze the hemipelagic sedimentary series from France and Spain from the Valanginian to the Barremian to provide a comprehensive and accurate time scale of the Valanginian–Barremian interval based on the stable 405-kyr eccentricity cycle. According to our astrochonologic framework, the Weissert Event started 134.56 ± 0.19 Ma, in perfect synchronicity with the peak of volcanic activity of the Paraná-Etendeka Large Igneous Province. On average, EECs show a pacing of 2.40 Myr from the Valanginian to the Barremian, in phase with detrital supply and carbon isotope variations from marine carbonates. Long eccentricity cycles were hence key parameters in the regulation of climate and carbon cycles in the Early Cretaceous through changes in the detrital and nutrient supply, oceanic fertilization, organic carbon storage and global sea level. A long obliquity forcing, at 1.2 Myr, is also observed through the studied interval in both the detrital and carbon-isotope ratios series, allowing the identification of long isotopic stages in the Early Cretaceous. Our study highlights a positive correlation between continental runoff and sea-level change, suggesting that glacio-eustasy, and not aquifer-eustasy, was the main driver of global-sea level fluctuations during the Early Cretaceous. We also demonstrate that the humid peak related to the Weissert Event is driven by the pacing of the long orbital cycles despite the emplacement of the Paraná-Etendeka province. Nevertheless, in comparison to other EECs of the Valanginian–Barremian, the Weissert Event appears as a singularly long event with stronger impact on climate and marine ecosystems compared to other EECs. We posit that this is a consequence of the concomitant effect of the emplacement of the Paraná-Etendeka province and the long orbital cycles.

1. Introduction

Dramatic Episodes of Environmental Changes (EECs) punctuated the Early Cretaceous period (Föllmi, 2012). According to Föllmi (2012), these EECs occurred at time of reinforced greenhouse climatic conditions, when an accelerated hydrological cycle led to higher levels of continental weathering, increase of primary productivity, and high amounts of organic carbon storage (Weissert et al., 1998; Bodin et al., 2009; Föllmi, 2012; Stein et al., 2012; Aguado et al., 2014; Duchamp-Alphonse et al., 2014; Mattioli et al., 2014). From the Valanginian to the Barremian stages (~137 to ~121 Ma; Gale et al., 2020), the documented EECs are the Weissert Event during the mid-Valanginian, the Faraoni Event at the end of the Hauterivian, the Mid-Barremian Event and the Taxy Event at the end of the Barremian (Föllmi, 2012; Fig. 1).

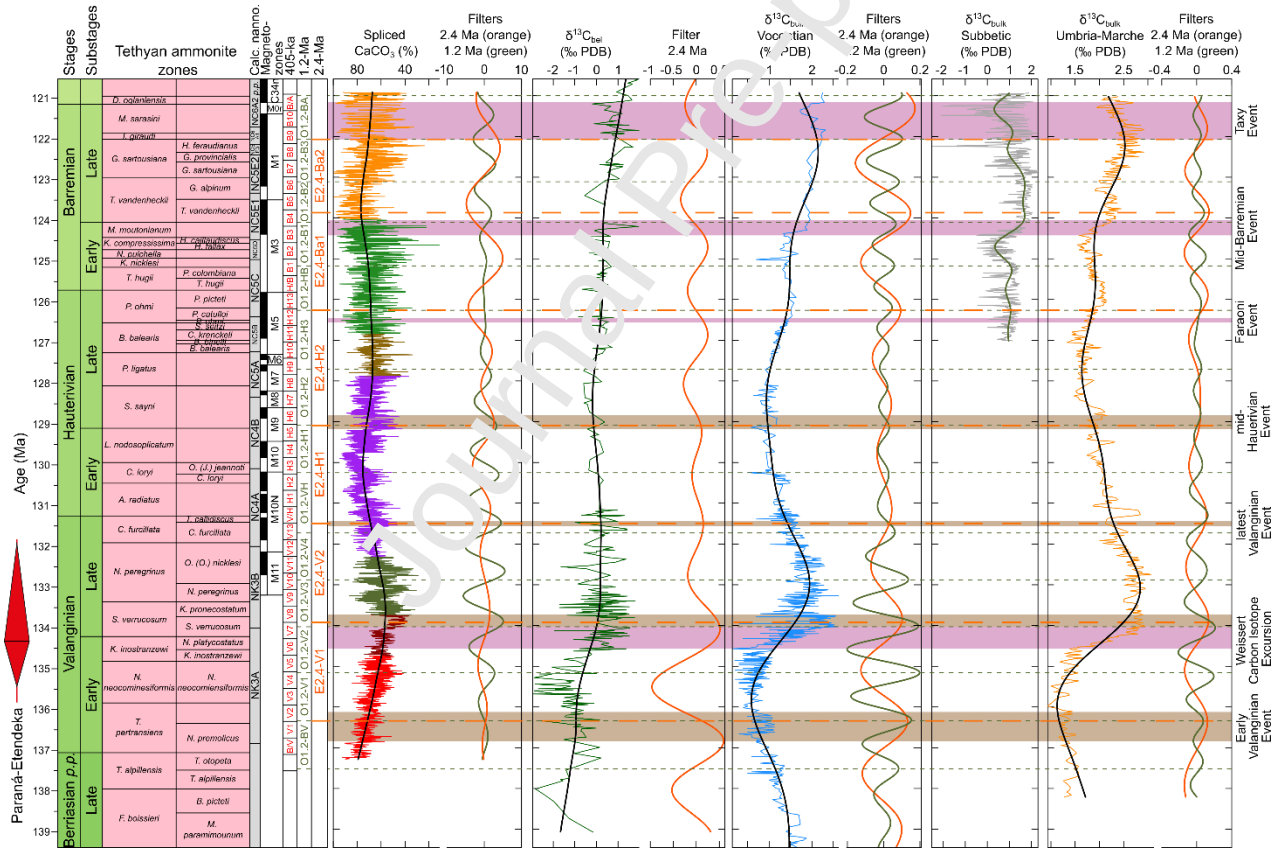

Fig. 1. Time scale calculated here of stages, substages, Tethyan ammonite zones, calcareous nannofossil zones, magnetochrons, orbital cycles, composite $CaCO_3$ series and various $\delta^{13}C_{carb}$ series

The Weissert Event is defined as a positive carbon-isotope excursion of +1.5 to +2 ‰ PDB amplitude in bulk carbonate, fossil shells and organic carbon, starting at the end of the Early Valanginian (*Karakaschiceras inostranzewi* Tethyan Ammonite Zone; Fig. 1) and culminating in the lower part of the Late Valanginian (*Saynoceras verrucosum* Tethyan Ammonite Zone), with worldwide expression (Cotillon and Rio, 1984; Lini et al., 1992; Weissert et al., 1998; Hennig et al., 1999; Erba et al., 2004; Gröcke et al., 2005; McArthur et al., 2007; Aguirre-Urreta et al., 2008; Gréselle et al., 2011; Kujau et al., 2012; Aguado et al., 2018; Cavalheiro et al., 2021). Carbon-isotope values remained high in the Late Valanginian and decreased slowly until the Early-Late Hauterivian transition (Hennig et al., 1999; Sprovieri et al., 2006; Aguirre-Urreta et al., 2019; Fig. 1). This event corresponds to the culmination of the neritic carbonate production crisis recorded in the peri-North Atlantic and Tethys oceans (Wortmann and Weissert, 2000), and associated to the drowning of carbonate platforms documented in the peri-Tethys area, spanning from the Late Valanginian to the Early Hauterivian (*S. verrucosum* to the *Crioceratites loryi* Tethyan ammonite zones; Föllmi et al., 2006). The beginning of this drowning event corresponds to a 2nd-order transgression, following a 2nd-order sea-level fall at the transition between the *Karakaschcieras inostranzewi* and the *S. verrucosum* Tethyan ammonite subzone, documented worldwide (Hardenbol et al., 1998; Gréselle and Pittet, 2010; Reboulet et al., 2003, 2022) and of several dozens of meters of amplitude (Ray et al., 2019). Despite the global expression of the carbon isotope excursion, no synchronous, thick black shale series is found in the Tethyan area, suggesting that (i) the burial of organic carbon occurred in continental areas (Westermann et al., 2010) or in high latitudes (Cavalheiro et al., 2021) and/or (ii) the positive carbon-isotope excursion also results in the demise of the peri-Tethys and North Atlantic carbonate platform, an important sink in ^{13}C (Westermann et al., 2010).

The culmination of the $\delta^{13}C$ values in the Upper Valanginian is associated to a global warming event, as reflected by TEX86 (Cavalheiro et al., 2021) and oxygen isotope data on bulk carbonate (Duchamp-Alphonse et al., 2007; Charbonnier et al., 2020), to a third-order maximum flooding (Hardenbol et al., 1998), to increased weathering and humid conditions, as reflected by increased kaolinite contents in the

Vocontian Basin and Umbria-Marche Basin (Fesneau, 2008; Duchamp-Alphonse et al., 2011; Westermann et al., 2013; Charbonnier et al., 2016, 2020), and palynological assemblages (Kujau et al., 2013). In pelagic settings, the culmination of the $\delta^{13}C$ values is also marked by an increase in fertilization of the water column, as indicated by the nannofossil assemblages in Tethys and Atlantic realms (Erba et al., 2004; Bornemann and Mutterlose, 2008; Duchamp-Alphonse et al., 2014; Mattioli et al., 2014).

The Faraoni event is a series of deposits rich in marine organic matter identified first in the Umbria-Marche Basin (Cecca et al., 1994). These deposits have been correlated through the western Tethys, thanks to ammonites and calcareous nannofossils (Baudin et al., 1999; Baudin, 2005; Baudin and Riquier, 2014). This event notably occurs at the transition between the *Pseudothurmannia ohmi* and *Pseudothurmania mortilleti* Tethyan ammonite subzones (Fig. 1). The last occurrence of calcareous nannofossil *Lithraphidites bollii* occurred during this event (Company et al., 2005; Sprovieri et al., 2006). The kaolinite content, calcareous nannofossil assemblages and organic matter geochemistry point to a maximum of weathering conditions (Moiroud et al., 2012), accompanied by increased fertilization of the water masses (Aguado et al., 2014) and increased primary productivity (Baudin et al., 2002), in a context of 2nd-order maximum flooding (Hardenbol et al., 1998). This event is also associated to a drowning event of the Helvetic platform, the Altmann Member (Bodin et al., 2006b), and in Turkey (Yilmaz et al., 2012), overlying an emersive surface (Godet et al., 2013). The Faraoni Event occurred within a trend toward increasing $\delta^{13}C$ values of bulk carbonate, starting in the *Crioceratites krenkeli* Tethyan ammonite subzone and culminating in the *Pseudothurmannia catulloi* Tethyan ammonite subzone, with an amplitude ranging from +0.3 to +0.5 ‰ PDB (Godet et al., 2006; Aguado et al., 2014).

The Mid-Barremian Event is a 1 ‰ PDB increase of bulk carbonate $\delta^{13}C$ values, first observed in the Umbria-Marche Basin at the early-late Barremian transition (Coccioni et al., 2003; Fig. 1), and then described in the Lower Saxony Basin (Malkoč and Mutterlose, 2010; Pauly et al., 2013), in Turkey (Yilmaz et al., 2012), in the Subbetic Domain (Aguado et al., 2014), and in Denmark (Rudra et al., 2021). The Mid-

Barremian Event lasted 0.4 Myr (Martinez et al., 2020a). Black shale deposits have been found in this interval in the Lower Saxony Basin (Hauptblättertorn Level; Mutterlose et al., 2009), Danish North Sea (Munk Marls; Rudra et al., 2021), Italy (Föllmi et al., 2012) and Turkey (Yilmaz et al., 2012). Calcareous nannofossil assemblages indicate increased fertilization of the water masses (Aguado et al., 2014; Wulff et al., 2020) and increased marine productivity (Rudra et al., 2021) in a context of increased temperatures (Mutterlose et al., 2009, 2010, 2012; Huck and Heimofer, 2021) and increased input of fresh water suggested in the Subbetic Domain and Lower Saxony Basin (Aguado et al., 2014; Mutterlose et al., 2014). The Mid-Barremian Event occurred in a context of 2nd-order maximum flooding interval (Hardenbol et al., 1998). In the Helvetic Platform, it corresponds to a second step of the Late Hauterivian-Early Barremian drowning event, marked by (i) a phosphatized hardground characterizing a sequence boundary, and (ii) then a backstepping of the carbonate platform characterizing a rapid sea-level rise (Godet et al., 2013).

The Taxy Levels were originally defined as black shale layers observed at the end of the Barremian series (*Martelites sarasini* Tethyan ammonite zone; Fig. 1) and used as a correlation marker in the Provence Basin (Moullade et al., 1998). This organic-rich marker bed is preceded by the drowning of the photozoan Urgonian platform and the interruption of its growth, replaced by the heterozoan facies of "Lower Orbitolina Beds" (Frau et al., 2020). Recent revision of the biostratigraphy in Cassis-la-Bédoule suggests that these environmental perturbations started in the *Imerites giraudi* Tethyan ammonite Zone and correlate to a 2nd-order maximum flooding interval (Hardenbol et al., 1998; Frau et al., 2020). Increase in the density of organic-rich layers have been documented in the Umbria-Marche Basin (Föllmi et al., 2012), in the Lower Saxony Basin (Mutterlose et al., 2009; Pauly et al., 2013) and in the Atlantic Ocean (Bralower et al., 1994). The event started with an increase in bulk $\delta^{13}C$ in the *I. giraudi* and lower part of *M. sarasini* zones with amplitudes of 0.4 ‰ PDB in the Subbetic Domain (Martinez et al., 2020a; Aguado et al., 2022) and 0.3 ‰ PDB in the Vocontian Basin (Godet et al., 2006). In the Umbria-Marche Basin, this trend encompasses the boundary between chrons M1n and M0r (Frau et al., 2018) and is recorded with an amplitude of +0.6 ‰ PDB (Stein et al., 2011; Aguado et al., 2022). The increase in bulk $\delta^{13}C$ values also

corresponds to a +4 ‰ PDB increase in organic matter $\delta^{13}C$ in the Provence Basin at Cassis-la-Bédoule (Stein et al. 2012). This increase in $\delta^{13}C$ values is immediately followed by a sharp decrease in $\delta^{13}C$ values recorded in bulk rock with an amplitude of 1.6 ‰ PDB in Cassis-la-Bédoule (Kuhnt et al., 1998), 0.8 ‰ PDB in the Subbetic Domain (Martinez et al., 2020a, Aguado et al., 2022), 0.5 ‰ PDB in the Vocontian Basin (Wissler et al., 2002; Godet et al., 2006) and 0.4 ‰ PDB in the Umbria-Marche Basin (Sprovieri et al., 2006; Stein et al., 2011). The end of this negative excursion corresponds to the boundary between M0r and C34n magnetochrons in the Umbria-Marche Basin, while it corresponds to the upper part of the *M. sarasini* Tethyan ammonite zone in Cassis-la-Bédoule and the Subbetic Domain (Frau et al., 2018; Aguado et al., 2022). In the Cassis-Bedoule section, the negative excursion observed in bulk carbonate $\delta^{13}C$ values is not observed in organic matter $\delta^{13}C$. This dichotomy was interpreted by Stein et al. (2012) as the result of increased burial of continental organic matter in this section by increased riverine fresh water supply during the Taxy event. This agrees with both kaolinite and TEX86 proxies that indicate warmer climate and increased levels of continental weathering during this event (Stein et al., 2012; Huck and Heimofer, 2021). Increased fertilization of the water masses is documented around chron M0r in eastern Atlantic and in the Subbetic Domain (Tremolada et al., 2006; Aguado et al., 2022).

These episodes of environmental changes are thus associated to increased bulk $\delta^{13}C$, at least at the beginning of these events, increased temperatures, continental weathering and supply of fresh waters in Boreal and Tethyan basins and increased in trophic conditions, leading to fertilization of the water masses. They are also accompanied by 2nd-order sea level increases, after a phase of sea-level decrease. Rapid sea-level and nutrification increases led to drowning of carbonate platforms or, at the end of the Barremian Stage, led to changes from photozoan to heterozoan facies in peri-Tethyan environments (Föllmi et al., 2006; Godet et al., 2013). Additional humid peaks and increase in trophic levels were documented from clay mineral, palynological and calcareous nannofossil assemblages in the earliest Valanginian (Morales et al., 2013; Kujau et al., 2013; Duchamp-Alphonse et al., 2014; Charbonnier et al., 2016), and in the Valanginian-Hauterivian transition (Kujau et al., 2013; Charbonnier et al., 2016). A drowning event, the

Lidernen episode, is also documented in the "middle" Hauterivian, from the *Lyticoceras nodosoplicatum* to the *Plesiospitidiscus ligatus* Tethyan ammonite zones (Föllmi et al., 1994; Godet, 2013). All these events also share the fact that they correspond to 2nd-order transgression documented by facies changes (Morales et al., 2013; Godet, 2013; Aguirre-Urreta et al., 2019), widespread marl formations or drownings on platforms (van de Schootbrugge et al., 2003; Godet et al., 2013; Morales et al., 2013; Pictet, 2021) and faunal migration patterns (Walter, 1996; Mutterlose and Bornemann, 2000).

If similarities can be observed between these events, the carbon isotope variations in the Weissert event appears of higher amplitude and much longer than in the other episodes of environmental changes. The forcing mechanisms leading to these carbon cycle and climate disturbances are still uncertain because of their heterogenous imprint on the sedimentary record. Of special importance here is that part of this lack of understanding results from a lack of global temporal calibrations of all climatic events at the resolution of Milankovitch cycles. The Milankovitch cycles correspond to the imprint of the quasiperiodic motions of the Earth's orbit and rotational axis on global climate over 10^4 to 10^6 years periods. The climatic precession (average period 130 Ma: 20.4 ± 0.4 kyr), the obliquity (main period 130 Ma: 38.4 ± 0.4 kyr) and the eccentricity cycles (periods: 405 kyr and *ca.* 100 kyr for the shortest periods) (Laskar et al., 2011; Waltham, 2015) modify the annual distribution in insolation at a given latitude which triggers pseudo-periodic climatic changes ultimately preserved in strata. The effect of the Earth's orbital eccentricity is not directly observed on the spectra of the insolation series as it modulates the amplitude of the precession cycles (e.g. Hinnov, 2018). Non-linearities in the climate and sedimentary systems nonetheless allow its direct observation in sedimentary series (Martinez, 2018). The identification of these quasi-periodic cycles in the sedimentary record provide accurate durations of geological times, also referred to orbital time scales or astrochronology. In strata of Mesozoic age, the period of the 405-kyr eccentricity cycle is known with the best accuracy and is preferred for astrochronology (Laskar et al., 2011). If anchored to radiometric ages, numerical ages of geological times and climatic events can be given with an accuracy of 0.1 Myr in the Mesozoic. This is the case for hemipelagic marl-limestone alternations recorded in Early Cretaceous series

which correspond to humid-arid cycles controlled by Earth orbital configuration (Cotillon et al., 1980; Reboulet et al., 2003; Moiroud et al., 2012). Under humid climate, increased detrital and nutrient inputs to basins induced meso- and eutrophic conditions in marine environments, decreased neritic carbonate productivity but increased pelagic carbonate productivity, leading to the deposit of marl beds. Under more arid conditions, neritic carbonate production and their export to basin increased under oligo- to mesotrophic conditions concomitant to decreased siliciclastic supply (Reboulet et al., 2003; Föllmi et al., 2006), leading to the deposit of carbonate beds. The sedimentary record of all the Milankovitch cycles can thus be identified through spectral analyses of the $CaCO_3$ content (Martinez et al., 2013, 2020a; Aguirre-Urreta et al., 2019). Magnetic Susceptibility (MS) and Gamma-Ray Total Count (GRTC) are useful proxies of $CaCO_3$ content in marl-limestone alternations as their measurements are precise, quick, non-destructive and inversely correlated to $CaCO_3$ (Martinez, 2018). The Valanginian and Barremian stages were entirely calibrated with the 405-kyr eccentricity cycle directly observed in MS, GRTC and $CaCO_3$ signals (Martinez et al., 2013; 2020a; Aguirre-Urreta et al., 2019). The record of this cycle is still missing in most of the Hauterivian part, which limits the accuracy of the orbital time scale and prevents from bridging the timing of the climatic events from the Valanginian to the Barremian.

Here, we propose to reassess the astrochronology of the Hauterivian series from the Vocontian Basin (France) and the Subbetic Domain (Spain) by analyzing the amplitude modulation of the precession cycles and extracting the 405-ka eccentricity cycle. The sections studied were accurately dated with thousands of ammonites and constitute reference sections of this time interval (Bulot et al., 1992; Hoedemaeker and Leereveld, 1995; Reboulet and Atrops, 1999; Company et al., 2005; Aguado et al., 2014; Aguirre-Urreta et al., 2019; Kenjo et al., 2021). This new astrochronology is then anchored to CA-ID-TIMS U-Pb ages measured in the Neuquén Basin (Argentina, Aguirre-Urreta et al., 2017). We also review and reassess the astrochronology of the Valanginian series from multiple sites of the Vocontian Basin. From this revised temporal framework and carbon-isotope data synthetized here, we propose a new correlation scheme between biozones and magnetozones from the Valanginian to the Barremian stages, in line with

radiometric data published elsewhere (Zhang et al., 2021). We also reappraise the numerical ages of the episodes of environmental changes and related humid peaks and compile detrital and carbon-isotope series to determine the respective roles of the volcanism and the long orbital cycles on the pacing and intensity of climatic events during the Early Cretaceous.

2. Geological settings

2.1. Subbetic Domain

The Subbetic Domain (Fig. 2) is one of the external units of the Betic Cordillera, in southern Spain (Martín-Chivelet et al., 2019). It constitutes a domain of hemipelagic deposits alternating between marl and mudstone to wackestone beds, separated from the neritic domain by a rifting phase starting in the Pliensbachian (Ruiz-Ortiz et al., 2004). During the Early Cretaceous, the Subbetic Domain was part of the northern Tethys margin and was located at a paleolatitude comprised between 20° and 30°N (Barrier et al., 2018). During the period, the basin experienced a transtensional tectonic phase related to the opening of the Gascogne Bay and the anti-clockwise rotation of the Iberian Plate (Vera et al., 2004). The Subbetic Domain presents a morphology of swells and troughs reflecting these successive tectonic phases. The data shown here are from three sections located in one of these troughs: Río Argos (38°04'15" N; 1°56'58" E), Arroyo Gilico (38°09′35" N; 1°40′41" W) and Barranco de Cavila (38°03′10"; N 1°53′20" W), all located in the Murcia Province (Fig. 2). The macrofauna in these sections is composed of ammonites, accompanied by scarce belemnites, gastropods, bivalves, brachiopods and irregular echinoids. The microfauna and flora are composed of calcareous nannofossils, radiolarians and foraminifers. The facies and fauna observed in these sections point to a deposit depth of several hundred metres (Hoedemaeker and Leereveld, 1995).

2.2. Vocontian Basin

The Vocontian Basin (Fig. 2) belongs to the external units located in western Alps. This is a domain of hemipelagic deposits alternating between carbonate-rich (mudstone and wackestone) and clay-rich deposits, surrounded by the carbonate platforms of Jura-Bas-Dauphiné to the North and Provence to the

South. The basin was surrounded to the west by the Vivarais detrital margin and was open to the east to the Tethys Ocean (Cotillon et al., 1980). The basin opened during the Early Jurassic during rifting phases related to the opening of the Valais Ocean (Lemoine et al., 1986). During the Early Cretaceous, tectonic activity was much reduced and consisted of transtensional movement related to the opening of Gascogne Bay (Graciansky and Lemoine, 1988; Homberg et al., 2013). Most of subsidence during the Valanginian-Hauterivian was caused by the thermal subsidence of the northern Tethyan margin as it cooled (Wilpshaar et al., 1997). During this time, the basin was located at a paleolatitude between 30 and 35°N (Barrier et al., 2018).

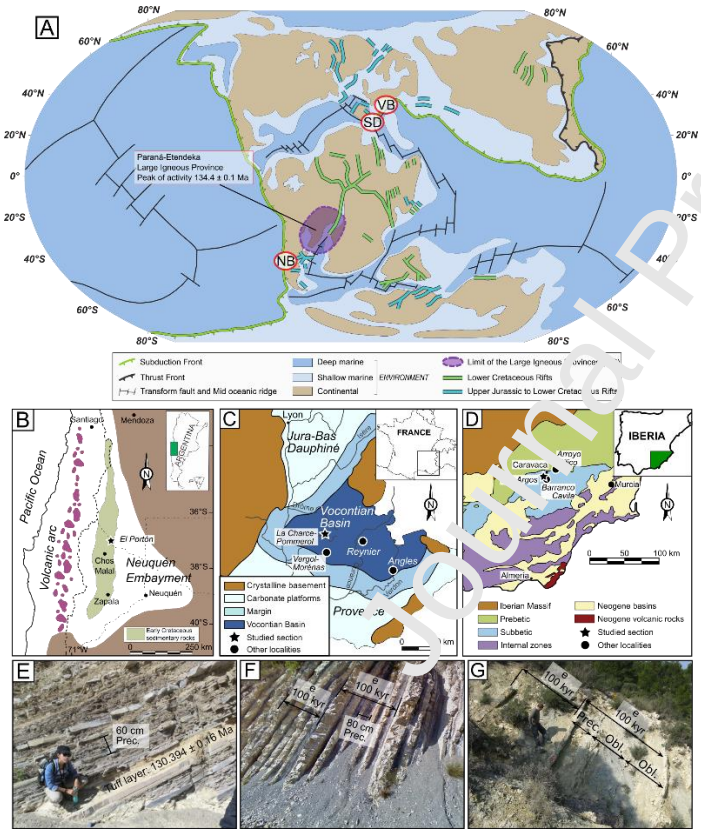

Fig. 2. A. Paleogeographic map of the Early Cretaceous with locations of the Late Jurassic and Early Cretaceous continental rifts (Frizon de Lamotte et al., 2015). Abbreviations: NB: Neuquén Basin, SD: Subbetic Domain, VB: Vocontian Basin. **B.** Map of the Neuquén Basin with location of the El Portón section. **C.** Map of the Vocontian Basin with location of the La Charce-Pommerol section and other sections mentioned. **D.** Map of the Betic Range with location of the Río Argos section and other mentioned

sections. **E.** Detail of the El Portón section showing the tuff layer dated within the marl-limestone alternations. **F.** Detail of the marl-limestone alternations of the la Charce section. **G.** Details of the marl-limestone alternations of the Río Argos section. Abbreviations: Prec.: Precession; Obl.: Obliquity.

2.3. Climatic and eustatic origins of the marl-limestone alternations

Clay mineral assemblages determined from marl-limestone alternations from the Vocontian Basin and the Subbetic Domain show that marl beds have higher kaolinite and illite contents, while limestone beds have higher smectite contents (Cotillon et al., 1980; Deconinck and Chamley, 1983; Moiroud et al., 2012; Giraud et al., 2013; Ghirardi et al., 2014; Martinez et al., 2020b; Figs. 3, 4). This feature has also been recognized in the Hauterivian-Barremian transition of the Lower Saxony Basin, in northern Germany (Mutterlose and Ruffell, 1999) and particularly verified in sections having experienced low level of burial diagenesis, showing these are primary fluctuations. Nannofossil abundances are systematically higher in marl beds than in limestone beds (Mutterlose and Ruffell, 1999; Gréselle et al., 2011; Giraud et al., 2013). Marl beds also shows mesotrophic assemblages while limestone beds show oligotrophic assemblages. All these data suggest that marl beds were deposited under more humid conditions than limestone beds. Increased detrital and nutrient supply during more humid times led to the deposits of marl beds and increased surface-water fertility in marine environments. In marl beds, the bulk carbonate $\delta^{13}C$ also correlates with the $CaCO_3$ content ($r = 0.78$; Fig. 4E), likely reflecting this increase in primary productivity during marl bed deposits. The pelagic producers are not the dominant carbonate component of these limestone beds and their abundance decrease when the $CaCO_3$ content of the rock increases (Reboulet et al., 2003; Gréselle et al., 2011). These correlations between lithology and climate are not only true at marl-limestone alternation scale, but are also verified at 100-kyr, 405-kyr eccentricity scales, and longer time scale (Fig. 5). In the Vocontian Basin, the trend in $CaCO_3$ contents of the alternations mimics the trend in neritic carbonate production at 10^7-to-10^4-year time scales (Ferry and Monier, 1987; Föllmi et al., 1994; Quesne and Ferry, 1995; Reboulet et al., 2003). Detailed platform-basin correlations show a progressive decrease in thickness and size of carbonate particles toward the basin, which suggest that most of carbonate

mud deposited in the basin was exported from the platforms through nepheloid flows (Reboulet et al., 2003). In the *Neocomites neocomiensiformis* Zone of Vergol, the trend in bulk carbonate $\delta^{13}C$ in marl beds follows the trend in the kaolinite content (Fig. 3). Comparatively, the trend in bulk carbonate $\delta^{13}C$ in limestone beds follows he trend in $CaCO_3$ content. These various trends reflect the change in the isotopic signature of the carbonate mud through the change in carbonate producers, themselves climatically control (Martinez et al., 2020b).

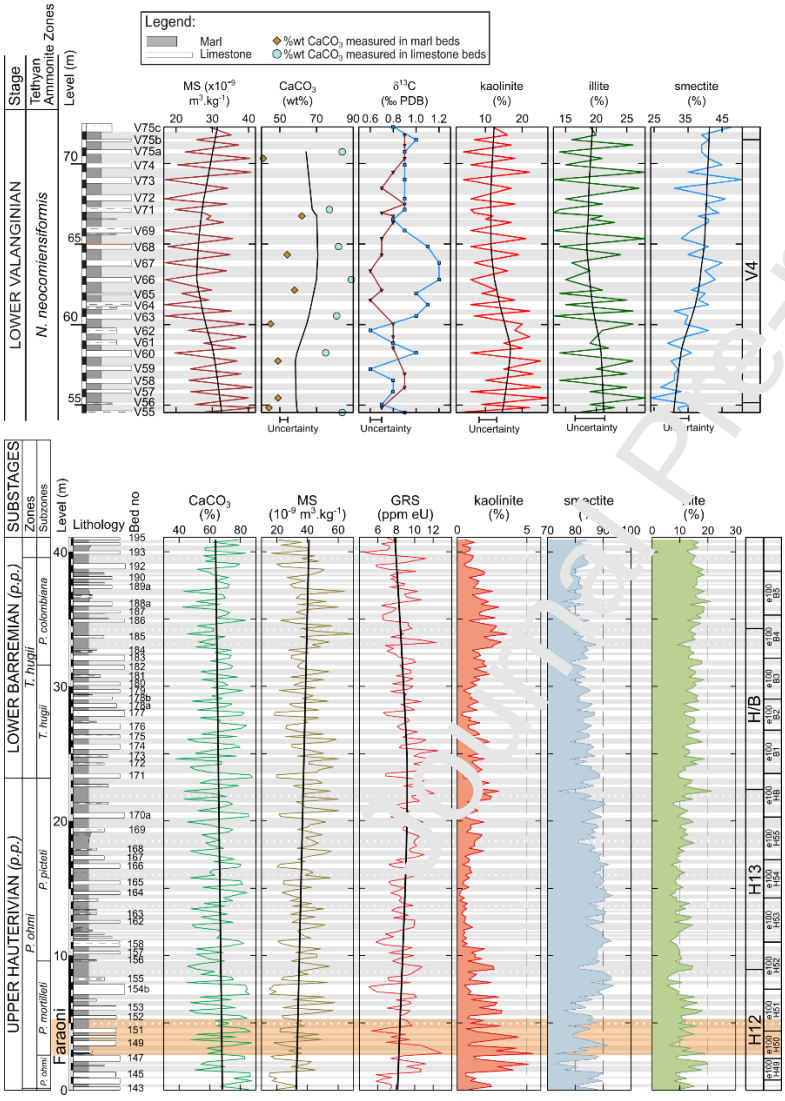

Fig. 3. Behavior of Magnetic Susceptibility (MS), $CaCO_3$ content $\delta^{13}C_{carb}$ and clay mineral assemblage over several marl-limestone alternations of the Vergol section (up; from Martinez et al. (2020b) and the Río Argos section (down; from Martinez et al., 2012; Moiroud et al., 2012).

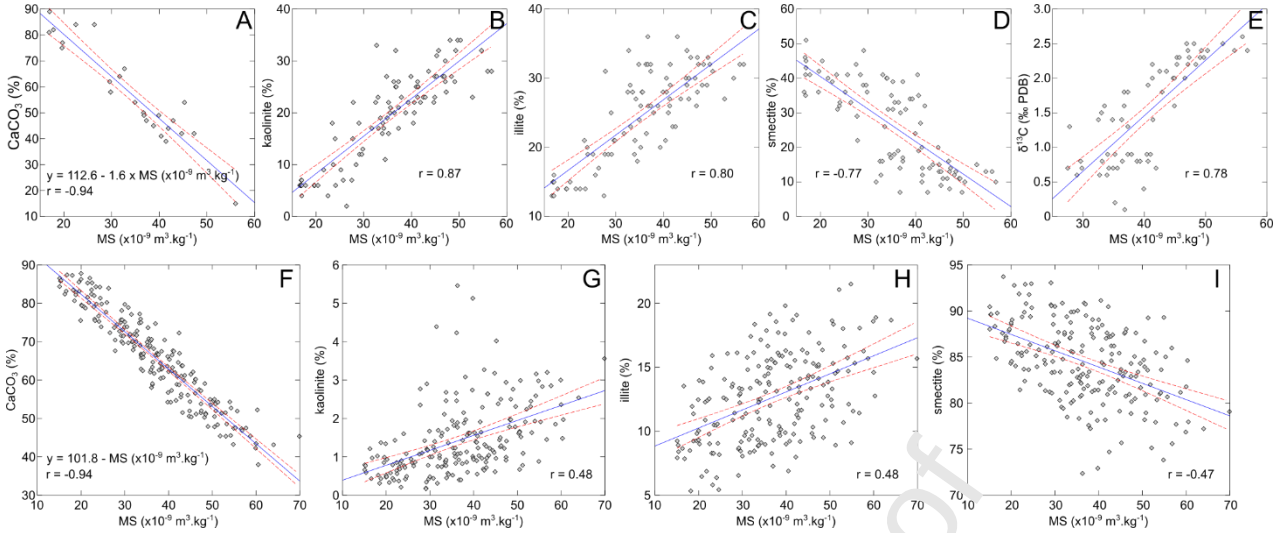

Fig. 4. Cross plots between the MS, $CaCO_3$ content and clay species content. **From A to E**: data from Vergol-Morénas (Martinez et al., 2020b). **From F to I**: data from Río Argos (Martinez et al., 2012; Moiroud et al., 2012). The blue line indicates the best fit and the red lines the 95 % confidence intervals.

Platform-basin correlations and geometry of the platform carbonate wedges suggest that limestone beds correspond to regressive intervals, while marl deposits formed during transgressive intervals and maximum flooding (Quesne and Ferry, 1994; Godet et al., 2013). This relationship can be complicated at precession-scale if the amplitude of sea-level change is just enough to transiently inhibit the carbonate production (Pittet, 2006), leading to the deposit of a thin limestone and marl bed next to a thicker limestone bed or to clustered thin limestone and marl beds separated by thick marl beds (Pittet and Strasser, 1998; Pittet, 2006). This link between lithology and sea-level also existed at larger scale since the intervals of local maxima in clay contents in the *S. verrucosum* Zone (upper Valanginian; Fig. 5) and the *Saynoceras sayni* Tethyan Ammonite Zone (upper Hauterivian; Fig. 6A). Both correspond in time to drowning of the carbonate platforms, notably marked by stepwise retrograding wedges, condensation and eutrophication in a context of increased humid climate, as well as widespread offshore marl deposits (*Marnes à Astieria* in the upper Valanginian and *Marnes d'Uttins* and *Marnes de Cornaux*, at the lower-upper Hauterivian transition; Godet et al., 2011; Morales et al., 2013; Pictet, 2021). Similarly, transgressive intervals are also noted by the increase in clay content of the marl-limestone alternations at the base of the Valanginian Stage (Morales et

al., 2013; Figs. 6E, F). The marlier interval at the end of the Valanginian Stage (Ferry, 1987; Fig. 6B) corresponds to the widespread deposits of the *Marnes d'Hauterive* (Walter, 1996; Gréselle and Pittet, 2010; Morales et al., 2013). In the Late Barremian, the marlier interval in the *I. giraudi* Zone, corresponds in time to the change of neritic carbonate community from photozoan to heterozoan assemblages, in line with increased trophic levels (Frau et al., 2020). This model of higher sea-level during marl deposits contradicts the model of highstand shedding (Schlager et al., 1994), which remains to be explained. In the uppermost Hauterivian to Barremian of the Subbetic Domain, notice that the 2nd-order Maximum Flooding Surfaces (MFS) are more likey associated with long term decrease in detrital content in line with decreased sedimentation rates (Martinez et al., 2020a). This correspondence between detrital content and sedimentation rate was there interpreted as basin starvation during sea-level rise.

This last example illustrates that the response of the lithology to sea-level change in marl-limestone alternations also depends on local factors, such as palaeotopography, areas of the sea floor in the photic zone, oceanic circulation or sedimentary fluxes. However, in all cases studied here, marl deposits more likely occurred under humid conditions while limestone deposits occurred under more arid conditions.

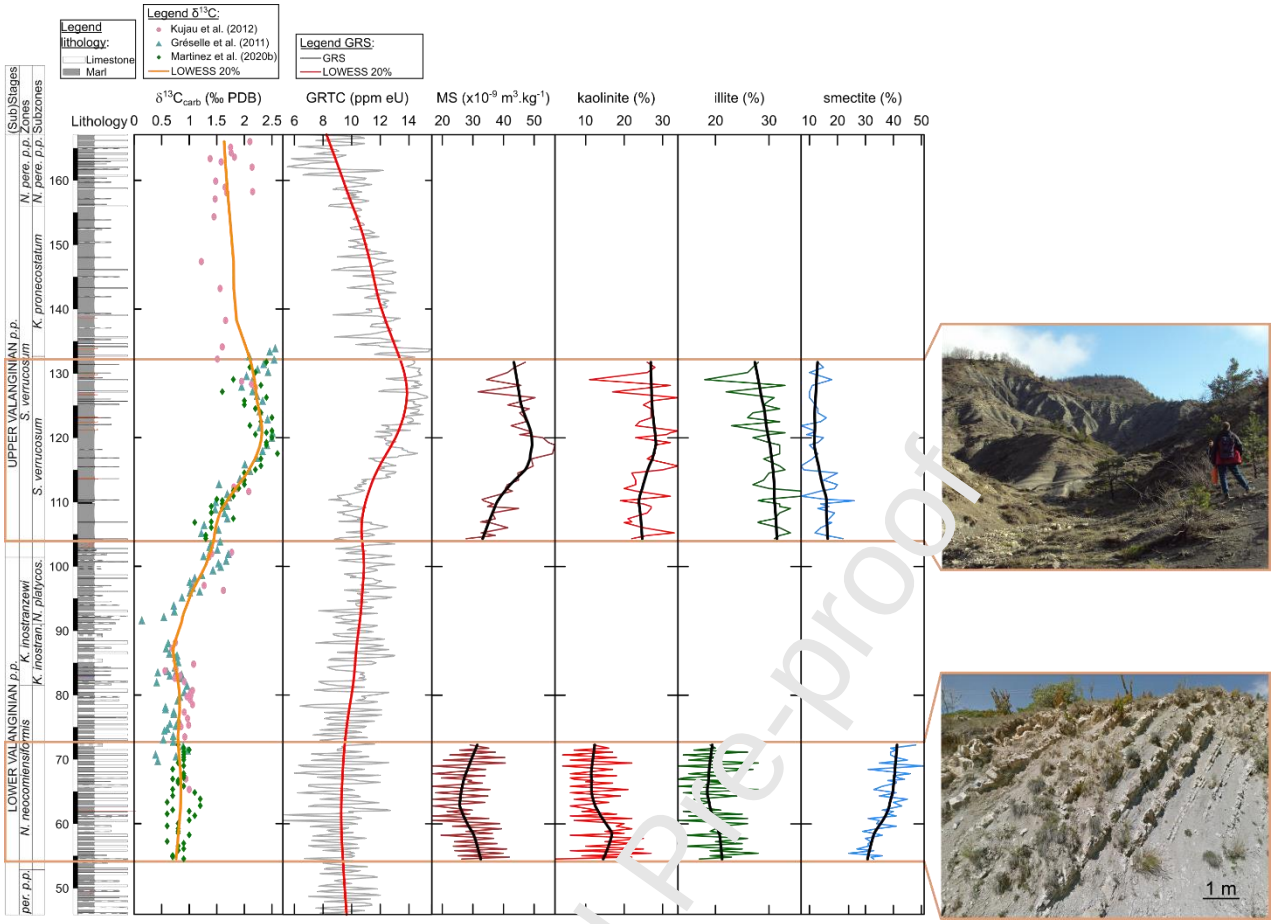

Fig. 5. $\delta^{13}C$, Gamma-Ray Total Count (GRTC), Magnetic Susceptibility (MS) and clay mineral assemblages from the Vergol-Morénas section. The $\delta^{13}C$ data are from Gréselle et al. (2011), Kujau et al. (2012), Martinez et al. (2020b). The two pictures to the right are from Vergol-Morénas.

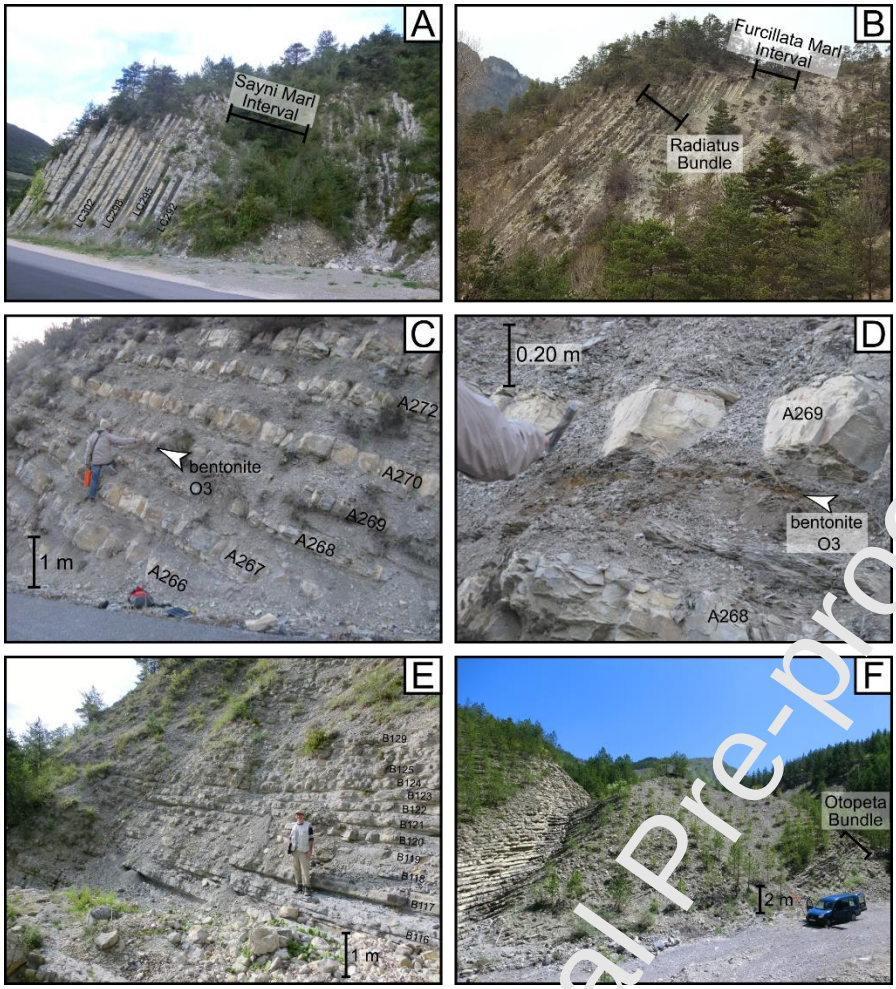

Fig. 6. Examples of bundles and beds used as correlation markers throughout the Vocontian Basin. **A.** The Sayni Marl Interval (Upper Hauterivian) at La Charce section. Beds numberd are labelled according to Martinez et al. (2013) following Reboulet and Atrops (1999) numbering scheme. **B.** Furcillata Marl Interval and Radiatus Bundle at the Valanginian-Hauterivian boundary of the La Charce section. **C.** Bentonite O3 in the *N. neocomiensiformis* Tethyan Ammonite Zone (Lower Valanginian) at the Angles section. Bed number is from Busnardo et al. (1979). **D.** Close-up view of bentonite O3. **E.** View of the Otopeta Bundle at the Vergol section. Bed numbers are from Kenjo et al. (2021). **F.** View of the Otopeta Bundle at the Reynier section. Note the interval of less visible limestone beds above the Otopeta Bundle is due to increase of clay content. This outcropping condition is also observed at Vergol.

2.4. Biostratigraphic framework

Establishing geological time scales requires the calculation of the durations of chronozones rather than biozones. Biozones are based on the paleontological observation from a section, if possible a given basin. Because of quality of preservation of the paleontological record, migration of fauna, local environmental conditions or density of sampling, bioevents are not necessarily recorded synchronously at global scale, and even within a given basin. In a given basin where multiple sections have been studied, it is possible to assess and minimize the uncertainties linked to the quality of preservation of the paleontological record provided the lithological changes can be correlated. This is the case for the Vocontian Basin and the Subbetic Domain, where remarkable bundles have been correlated through the basin (Cotillon, 1971; Company et al., 2003; Gréselle and Pittet, 2010; Martinez et al., 2020a; Kenjo et al., 2021; Aguado et al., 2022; Figs. 6-8).

The Valanginain series studied here are composite Vergol-Morénas, Reynier, Orpierre, Angles and composite La Charce-Pommerol (Fig. 2). The biostratigraphy of Vergol-Morénas, Angles and La Charce-Pommerol are based on ammonites, calcareous nannofossils and calpionellids (Bulot et al., 1992; Blanc, 1996; Reboulet and Atrops, 1999; Reboulet et al., 2003; Duchamp-Alphonse et al., 2007; Gardin, 2008; Gréselle et al., 2011; Kenjo et al., 2021). This biostratigraphic framework is refined thanks to the correlations of remarkable levels and bundles of limestone beds that can be identified bed-to-bed throughout the Vocontian Basin (Cotillon, 1971; Gréselle and Pittet, 2010; Kenjo et al., 2021). These remarkable levels are from bottom to top: (i) the Otopeta Bundle (Figs. 6E, F), described as a series of 12 closely-spaced limestone beds below the Berriasian-Valanginian boundary, from bed B118 to bed B129 at Vergol (Kenjo et al., 2021) and correlated to the interval from bed R1 to R13 in Reynier based on gamma-ray signal (Martinez et al., 2013), (ii) the bentonite layer O3 (Fesneau et al., 2009), first identified in marl bed V65-V66 at Vergol and then identified in marl A268-A269 at Angles and marl R111-R112 at Reynier (Martinez et al., 2013; Figs. 6C, D), (iii) the Tetrade, a bundle of four beds at the boundary between the *K. inostranzewi* and *S. verrucosum* zones (Cotillon, 1971), (iv) the Pronecostatum Bundle, at the base of the *Karakaschiceras pronecostatum* Tethyan Ammonite Subzone (Cotillon, 1971; Fig. 7), (v) the Peregrinus Bundle, also called "*Faisceau Médian*", a cluster of 10 limestone beds at the base of the *Neocomites*

peregrinus Tethyan Ammonite Zone, spectacularly correlated throughout the basin (Cotillon et al., 1980; Fig. 7), (vi) the Nicklesi Bundle, a cluster of 4 limestone beds at the transition between the *N. peregrinus* and *Olcostephanus (Olcostephanus) nicklesi* Tethyan Ammonite subzones (Cotillon, 1971; Fig. 7), (vii) the double Trinodosum Bundle, two clusters of limestone beds at the transition between the *N. peregrinus* and *Criosarasinella furcillata* Tethyan Ammonite zones, (viii) the base of the *Acanthodiscus radiatus* Tethyan Ammonite Zone is marked by a rapid increase in $\%CaCO_3$ of the limestone beds and by harder limestone beds in the field above the *Vire Marneuse à Callidsicus* (Figs. 6B, 8). The MS and GRTC signals correlate with the biostratigraphic frameworks and marker beds (Martinez et al., 2013; Boulila et al., 2015).

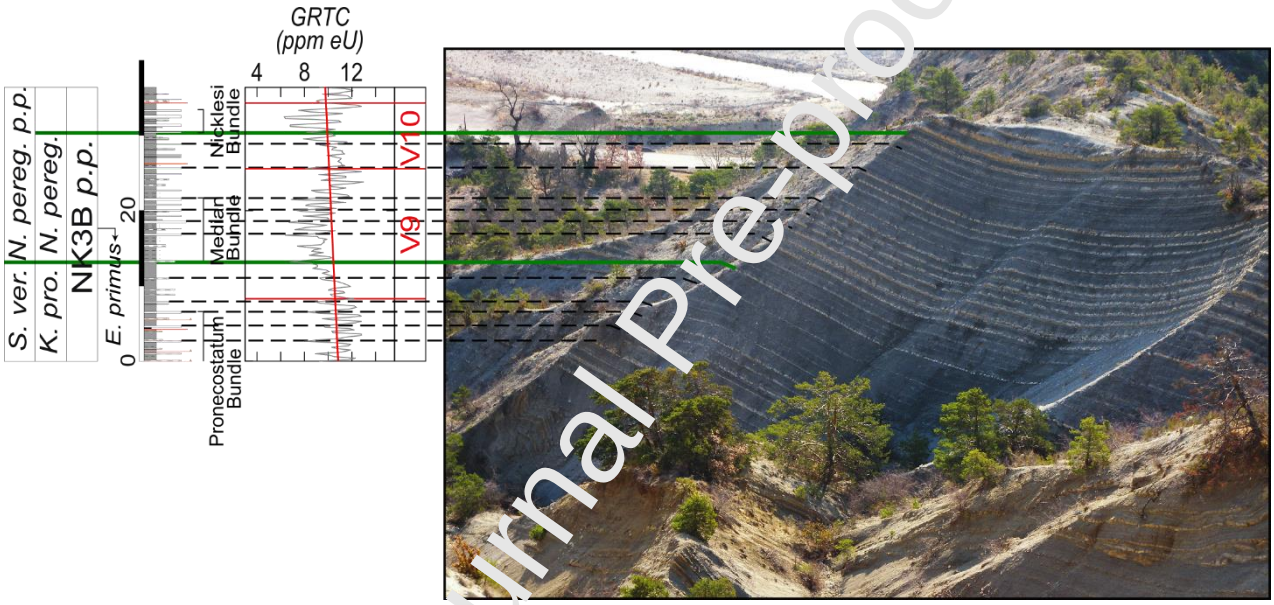

Fig. 7. Correspondance between the Gamma-Ray Total Count (GRTC) signal, the 405-kyr eccentricity cycles and the lithology in the Pronecostatum, Median and Nicklesi bundles (Upper Valanginian) of the La Charce section. Ammonite zonation is from Bulot et al. (1992) and Reboulet and Atrops (1999). Calcareous nannofossil biostratigraphy is from Barbarin et al. (2012).

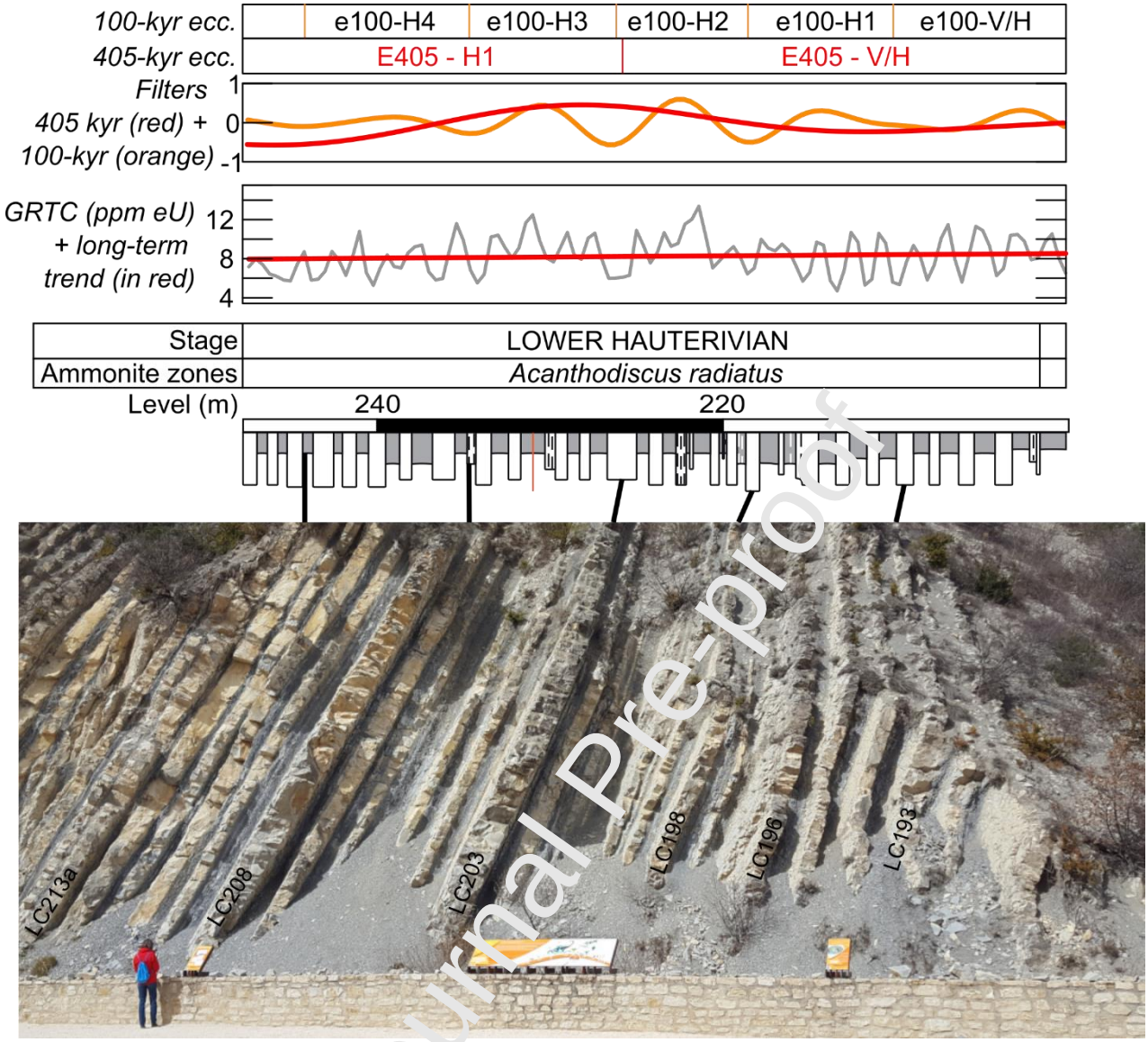

Fig. 8. Correspondance between the Gamma-Ray Total Count (GRTC) signal, the 405-kyr, 100-kyr eccentricity cycles and the lithology in the Radiatus Bundle (Lower Hauterivian) of the La Charce section. Bed number and biostratigraphy are from Reboulet and Atrops (1999), also available in higher resolution in Mutterlose et al. (2021).

The biostratigraphic framework of the Orpierre section is provided in Charbonnier et al. (2013), which locates the Berriasian-Valanginian boundary at the first occurrence of *Calpionellites darderi*. The biostratigraphic framework of the Berriasian-Valanginian boundary was recently revised at Vergol in Kenjo et al. (2021). Several remarkable differences between the two biostratigraphic frameworks can be

noted: (i) the LO of calcareous nannofossil *R. nebulosus* is in the *"T." pertransiens* Tethyan Ammonite Zone and above the FO of calpionellid *C. darderi*, and calcareous nannofossils *E. windii* and *C. oblongata* at Vergol (Kenjo et al., 2021), while it is below all these events at Orpierre (Charbonnier et al., 2013); (ii) the FOs of *E. windii*, *C. oblongata* and *Z. trivectis* are above the FO of *C. darderi* at Vergol (Kenjo et al., 2021), unlikely the Orpierre section (Charbonnier et al., 2013); (iii) FO of *Z. trivectis* is below the FO of *C. oblongata* at Vergol (Kenjo et al., 2021), unlikely the Orpierre section (Charbonnier et al., 2013).

In addition to these biostratigraphic unconsistencies, the base of the Valanginian Stage defined at Orpierre (Charbonnier et al., 2013) and at Vergol (Kenjo et al., 2021) do not correlate using the MS and GRTC signals, while these signals correlate with biostratigraphy higher in the Valanginian series and with lithology (Martinez et al., 2013; Charbonnier et al., 2013; Boulila et al., 2015). The FO of *"T." pertransiens* occurs *ca.* 5 m above the Otopeta Bundle and 5 m below a rapid increase in GRTC values (Fig. 9; Kenjo et al., 2021) correlated to the Reynier section (Martinez et al., 2013). Correlating the GRTC and MS signals would position the level equivalent to the FO of *"T." pertransiens* at level 10 m at Orpierre, which would locate the Berriasian-Valanginian boundary 18 m below the FO of *C. darderi* identified in Charbonnier et al. (2013). The work of Kenjo et al. (2021) demonstrate that detailed observations of biostratigraphic markers are necessary at specific intervals to determine the biozone boundary with accuracy. In this case, the use of quantitative lithological markers, such as MS and GRTC, can help in correlating FADs and LADs within a basin or between basins. Similarly, the base of NK3B calcareous nannofossil Zone is located at the LAD of *R. wisei* identified in the Vocontian Basin, the base of the NC4A at the highest position of the LCO of *T. verenae* between Angles and Orpierre (which questions the meaning of this LCO, *T. verenae* having been observed in La Charce in the lower Hauterivian; Gardin, 2008). In addition, the Tethyan ammonite zonation at Reynier and Orpierre is correlated to Vergol-Morénas, Angles and La Charce (Figs. 9, 10).

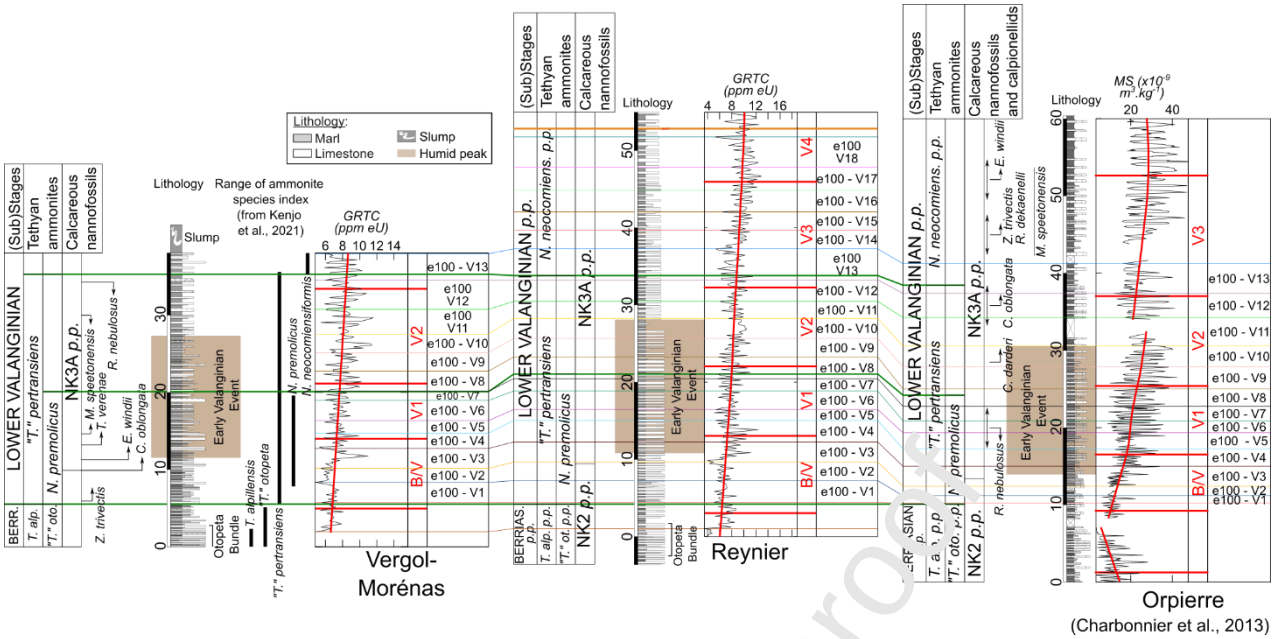

Fig. 9. Biostratigraphic framework of the Berriasian-Valanginian transition. Ammonite and calcareous nannofossil data are from Kenjo et al. (2021). Calcareous nannofossil and calpionellid data are from Charbonnier et al. (2013). The Gamma-Ray Total Count (GRTC) data are from Martinez et al. (2013) and the Magnetic Susceptibility data (MS) are from Charbonnier et al. (2013). The ammonite zonation at Reynier and Orpierre is extrapolated from Vergol by correlation of GRTC and MS signals. Boundaries of calcareous nannofossil zone boundaries are located at the FAD or LAD of the index species within the Vocontian Basin, determined by correlation of GRTC and MS signals.

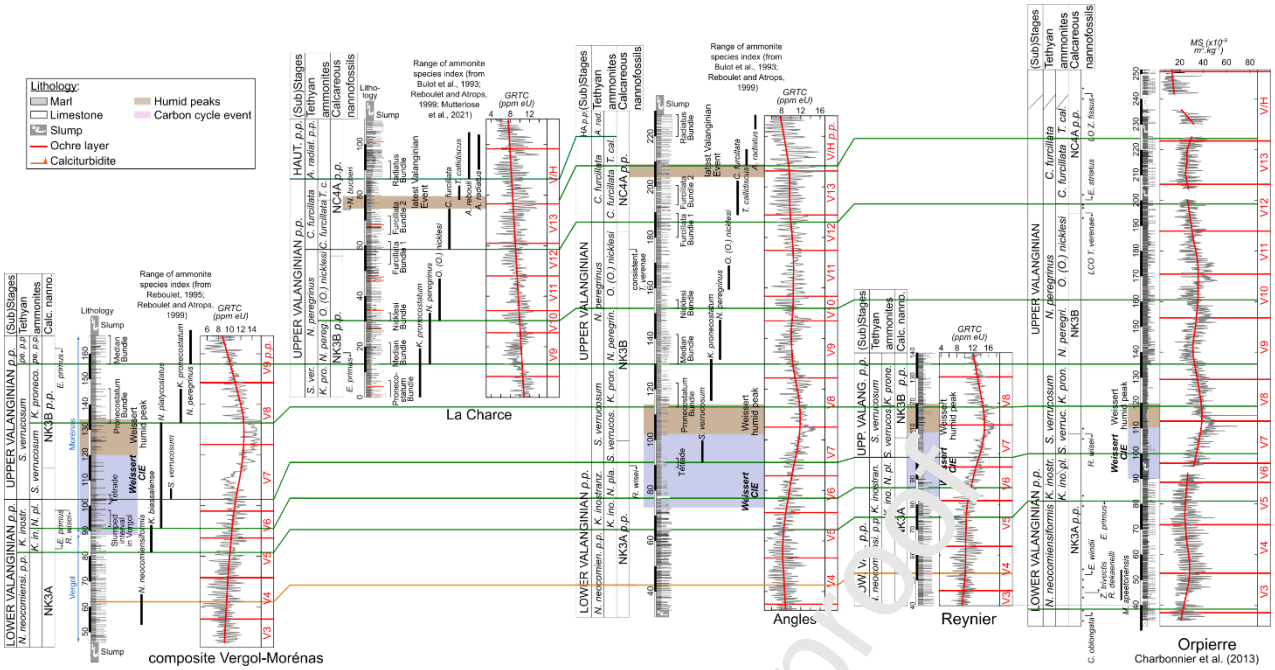

Fig. 10. Biostratigraphic framework of the analysed sections from the lower Valanginian to the lower Hauterivian. Ammonite data are from Bulot et al. (1992), Reboulet (1995), Reboulet and Atrops (1999) and Mutterlose et al. (2021). Calcareous nannofossil data are from Duchamp-Alphonse et al. (2007), Gréselle et al. (2011), Barbarin et al. (2012) and Charbonnier et al. (2013). The boundaries of the ammonite and calcareous nannofossil zones are fixed at the FO or LO of the considered species index in the Vocontian Basin and correlated to the other sections using the Gamma-Ray Total Count (GRTC) and Magnetic Susceptibility (MS) signals. The GRTC signals are from Martinez et al. (2013). The MS signal is from Charbonnier et al. (2013).

In the Hauterivian Stage, the Tethyan and Andean Ammonite zonation are available in Bulot et al. (1992), Reboulet and Atrops (1999), Hoedemaeker and Leereveld (1995), Company et al. (2003, 2005), Martinez et al. (2012), Aguado et al. (2014) and Aguirre-Urreta et al. (2017, 2019) and calcareous nannofossil data are from Thierstein (1973), Gardin (2008), Hoedemaeker and Leereveld (1995), Company et al. (2003) and Aguado et al. (2014). Correlation between the Andean and Tethyan Ammonite zones is necessary to anchor the astrochronology of the Tethyan areas (where the stage boundaries are defined) to the Andean radio-astrochronology (where U-Pb ages are available; Aguirre-Urreta et al., 2017). The widespread, short-lived

distribution of the *Olcostephanus (Jeannoticeras)* subgenus is regarded as a major ammonite event in the Hauterivian Stage to establish firm correlations at global scale (Lehmann et al., 2015). The occurrence of the *O. (Jeannoticeras)* subgenus is recorded within the *Olcostephanus (Olcostephanus) laticosta* Andean Ammonite Subzone and in the *Olcostephanus (Jeannoticeras) jeannoti* Tethyan Ammonite Subzone (Aguirre-Urreta et al., 2017, 2019). The correlation between the base of the *Holcotpychites neuquensis* Andean Ammonite Zone to the base of the *Acanthodiscus radiatus* Tethyan Ammonite Zone is another important correlation line to quantify the variaibility of the duration estimates, and thus, the uncertainty in the correlation lines.

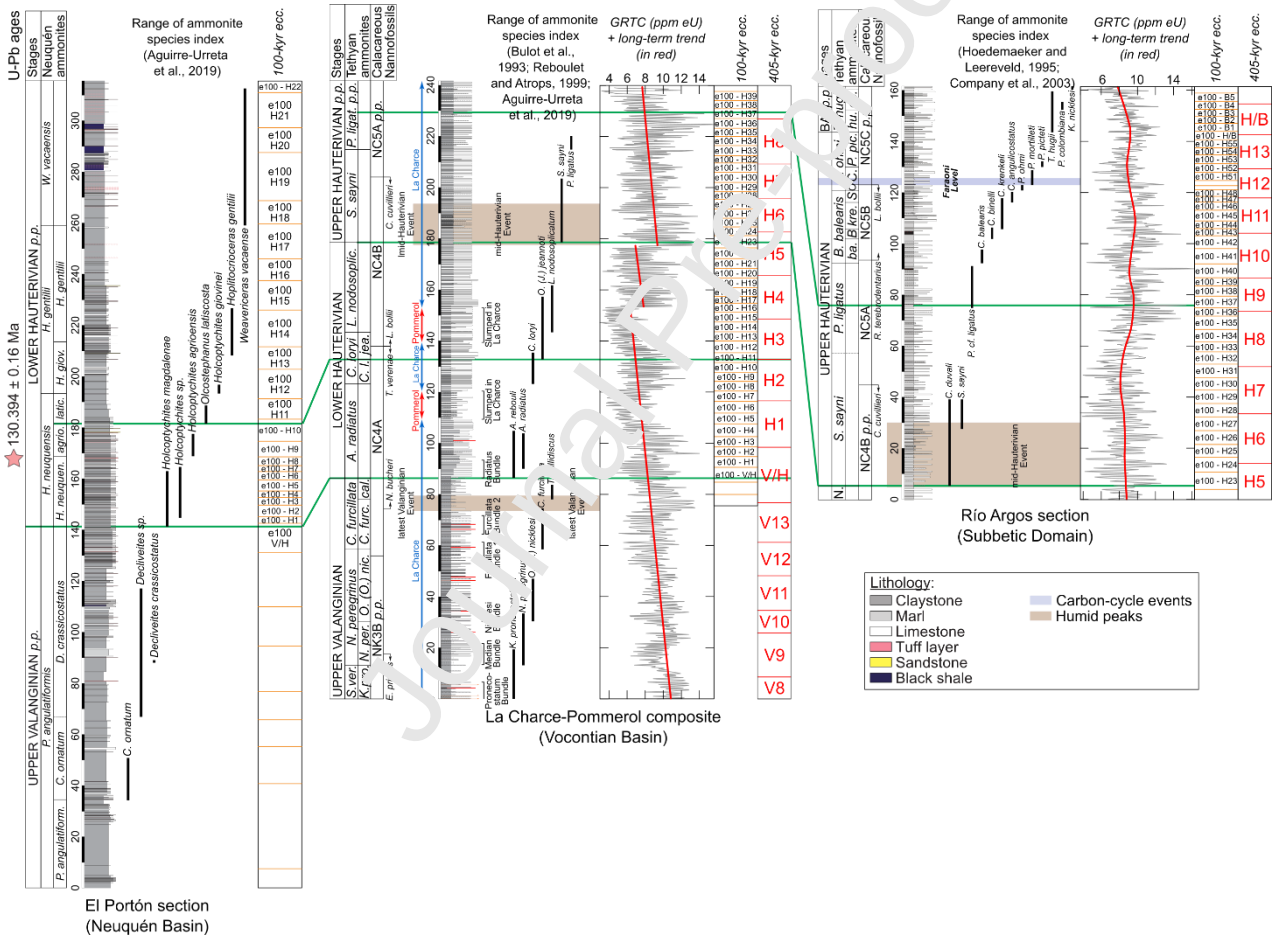

Fig. 11. Biostratigraphic framework of the analysed sections from the upper Valanginian to the lower Barremian in the Neuquén Basin, Vocontian Basin and Subbetic Domain. The ammonite data are from Bulot et al. (1992), Reboulet and Atrops (1999), Aguirre-Urreta et al. (2019), Hoedemaeker and Leereveld (1995) and Company et al. (2003). The calcareous nannofossil data are from Thierstein (1973), Gardin

(2008), Hoedemaeker and Leereveld (1995), Company et al. (2005) and Aguado et al. (2014). The pink star at El Portón indicates the stratigraphic location of a CA-ID-TIMS U-Pb age on zircons from Aguirre-Urreta et al. (2017).

In the upper Hauterivian, the La Charce and Río Argos sections are correlated with (i) the base of *Saynoceras sayni* Tethyan Ammonite Zone, (ii) the last occurrence of the *Cruciellipsis cuvillieri* calcareous nannofossil, and (iii) the local maximum in the GRTC values in the *P. ligatus* Tethyan Ammonite Zone. The boundary between the *S. sayni* and the *P. ligatus* Tethyan Ammonite zones was notably located at Río Argos from these correlations, as there is a gap in the ammonite record from 40 to 75 m (Hoedemaeker and Leereveld, 1995; Martinez et al., 2015; Fig. 11).

The ammonite and calcareous nannofossil biostratigraphy of the Barremian Stage was defined at Río Argos, Arroyo Gilico and Barranco de Cavila in Company et al. (2003) and Aguado et al. (2014, 2022). Río Argos and Arroyo Gilico are easily correlated with ammonites, bundles of limestone beds and the record of the 100-kyr eccentricity cycles (Martinez et al., 2020a). Arroyo Gilico and Barranco de Cavila are correlated with the first occurrence of *Lithraphidites rugio* (Aguado et al., 2022), occurring both near the top of 405-kyr eccentricity cycle B5 (Martinez et al., 2020a; Fig. 12). Finally, *Deshayesites oglanlensis* was not found in Barranco Cavila, so that there is an uncertainty zone on the location of the Barremian-Aptian boundary, that we underlined in a grey area (Fig. 12). The location of the stage boundary was located using the $\delta^{13}C$ signal (Martinez et al., 2020a; Aguado et al., 2022). The impact on the uncertainty of the stage ages is discussed below.

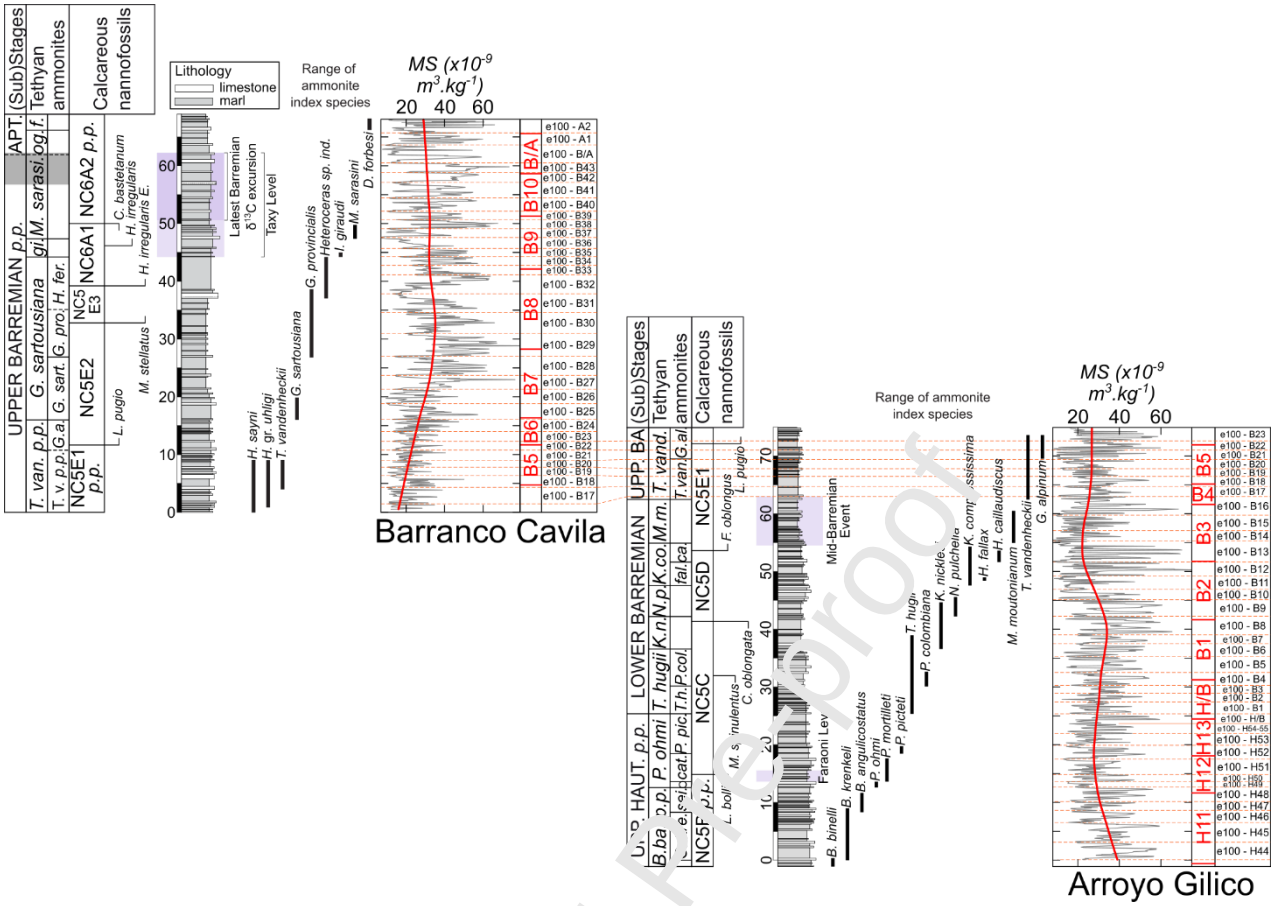

Fig. 12. Biostratigraphic framework from the upper Hauterivian to the lowermost Aptian. The ammonite data are from Aguado et al. (2014) and calcareous nannofossil data from Aguado et al. (2014, 2022).

2.5. Previous astrochronologic frameworks

2.5.1. Valanginian Stage

The duration estimates of the Valanginian Stage was assessed at 7.0-7.6 Myr in Rio et al. (1989), 5.9 Myr in Huang et al. (1993), 7.0 Myr in Giraud et al. (1995) and 4.7 Myr in Gréselle and Pittet (2010). Since Bulot (1996), the definition of the base of the Valanginian Stage moved from the FO of the *"T." otopeta* Tethyan ammonite to the FO of *C. darderi* calpionellid, equivalent in time to the FO of *"T." pertransiens* (Blanc, 1996). As the duration of the *"T." otopeta* Subzone is assessed at 0.43 Myr, the duration of the Valanginian Stage without the *"T." otopeta* Subzone is 6.4-7.2 Myr in Rio et al. (1989), 5.5 Myr in Huang et al. (1993) and 6.4 Myr in Giraud et al. (1995). These three durations estimates were calculated from the

Angles section and are based on cycle counting (Rio et al., 1989; Gréselle and Pittet, 2010) or on spectral analyses on encoded lithology (Huang et al., 1993; Giraud et al., 1995). In all these cases, the durations depend on the visual identification of the lithology, which is much harder in the upper Valanginain. In the *S. verrucosum* Tethyan Ammonite Zone, the limestone beds vanish so that precession cycles can not be discriminated. In the remainder of the upper Valanginian, a precession cycle can be subdivided into a bundle of thin limestone beds, which could be related to rapid sea-level change that could transiently inhibited the carbonate production and export within a precession cycle (Pittet and Strasser, 1998; Pittet et al., 2000). In the upper Valanginian, Boulila et al. (2015) noted that approximately half of precession cycles are missing in the upper part of the *N. peregrinus* Tethyan Ammonite Zone, thereby compromising reliable duration estimates with precesion cycle counting only. Thus, cycle counting from a section leads to highly variable durations and it is preferable to recognize longer cycles from a quantitative proxy for a more reproducible procedure and to limit the risk of entirely missing cycles. With such an approach, Sproveri et al. (2006), Martinez et al. (2013) and Charbonnier et al. (2013) respectively estimated the duration of the Valanginian Stage at 6.9 Myr, 5.08 Myr and 4.8 Myr, respectively. The high variability of the duration assessments is here linked to the appropriate definition of the base of the Valanginian Stage, the sample resolution adapted to the characterization of the precession cycle, necessary to recognize the eccentricity cycles, and the presence of sedimentary discontinuities. It is noteworthy that in the lower Valanginian, the interval covering 405-kyr cycles V1 and V2 defined in Martinez et al. (2013) encompasses 64 marl-limestone alternations, attributed to the precession cycle (Blard et al., 2023), which should correspond to 3 repetitions of the 405-kyr eccentricity cycle. So, the age model of this interval needs a reappraisal.

2.5.2. Hauterivian Stage

The duration estimates of the Hauterivian Stage were assessed at 4.8-5.2 Myr in Rio et al. (1989), 5.3 Myr in Huang et al. (1993), 5.3 ± 0.4 Myr in Fiet et al. (2006), 5.93 ± 0.41 Myr in Martinez et al. (2015) and 5.21 ± 0.08 Myr in Aguirre-Urreta et al. (2019). Rio et al. (1989) and Huang et al. (1993) based their

calculations on marl-limestone couplet counting and visual identification on the Angles and nearby Vergons sections. The definition of the base and top of the Hauterivian have not changed since their study. Both the Angles and Vergons sections contain a series of slumps, which can be associated to missing sequences. For instance, the two slumps in the lower Hauterivian of La Charce correspond to a total of 30 marl-limestone alternations preserved in Pommerol (Martinez et al., 2015). Fiet et al. (2006) did not specify from which section they counted the marl-limestone couplets, which prevents from assessing the quality of the sections they studied. The duration of the Hauterivian Stage calculated from astrochronology varies from 5.93 ± 0.41 Myr (Martinez et al, 2015) to 5.21 ± 0.08 Myr (Aguirre-Urreta et al., 2019). In all cases, the sections are composite and devoid of slumps. In Martinez et al. (2015), the uncertainty in the duration came from the identification of the 405-kyr eccentricity cycles in the Early Hauterivian. A total of 6 repetitions of the 405-kyr cycle was interpreted from the filter of the gamma-ray series in La Charce-Pommerol. The Early Hauterivian in the composite La Charce-Pommerol contains 108 marl-limestone couplets attributed to precession which suggests a shorter duration. The shorter duration finally appeared more consistent with the radio-astrochronology of the Pilmatué Member in the Neuquén Basin (Aguirre-Urreta et al., 2019; Fig. 2). The calibration of the upper Hauterivian at Río Argos is mainly based on the record of the 100-kyr eccentricity cycle (Aguirre-Urreta et al., 2019). Spectral analyses from the Hauterivian-Barremian boundary demonstrates that the 405-kyr cycle can be extracted from the spectrum of clay mineral assemblages or from amplitude modulation of the 100-kyr eccentricity from magnetic susceptibility (Martinez et al., 2015). As in the Early Valanginian, the extraction of the 405-kyr eccentricity cycle needs a reappraisal, notably through testing the amplitude modulation of the precession cycles.

2.5.3. Barremian Stage

The duration of the Barremian Stage was assessed at Gorgo a Cerbara (Umbria-Marche Basin, Central Italy) at 5.13 ± 0.34 Myr in Fiet and Gorin (2000), 4.93 Myr in Bodin et al. (2006a), 4.4 Myr in Sprovieri et al. (2006). The duration of the Barremian Stage in these cases was calculated upon the visual identification of the lithological record of the 100-kyr eccentricity cycles from the first occurrence of the Tethyan

ammonite *Taveraidiscus hugii* to the base of magnetochron M0r. In this interval, Fiet and Gorin (2000) identified 47 bundles, Bodin et al. (2006a) identified 49.3 bundles and Sprovieri et al. (2006) identified 44 bundles. Fiet and Gorin (2000) applied a mean duration of 109 kyr of the short eccentricity cycle, while a mean duration of 100 kyr was applied in Bodin et al. (2006a) and Sprovieri et al. (2006). The duration of 109 kyr corresponds to the average between the two main periods of the short eccentricity of 124 kyr and 95 kyr (see Laskar et al., 2004, 2011). In the astronomical solution of Laskar et al. (2011) taken in the last 50 Myr, the average duration of 47 consecutive 100-kyr eccentricity cycles is 4.47 ± 0.11 Myr (2σ), leading to an average duration of the 100-kyr cycle of 95.2 ± 2.2 kyr. Thus, the durations proposed in Fiet and Gorin (2000), Bodin et al. (2006a) and Sprovieri et al. (2006) should be 4.5 ± 0.1, 4.7 ± 0.1 and 4.2 ± 0.1 Myr, respectively. This difference, from the same section and three different studies, illustrates the uncertainty of the cycle-derived durations based on the visual identification of the lithological cycles only. In the Angles section (Vocontian Basin, SE France), cycle counting attributed to the precession cycle led to a duration estimate of the Barremian Stage of 4.5 Myr (Bodin et al., 2006a). However, in the Vocontian Basin, the Barremian Stage is defined from the first occurrence of the ammonite *T. hugii* to the first occurrence of the ammonite *Deshayesites oglanlensis* (Delanoy, 1997; Reboulet et al., 2018). Recent reattribution of ammonite specimen together with refined calcareous nannofossils biostratigraphy (Frau et al., 2018; Aguado et al., 2022) suggest that magnetochron M0r correlates within the interval of *I. giraudi*–*M. sarasini* Tethyan ammonite zone. Carbon-isotope stratigraphy suggests that the positive carbon-isotope excursion linked to the Taxy Episode occurred within chron M0r, while the related negative carbon-isotope excursion correlates to the top of chron M0r. The Barremian Stage, as defined from Tethyan ammonites, ends within chron C34n (Aguado et al., 2022). Following the correlations proposed in Aguado et al. (2022) and the lithology of Gorgo a Cerbara, the interval equivalent to the Barremian Stage defined by ammonites contains 51 repetitions of 100-kyr cycle in the sequencing of Fiet and Gorin (2000), corresponding to a duration of 4.9 Myr, and 47 repetitions of the 100-kyr cycle in the sequencing of Sprovieri et al. (2006), corresponding to a duration of 4.5 Myr. These durations are in good agreement with the duration of $4.58^{+0.15}_{-0.29}$ Myr proposed in Martinez et al. (2020a) from the 405-kyr cycle identified from spectral analyses

on magnetic susceptibility signals. Different durations of the Barremian Stage were thus proposed because of the difficulty in recognizing the orbital cycles with visual inspection only, different definitions of the Barremian Stage used, and different durations of the ~100-kyr eccentricity cycle used. Here, the spectral analyses will be briefly described as the age model has no change compared to Martinez et al. (2020a).

3. Datasets

3.1. Carbon isotopes

A total of 656 new carbon-isotope data from the Subbetic Domain were acquired for the purpose of this study. Powdered bulk rock samples from Arroyo de Gilico and Cavila sections were collected at a constant interval of ~0.21 m. These samples were analysed for C-isotope ratios using a ThermoScientific MAT253 Isotope Ratio Mass Spectrometer connected to a Kiel IV Carbonate Device at the Stable Isotope Laboratory of the Instituto de Geociencias, Universidad Complutense de Madrid. Isotopic values were calibrated against carbonate standards (NBS-19, NBS-18, and in-house standards). The isotope data are reported with the δ (‰) notation referred to the Vienna-Pee Dee Belemnite (VPDB) standard and an averaged analytical error (1σ) ± 0.01‰.

The bulk carbon-isotope data from the Vocontian Basin and the belemnite data were compiled from the literature (Emmanuel and Renard, 1993; Hennig et al., 1999; van de Schootbrugge et al., 2000; Duchamp-Alphonse et al., 2007; McArthur et al., 2007; Godet et al., 2006; Bodin et al., 2009; Gréselle et al., 2011; Kujau et al., 2012; Charbonnier et al., 2013; Bodin et al., 2015; Price et al., 2018; Martinez et al., 2020b). The data were reported to the bed they were measured and correlated to the different sections, so that they were positioned on the same spliced section and calibrated to time to the same age model. The bulk carbon-isotope data from the Umbria-Marche Basin are from Sprovieri et al. (2006).

3.2. Total Gamma-ray Total Count

The Gamma-Ray Total Count (GRTC) have been acquired in Martinez et al. (2013, 2015) every 0.20 m in

the Valanginian and Hauterivian of the sections of Reynier, Vergol-Morénas, Angles, La Charce and Río Argos. Prior to meaurements, the surfaces have been cleaned from weathered material and smoothed. The GRTC measurements were acquired with a SatisGeo GS-512 device and expressed in equivalent uranium concentration [ppm Ueq] (1 ppm = 1 µg/g), with a constant 1-min duration of acquisition. The reproducibility of the measurement was assessed by measuring 30 times the same spot in marl and limestone beds. The standard deviation of the measurements is 5 % of the mean value. A scintillometer arrangement was used to produce an energy spectrum for the natural gamma-ray emitted from an outcrop. This spectrum was interpreted electronically to yield concentrations of the principal gamma-ray sources involved, namely potassium (K), thorium (Th) and uranium (U). K and Th are usually concentrated in clay minerals, while U is associated to organic matter (Myers and Wignall, 1987).

3.3. Magnetic susceptibility

Mass-normalized Magnetic Susceptibility (MS) has been acquired every 0.25 m with a Kappabridge KLY-2 in El Portón in Aguirre-Urreta et al. (2019) and every 0.07 m with a Kappabridge KLY-3 in Arroyo Gilico and Barranco de Cavila in Martinez et al. (2020a). The mass-normalized MS data from Vergol were acquired with a Kappabridge KLY-3 in Martinez et al. (2020b). Volumic MS were normalized to the sample mass in Aguirre-Urreta et al. (2019) and to the mass and the volume measured (10 cc) in Martinez et al. (2020a, 2020b). The reproducibility of the volumic MS measurements in these studies is 1 % of the MS value. The mass-normalized MS data from Orpierre were acquired in Charbonnier et al. (2013) with a Kappabridge MFK-1B.

3.4. Calcium carbonate content ($CaCO_3$)

$CaCO_3$ wt % data were acquired every 0.07 m in Arroyo Gilico and Barraco de Cavila in Martinez et al. (2020a) using an automatic calcimeter Dream Electronique, with a range of masses 90–150 mg and

measurement time of 20 s at a temperature of 20 ± 2 °C. The maximum error in the determination of the carbonate content is ±4%. $CaCO_3$ wt % were acquired every 0.50 m in the Angles section in Giraud (1994) and every 0.20 m in Río Argos X.Ag-1 section in Moiroud et al. (2012), using a Bernard calcimeter. The maximum error of the Bernard calcimeter in the determination of the carbonate content is ±5%.

4. Spectral analyses

The long-term trend in the average was calculated using best-fit linear regression or LOcally Weighted Scatterplot Smoothing (LOWESS; Cleveland et al., 1979). This long-term trend was subtracted from the series studied prior to the spectral analyses. In case of persistence of a trend in the variance in the residual, the instantaneous amplitude was calculated using a Hilbert Transform. a LOWESS was applied on this instantaneous amplitude and the residual series was divided by the LOWESS of the instantaneous amplitude. The method and parameters of detrend were chosen to remove the variance at frequencies near 0 while not creating spurious spectral peaks or impacting already existing spectral peaks at low frequencies (Vaughan et al., 2015).

Spectral analyses of the considered intervals were performed using 2π Multi-Taper Method (2π-MTM; Thomson, 1982, 1990). The confidence levels in the spectrum were obtained by calculating the moving median over 20% of the spectrum, calculating the best-fit red-noise model of this moving median and extrapolating the confidence levels assuming a χ^2 model. The spectral peaks exceeding the 95% confidence level in a first incrementation were excluded from the calculation of the moving median to not bias the confidence levels toward high values (Mann and Lees, 1996). Evolutive spectral analyses were performed on long compilations of climatic series in order to determine the pervasivity of the ong cycles observed in the 2π-MTM spectra applying Time-Frequency Weighted fast Fourier Transforms (TF-WFFT; Martinez et al., 2015). The length of the windows selected is generally 6 Myr, except for the $\delta^{13}C_{bulk}$ of the Subbetic Domain, studied with 4-Myr long windows.

Filters were done applying Taner lowpass and bandpass filters (Hinnov et al., 2002). Amplitude

modulations were determined by calculating the instantaneous amplitude of the band of interest filtered, usually the precession band, using Hilbert Transform. The 2π-MTM spectra of the instantaneous amplitude of the filtered bands were then calculated to determine on which periods their amplitude evolved. The orbital calibration was performed on the 405-kyr eccentricity cycle either directly filtered from the detrended series, or filtered from the instantaneous amplitude of the precession band. The age model assumes a constant sedimentation rate between each boundary of the 405-kyr cycles.

5. Calibration of the Valanginian Stage

5.1. Extraction of the 405-kyr eccentricity in the lower Valanginian

The calibration of the Early Valanginian Subtage is based on the record of the 405-kyr eccentricity cycle directly filtered from the standardized series or filtered from the instantaneous amplitude of the precession band from the Vergol-Morénas, Orpierre, Reynier and Angles sections.

5.1.1. Spectral analyses of the Reynier series

The trend of the GRTC series of the Reynier section was calculated using the LOWESS method with a coefficient of 0.2. The residual series was then standardized (average = 0; standard deviation = 1). At Reynier, the marl-limestone alternations show a progressive increase in detrital fraction and thickness (Fig. 13). Evolutive spectral analyses support the increase in the thickness of marl-limestone alternations from 0 to 55 m before this thickness stabilizes (Martinez et al., 2013). Noteworthy, the filter of the 405-kyr eccentricity at Reynier generally shows a ratio of 1:20 with the precession cycles, except at two noticeable intervals: cycles V1-V2 in Martinez et al. (2013), which contain 64 marl-limestone alternations, and cycle V5 of Martinez et al. (2013) which contain 12 cycles. This latter feature is also observed in Vergol-Morénas and Angles. It occurs in the upper part in the *K. inostranzewi* Tethyan Ammonite Zone, which is marked by a thick slumped and turbidite-rich interval at La Charce, and a slumped interval at Orpierre. This interval is generally interpreted as an important 3rd-order lowstand (Hardenbol et al., 1998; Mutterlose and Bornemann, 2000; Reboulet et al., 2003; Gréselle and Pittet, 2010; Reboulet et al., 2022), possibly

glacio-eustatically forced (Gréselle and Pittet, 2010; Reboulet et al., 2022). High-amplitude variations in sea-level and climate may have here truncated approximately half of the 405-kyr cycle in the *K. inostranzewi* Tethyan Ammonite Zone, although the exact mechanism remains to be clarified.

The non-correspondance between the number of marl-limestone alternations within cycle V2 in Martinez et al. (2013) suggested a hemi-precession control on these alternations. However, recent $^{3}He_{ET}$ analyses suggest the precession cycle remain the dominant forcing factor of the marl-limestone alternations in the lower Valanginian (Blard et al., 2023), implying that in this part of the Valanginian, the direct filter does not appropriately account for the number of 405-kyr eccentricity cycles. We thus divide here the Reynier series into a first interval from 0 to 55 m and a second from 45 m to the top of the series.

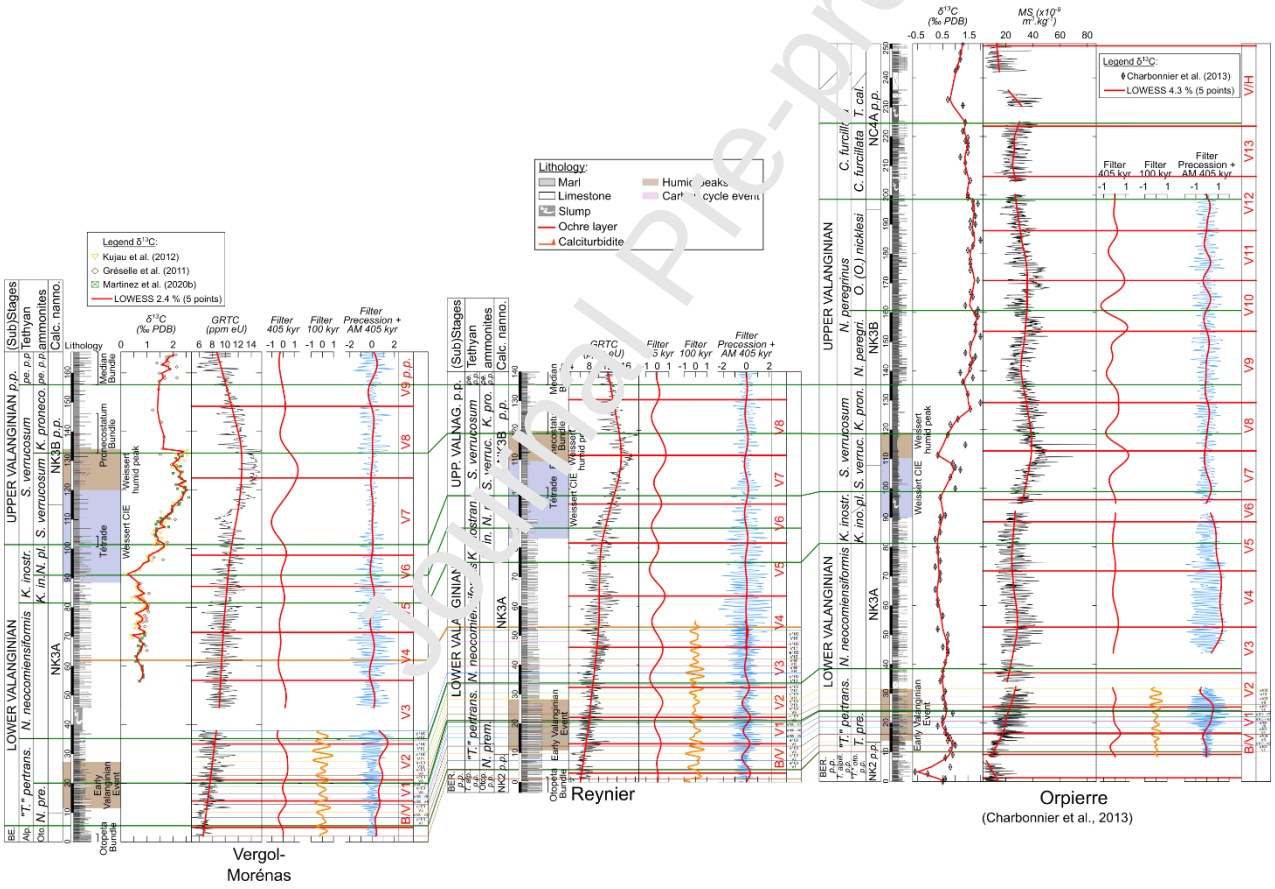

Fig. 13. Correlation of the astrochronologic frameworks in the lower part of the Valanginian series. The $\delta^{13}C_{bulk}$ data of Vergol is from Gréselle et al. (2011), Kujau et al. (2012), Martinez et al. (2020b). The $\delta^{13}C_{bulk}$ data from Orpierre is from Charbonnier et al. (2013).

From 0 to 55 m, the 2π-MTM spectrum shows significant cycles above the 99 % confidence level at 18, 8.1, 0.70 and 0.56 m (Fig. 14A), and cycles above the 95 % confidence level at 2.4 and 0.49 m. The precession cycle ranges from 0.49 to 0.70-m thick, the 100-kyr eccentricity cycle corresponds to the peak at 2.4 m, the 405-kyr eccentricity cycle corresponds to the band from 8.1 m to 18 m. The spectrum of the instantaneous amplitude of the precession cycle shows a peak at 2.6 m, corresponding to the 100-kyr eccentricity cycle, and peaks at 9.6 m and 18 m, corresponding to the 405-kyr eccentricity cycle (Fig. 14B). The precession band was filtered from the GRTC signal applying a bandpass filter with lower and higher frequency cuts at 1.1091 cycles.m^{-1} and 2.4182 cycles.m^{-1}. The 100-kyr eccentricity band was filtered from the GRTC signal applying a bandpass filter with lower and higher frequency cuts at 0.1818 cycles.m^{-1} and 0.50921 cycles.m^{-1}. The 405-kyr eccentricity band was filtered from the instantaneous amplitude of the precession band applying a bandpass filter with lower and higher frequency cuts at 0.04545 cycles.m^{-1} and 0.1364 cycles.m^{-1}.

From 45 m to the top of the series, the 2π-MTM spectrum shows significant cycles above the 99 % confidence level at 17 m, 7.3 m, 1.3 m and 1.0 m (Fig. 14C), and cycles above the 95 % confidence level at 2.1 m, 1.6 m and 0.73 m. The cycle of 17 m is attributed to the 405-kyr eccentricity cycle, the cycle at 2.1 m to the obliquity and the cycles from 1.6 to 1.0 m to the precession cycle. The 2π-MTM spectrum of the instantaneous amplitude of the precession cycle shows spectral peaks at 17 and 12 m, attributed to the 405-kyr eccentricity cycle, from 4.6 to 3.8 m, attributed to the 100-kyr eccentricity cycle, and at 2.8 m (Fig. 14D). The precession band was filtered from the GRTC signal applying a bandpass filter with lower and higher frequency cuts at 0.5591 cyclesm^{-1} and 1.4451 cycles.m^{-1}. The 405-kyr eccentricity cycle extracted from the instantaneous amplitude of the precession band was filtered applying a bandpass filter with lower and higher frequency cuts at 0.0455 cycles.m^{-1} and 0.1364 cycles.m^{-1}.

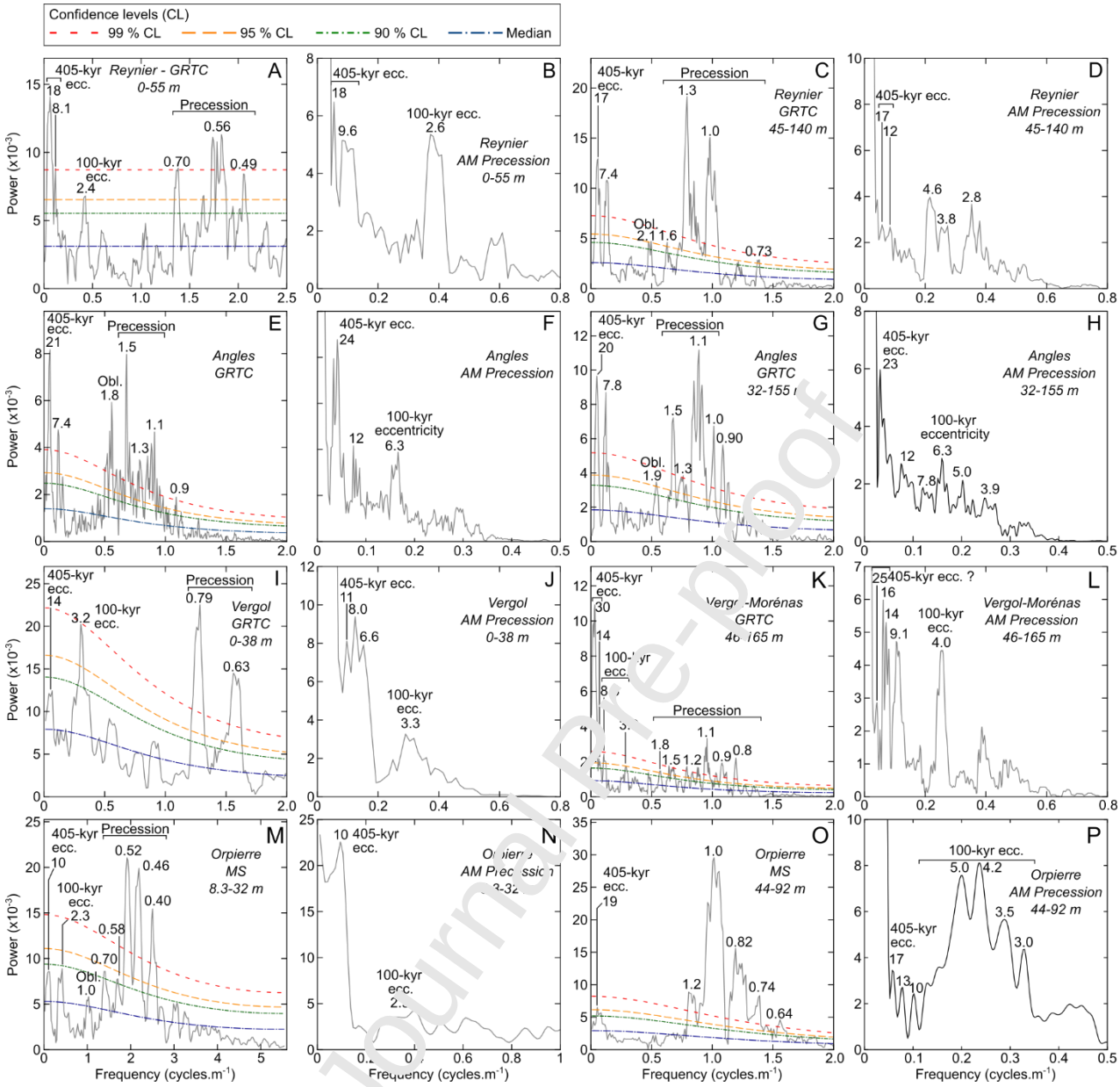

Fig. 14. 2π-Multi-Taper (MTM) of the direct signals and amplitude modulation of the precession cycles from Reynier (**A-D**), Angles (**E-H**), Vergol-Morénas (**I-L**) and Orpierre (**M-P**). Periods are lebeled in meters above correspondant spectral peaks. ecc.: eccentricity, obl.: obliquity, prec.: precession.

Finally, the 405-kyr eccentricity band directly extracted from the GRTC signal of the whole section was filtered applying a bandpass filter with lower and higher frequency cuts at 0.08584 cycles.m^{-1}. From 0 to 55 m, the filter of the 405-kyr eccentricity cycle in the instantaneous amplitude of the precession cycle at

Reynier shows four cycles, namely here B/V to V3, which is one more cycle than the direct filter of the 405-kyr band directly extracted from the GRTC signal (Fig. 13). Interestingly, these four cycles encompass 86 marl-limestone alternations, either an average of 21.5 cycles per 405-kyr cycle and an average period of 18.8 kyr per alternation. These four 405-kyr eccentricity cycles also contain seventeen 100-kyr eccentricity cycles, which corresponds to an average period of 95.3 kyr, in excellent agreement with the mean period of the 100-kyr cycle in the astronomical solution (95.2 kyr). Thus, the sequencing of the 405-kyr eccentricity using the instantaneous amplitude of the precession cycle in interval B/V to V3 agrees with the number of marl-limestone alternations and 100-kyr eccentricity cycles and is preferred for astrochronology to the direct filter of the GRTC signal. The filter of 405-kyr eccentricity cycle is in phase with the direct filter of the GRTC series in cycle B/V. Its amplitude decreases in the upper half of cycle V3 and is no longer useful upward in the Valanginian series. A 405-kyr eccentricity cycle is added here, so that the numbering of 405-kyr cycles differs compared to Martinez et al. (2013) from cycle V3 upward.

In the interval from 45 m to the top of the series, the 405-kyr band extracted from the GRTC signal shows five complete cycles, which encompass *ca.* 90 marl-limestone alternations. On details cycles V4, V5, V7, V8 contain *ca.* 20 alternations, while cycle V6 contains *ca.* 10 alternations. This feature was observed elsewhere in the basin (Martinez et al., 2013; Fig. 13). Conversely, the filter of the 405-kyr eccentricity cycle in the instantaneous amplitude of the precession shows weak amplitudes, in phase with the direct filter in cycle V5, and then inverse phase from the top of V6 in the *K. inostranzewi* Tethyan Ammonite Zone (Fig. 13). This change of phase corresponds to the decrease in carbonate content in the sedimentary series in line with the crisis in carbonate production associated with the Weissert Event. The 405-kyr band filtered from the signal has higher amplitudes than the 405-kyr band filtered from the AM of precession, is in phase with clay mineral assemblages (Martinez et al., 2020b) and is consistent between all the sections considered. Consequently, the 405-kyr band filtered from the signal is much more reliable to establish the sequencing of the 405-kyr cycle in this interval.

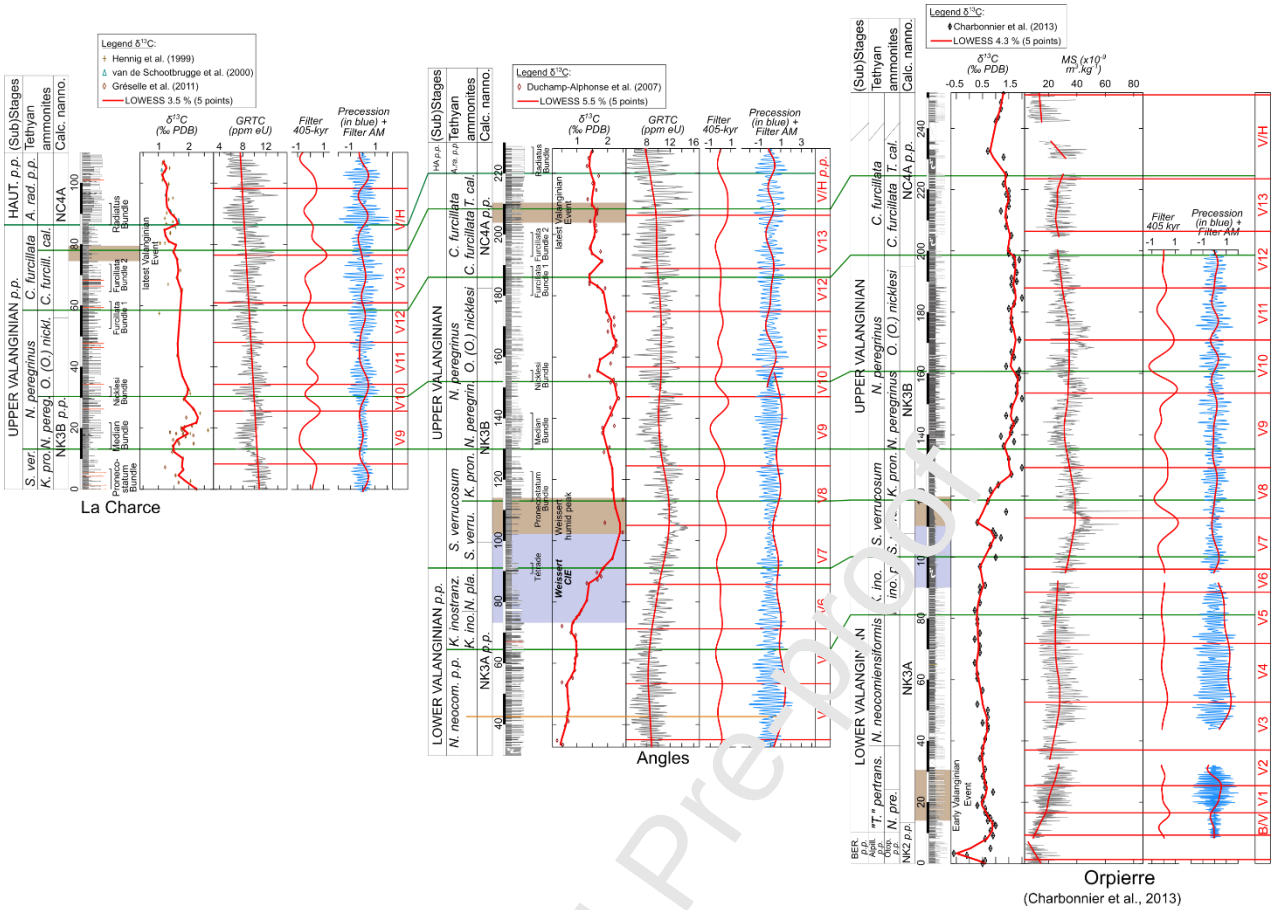

Fig. 15. Correlation of the astrochronologic frameworks from the lower Valanginian to the lower Hauterivian. The $\delta^{13}C_{bulk}$ from La Charce is from Gréselle et al. (2011), Hennig et al. (1999) and van de Schootbrugge et al. (2000). The $\delta^{13}C_{bulk}$ from Angles is from Duchamp-Alphonse et al. (2007). The $\delta^{13}C_{bulk}$ from Orpierre is from Charbonnier et al. (2013).

5.1.2. Spectral analyses of the Angles series – lower Valanginian

The trend of the GRTC series of the Angles section was calculated using the LOWESS method with a coefficient of 0.2 (Fig. 15). The residual series was then standardized. The 2π-MTM spectrum shows spectral peaks above the 99 % confidence level at 21 m, attributed to the 405-kyr eccentricity band, at 7.4 m, at 1.8 m, from 1.5 to 1.1 m, attributed to the precession, and at 0.9 m (Fig. 14E). The 2π-MTM of the instantaneous amplitude of the precession band shows spectral peaks at 24 m, attributed to the 405-kyr eccentricity, and at 6.3 m, attributed to the 100-kyr eccentricity (Fig. 14F). Another peak is observed at 12

m. The precession band was filtered from the GRTC signal applying a bandpass filter with a lower and upper frequency cuts of 0.6161 and 1.0429 cycles.m^{-1}. The 405-kyr eccentricity band was filtered from the GRTC signal applying a lowpass filter with the upper frequency cut of 0.0920 cycles.m^{-1}. The filter of the 405-kyr band from the GRTC signal correlates with Reynier (Figs. 13, 15). As also shown in Martinez et al. (2013), it shows that the thickness of the 405-kyr band varies from 23 m (cycle V9) to 10 m (cycle V10). The 2π-MTM spectrum of the interval covering the base of the series to level 155 m shows the 405-kyr eccentricity band at 20 m and the precession band from 1.5 to 1.1 m (Fig. 14G). The 2π-MTM spectrum of the instantaneous amplitude of the precession band shows the 405-kyr eccentricity band at 23 m, the 100-kyr eccentricity band from 7.8 to 5.0 m and other spectral peaks at 12 and 3.9 m (Fig. 14H). The 405-kyr eccentricity band was filtered from the instantaneous amplitude of the precession band applying a lowpass filter with the upper frequency cut of 0.0613 cycles.m^{-1}. The filter of the 405-kyr band from the instantaneous amplitude of the precession band is in phase with the filter of the 405-kyr band from the GRTC signal up to the upper boundary of cycle V5 and in inverse phase from the base of cycle V7 to the top of cycle V9 (Fig. 13).

5.1.3. Spectral analyses of the Vergol-Morétas series

The trend of the GRTC series of the Vergol section below the slump (0-38 m) was calculated applying a best-fit linear regression. The residual series was then standardized. The 2π-MTM spectrum shows significant cycles above the 99 % confidence level at 0.79 m and 0.63 m attributed to the precession, and a significant peak above the 95 % confidence level at 3.2 m, attributed to the 100-kyr eccentricity cycle (Fig. 14I). A peak at 14 m is also observed and attributed to the 405-kyr eccentricity cycle. The 2π-MTM spectrum of the instantaneous amplitude of the precession band shows a peak at 3.3 m attributed to the 100-kyr eccentricity cycle, a peak at 11 m attributed to the 405-kyr eccentricity cycle and peaks at 8.0 and 6.6 m (Fig. 14J). The precession band was filtered from the GRTC signal applying a bandpass filter with lower and higher frequency cuts at 1.0635 cycles.m^{-1} and 1.7265 cycles.m^{-1}. The 100-kyr eccentricity band was filtered from the GRTC signal applying a bandpass filter with lower and higher frequency cuts at 0.2072

cycles.m^{-1} and 0.4144 cycles.m^{-1}. The 405-kyr eccentricity band was filtered from the GRTC signal applying a lowpass filter with a higher frequency cut at 0.1243 cycles.m^{-1} and was filtered from the instantaneous amplitude of the precession band applying a lowpass filter with a higher frequency cut at 0.1105 cycles.m^{-1}.

The filter of peak at 11 m from the instantaneous amplitude of the precession band correlates with the filter of this band at Reynier (Fig. 13). Cycles B/V to V2 encompass twelve 100-kyr eccentricity cycles and 34 marl-limestone alternations, corresponding to an average of 17 marl-limestone alternations per 405-kyr eccentricity cycle. As in Reynier, the 405-kyr band directly filtered from the GRTC signal and filtered from the instantaneous amplitude of the precession band are in phase in cycle B/V. In the interval 0-38 m of the Vergol-Morénas section, the filter of the 405-kyr band from the instantaneous amplitude of precession is thus preferred to the direct filter of the GRTC signal.

Above the slump (46 m to the top), the trend of the GRTC series was calculated using the LOWESS method with a coefficient of 0.5 (Fig. 13). The residual series was then standardized. The 2π-MTM spectrum shows spectral peaks above the 99 % confidence level at 30 m and from 1.5 to 0.8 m (Fig. 14K). Spectral peaks above the 95 % confidence level are observed at 14 m, 8.8 m, 3.6 m and 1.8 m. The peaks from 14 to 30 m are attributed to the 405-kyr eccentricity cycles, the peaks at 8.8 and 3.6 m to the 100-kyr eccentricity cycles and the peaks from 1.8 to 0.8 m to the precession cycles. The range of periods covered by each band reflects the progressive increase in sedimentation rate due to the increase in detrital supply from the lower to the upper Valanginian (Martinez, 2018). The 2π-MTM spectrum of the instantaneous amplitude of the precession band in the upper part of the Vergol-Morénas series shows spectral peaks from 25 to 14 m, in the 405-kyr eccentricity band, a peak at 9.0 m and at 4.0 m, in the 100-kyr eccentricity band (Fig. 14L). The precession band was filtered from the GRTC signal applying a bandpass filter with lower and higher frequency cuts at 0.5189 cycles.m^{-1} and 1.4003 cycles.m^{-1}. The 405-kyr eccentricity band was filtered from the GRTC signal applying a lowpass filter with higher frequency cuts at 0.0700 cycles.m^{-1} and was filtered from the instantaneous amplitude of the precession band applying a bandpass filter with lower and higher frequency cuts at 0.0329 cycles.m^{-1} and 0.0659 cycles.m^{-1}.

The filter of the 405-kyr eccentricity band from the instantaneous amplitude of the precession shows much lower amplitudes than in the Berriasian-Valanginian boundary interval and shall not be used for astrochronology (Fig. 13). The filter of the 405-kyr eccentricity cycle from the GRTC signal shows high amplitudes and correlates with Reynier from the base of cycle V7 to the base of cycle V9. The boundaries of 405-kyr cycles from the base of cycle V4 to the base of cycle V6 are correlated to Reynier and Angles.

5.1.4. Spectral analyses of the Orpierre series – lower Valanginian

The MS signal at Orpierre shows a progressive increase in thickness from 10 to 32 m, in line with a rapid increase in amplitude, reflecting the progressive enrichment in detrital component observed at Reynier and Vergol (Fig. 13). The spectral analyses in the lower Valanginian of Orpierre was subdivided into two intervals to account this change in sedimentation rate and the two observation hiatuses above level 32 m and below level 44 m (Fig. 13).

The trend of the Orpierre series from 8.3 to 32 m was calculated using the LOWESS method with a coefficient of 0.5 (Fig. 13). The residual series was then standardized. The 2π-MTM spectrum shows spectral peaks above the 99 % confidence level from 0.52 to 0.40 m (Fig. 14M). Additional peaks are observed at 10 m, 2.3 m, 1.0 m, 0.70 m and 0.58 m below the 95 % confidence level. The peak at 10 m is attributed to the 405-kyr eccentricity cycle, the peak at 2.3 m to the 100-kyr eccentricity cycle and the peak at 1.0 m to the obliquity. The peaks at 0.70 and 0.58 m are within the precession band and correspond to the increase in the thickness of the marl-limestone alternations. The 2π-MTM spectrum of the instantaneous amplitude of the precession band from 8.3 to 32 m shows periods at 10 m related to the 405-kyr eccentricity, and at 2.9 m related to the 100-kyr eccentricity (Fig. 14N). The precession band was filtered from the GRTC signal applying a bandpass filter with lower and higher frequency cuts at 1.3468 cycles.m^{-1} and 2.8199 cycles.m^{-1}. The 100-kyr eccentricity band was filtered from the GRTC signal applying a bandpass filter with lower and higher frequency cuts at 0.2946 cycles.m^{-1} and 0.5051 cycles.m^{-1}. The 405-kyr eccentricity band was filtered from the GRTC signal applying a lowpass filter with a higher frequency cut at 0.2104 cycles.m^{-1} and from the instantaneous amplitude of the precession band with a

lowpass filter applying a higher frequency cut of 0.1473 cycles.m^{-1}. The 405-kyr band filtered from the GRTC signal correlates with Reynier and Vergol-Morénas. In particular, the lower and higher boundaries of cycles B/V are identified. The filter of the 405-kyr band from the instantaneous amplitude of the precession band shows maxima at the lower boundaries of B/V and V2. It however does not show the maximum in the lower boundary of V1 because of the trend in rapid increase in amplitudes of the precession cycle observed in the MS signal of Orpierre. Here, the lower boundary of V1 is located on the maximum of the filter of 405-kyr band from the GRTC signal, which correlates with Reynier and Vergol-Morénas.

The trend of the Orpierre series from 44 to 92 m was calculated using the LOWESS method with a coefficient of 0.5 (Fig. 13). The residual series was then standardized. The 2π-MTM spectrum shows spectral peaks above the 99 % confidence level from 1.2 to 0.64 m, linked to the marl-limestone alternations and attributed to the precession cycle (Fig. 14O) and a peak above the 95 % confidence level at 19 m, attributed to the 405-kyr eccentricity cycle. The 2π-MTM spectrum of the instantaneous amplitude of the precession band in this interval shows a peak at 17 m, attributed to the 405-kyr eccentricity cycle, peaks from 5.0 m to 3.0 m, attributed to the 100-kyr eccentricity, and peaks at 13 m and 10 m (Fig. 14P). The precession band was filtered from the GRTC signal applying a bandpass filter with lower and higher frequency cuts at 0.7582 cycles.m^{-1} and 1.4233 cycles.m^{-1}. The 405-kyr eccentricity band was filtered from the GRTC signal applying a lowpass filter with a higher frequency cut at 0.0627 cycles.m^{-1} and from the instantaneous amplitude of the precession band applying a lowpass filter with a higher frequency cut at 0.06798 cycles.m^{-1}. The boundaries of the filter of the 405-kyr eccentricity band from the MS signal correlate with Reynier and Angles and with the filter of the 405-kyr band in the instantaneous amplitude of the precession band of Orpierre (Figs. 13, 15).

5.2. Extraction of the 405-kyr eccentricity in the upper Valanginian

5.2.1. Spectral analyses of the Orpierre series – upper Valanginian

The calibration of the Late Valanginian Subtage is based on the filter of the 405-kyr eccentricity cycle from

the Angles, La Charce-Pommerol and Orpierre sections (Charbonnier et al., 2013; Martinez et al., 2013). The trend of the MS series of the Orpierre section was calculated from 95 to 200 m using the LOWESS method with a coefficient of 0.2 (Fig. 13). The residual series was then standardized. The 2π-MTM spectrum shows spectral peaks above the 99 % confidence level at 18 m, attributed to the 405-kyr eccentricity cycle, and from 1.5 to 0.8 m, attributed to the precession cycle (Fig. 16A). The spectrum of the instantaneous amplitude of the precession band shows spectral peaks at 16 m, attributed to the 405-kyr eccentricity cycle, and from 6.1 to 3.9 m, attributed to the 100-kyr eccentricity cycle (Fig. 16B). Another peak is observed at 3.1 m. The precession band was filtered from the MS signal applying a bandpass filter with a lower and upper frequency cuts at 0.6446 and 1.2134 cycles.m^{-1}. The 405-kyr eccentricity band was filtered from the MS signal applying a lowpass filter with the upper frequency cut of 0.1138 cycles.m^{-1} and from the instantaneous amplitude of the precession cycle applying a bandpass filter with lower and higher frequency cuts of 0.0284 cycles.m^{-1} and 0.1043 cycles.m^{-1}. The interval V7 to V11 is bounded from the filter of the 405-kyr eccentricity cycle from the MS signal (Figs. 13, 15). It contains 93 precession cycles, which corresponds to 18.6 precession cycles per 405-kyr cycle on average, either an average period of the precession cycle of 21.8 kyr. The 405-kyr band filtered from the instantaneous amplitude of the precession cycle shows a broad reverse correlation with the 405-kyr band filtered from the MS band, in line with the correlation observed in Reynier and Vergol in cycles V7 and V8 (Fig. 13).

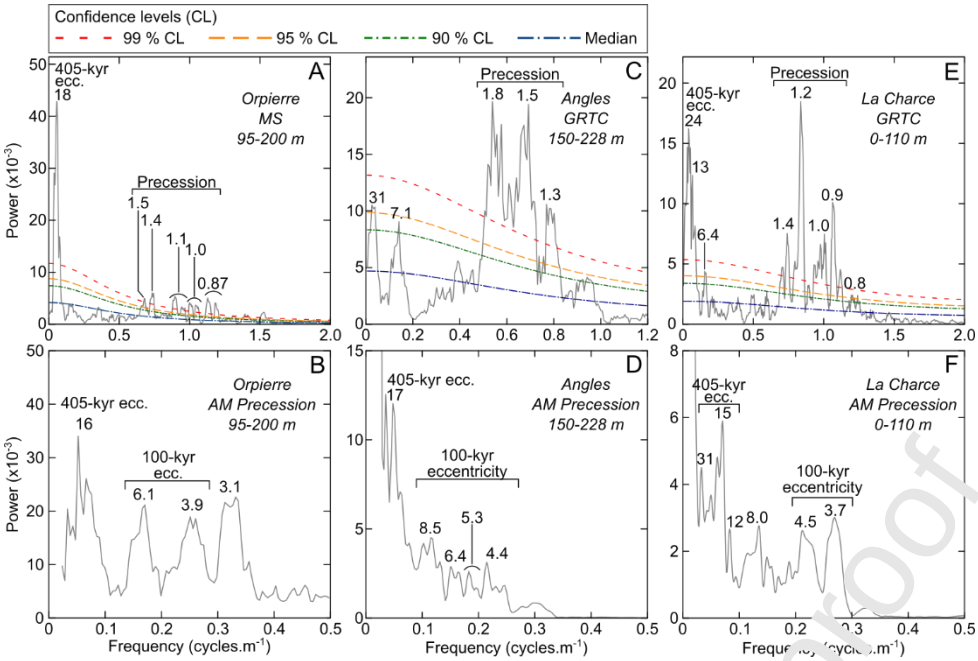

Fig. 16. 2π-Multi-Taper (MTM) spectra of the direct signals and amplitude modulation of the precession cycles from Orpierre (**A-B**), Angles (**C-D**) and La Charce (**E-F**). Periods are labeled in meters above the correspondant spectral peak. ecc.: eccentricity, obl.: obliquity, prec.: precession.

5.2.2. Spectral analyses of the Angles series – upper Valanginian

The 2π-MTM spectrum of the Angles section from 150 m to the top of the series shows spectral peaks above the 99 % confidence level at 1.8, 1.5 and 1.2 m attributed to the precession cycle (Fig. 14C), a peak above the 95 % confidence level at 31 m, and a peak above the 90 % confidence level at 7.1 m. The 2π-MTM spectrum of the instantaneous amplitude of the precession cycle shows cycles at 17 m, attributed to the 405-kyr eccentricity band and from 8.5 to 4.4 m, attributed to the 100-kyr eccentricity band (Fig. 14D). The precession band was filtered from the GRTC signal applying a bandpass filter with lower and upper frequency cuts at 0.4744 cycles.m^{-1} and 0.8365 cycles.m^{-1}. The 405-kyr band was filtered from the instantaneous amplitude of the precession band applying a bandpass filter with lower and upper frequency cuts at 0.0897 cycles.m^{-1} and 0.2564 cycles.m^{-1}. As in Orpierre, the base of cycle V12 corresponds to a minimum in the 405-kyr band filtered from the instantaneous amplitude of the precession band (Fig. 15). Then, the base of cycles V13 and V/H correspond to a maximum in the 405-kyr band filtered from the

instantaneous amplitude of the precession band, showing a progressive change of phasing between the 405-kyr band filtered from the GRTC signal and the same band filtered from the instantaneous amplitude of the precession cycle.

5.2.3. Spectral analyses of the La Charce series – upper Valanginian

The trend of the La Charce series from 0 to 110 m was calculated using a best-fit linear regression (Fig. 15). The residual series was then standardized. The 2π-MTM shows spectral peaks at 24 m and 13 m, attributed to the 405-kyr eccentricity cycle, at 6.4 m, and from 1.4 to 0.9 m, attributed to the precession (Fig. 14E). The 2π-MTM of the instantaneous amplitude of the precession band shows spectral peaks from 31 to 12 m attributed to the 405-kyr band, at 8.0 m, and from 4.5 to 3.7 m, attributed the 100-kyr eccentricity (Fig. 14F). The precession band was filtered applying a bandpass filter with a lower and upper frequency cuts of 0.7727 and 1.1455 cycles.m^{-1}. The 405-kyr eccentricity band was filtered from the GRTC signal applying a lowpass filter with the upper frequency cut of 0.1227 cycles.m^{-1} and from the instantaneous amplitude of the precession band applying a bandpass filter with lower and higher frequency cuts at 0.02727 cycles.m^{-1} and 0.0977 cycles.m^{-1}. The 405-kyr band filtered from the GRTC signal correlates with Angles and Orpierre. The 405-kyr band filtered from the instantaneous amplitude of the precession band generally shows minimum amplitudes at maxima of the 405-kyr band from the GRTC signal, in line with the correlation observed at Orpierre, but not in line with the correlation observed at Angles in cycles V13 and V/H.

5.3. Summary of the calibration of the Valanginian Stage

In the interval B/V–V2, the 405-kyr band filtered from the instantaneous amplitude of the precession cycles are much consistent with the number of marl-limestone alternations and 100-kyr eccentricity cycles than the 405-kyr band filtered from the GRTC signal (Fig. 13). Conversely, the interval from cycle V3 to H1 is consistent with the number of marl-limestone alternations, the bundles of limestone beds used as correlation markers throughout the basin (Fig. 7; see also Charbonnier et al., 2013) and to the number of

100-kyr eccentricity cycles at the Valanginian-Hauterivian transition (Fig. 8). The sequencing of the 405-kyr eccentricity cycle in the Valanginian Stage is thus based on the filter of the instantaneous amplitude of the precession cycle in cycles B/V, V1 and V2 and based on the filter of the 405-kyr band from the GRTC signal from cycle V3 to H1. The duration of the Valanginian Stage revised here from our interpretation of the 405-kyr sequencing is 5.81 Myr.

Compared to Martinez et al. (2013), this duration is 0.72 Myr longer. It is due to the reinterpretation of the 405-kyr sequencing in the Early Valanginian, in line with the number of precession and 100-kyr eccentricity cycles in the B/V–V2 interval (Fig. 13) and to the revised biostratigraphy of Vergol (Kenjo et al., 2021), which locates the base of the *"T." pertransiens* Tethyan Ammonite Zone three 100-kyr eccentricity cycles lower than Blanc (1996). The 405-kyr eccentricity cycle is best recorded throught the amplitude modulation of the precession cycles at the Berriasian-Valanginian transition, where the carbonate fraction is the highest. Comparatively, the 405-kyr eccentricity cycle is best expressed in the remaining part of the Valanginian, where the detrital fraction is higher (Fig. 15).

In a given stratigraphic interval and geographic setting, detrital proxies tend to record longer cycles compared to carbonate-related proxies (Martinez, 2018). In the astronomical series, the energy of the eccentricity is contained within the amplitude of the precession cycles. The direct expression of the amplitude of the 405-kyr eccentricity in the GRTC series reflects non-linear processes affecting detrital sediment supply and acting as natural lowpass filters. They thus attenuate the amplitude of the precession cycles and enhance the expression of the 405-kyr eccentricity cycles (Martinez, 2018). The duration of pedogenesis (up to 10^5 years; Lin, 2011) or duration of transport of detrital particles (Jerolmack and Paola, 2010) are examples of such processes. Comparatively, carbonate systems are much more dynamic and able to respond within Milankovtich timescales (Pittet et al., 2000; Strasser, 2018). These different dynamics could explain the better preservation of the 405-kyr eccentricity cycle in the amplitude modulation of the precession cycles in carbonated intervals, while this cycle is better preserved independently of the precession cycles in detrital-dominated intervals.

6. Calibration of the Hauterivian Stage

6.1. Extraction of the 405-kyr eccentricity in the Hauterivian

6.1.1. Spectral analyses of the Río Argos series

The trend of the GRTC series of the Río Argos section was calculated using the LOWESS method with a coefficient of 0.2 (Fig. 17). The residual GRTC series was then standardized. The spectrum of the GRTC series from 0 to 80 m shows the precession cycle with periods ranging from 1.3 to 1.0 m, obliquity cycle at 1.8 m and the 100-kyr eccentricity cycle from 7.6 to 5.2 m (Fig. 18A). The 100-kyr eccentricity band was filtered applying lower and higher frequency cuts at 0.1188 and 0.2500 cycles.m^{-1}. The precession band was filtered applying lower and higher frequency cuts at 0.7250 and 1.250 cycles.m^{-1} (Fig. 18A). The spectrum of the instantaneous amplitude of the precession band shows spectral peaks at 25 m and 15 m, related to the 405-kyr cycle, and at 6.0 and 4.5 m, related to the 100-kyr cycle (Fig. 18B). The 405-kyr band was filtered from the instantaneous amplitude of the precession band using a Taner lowpass filter applying a higher frequency cut at 0.0750 cycles m^{-1} (Fig. 18B).

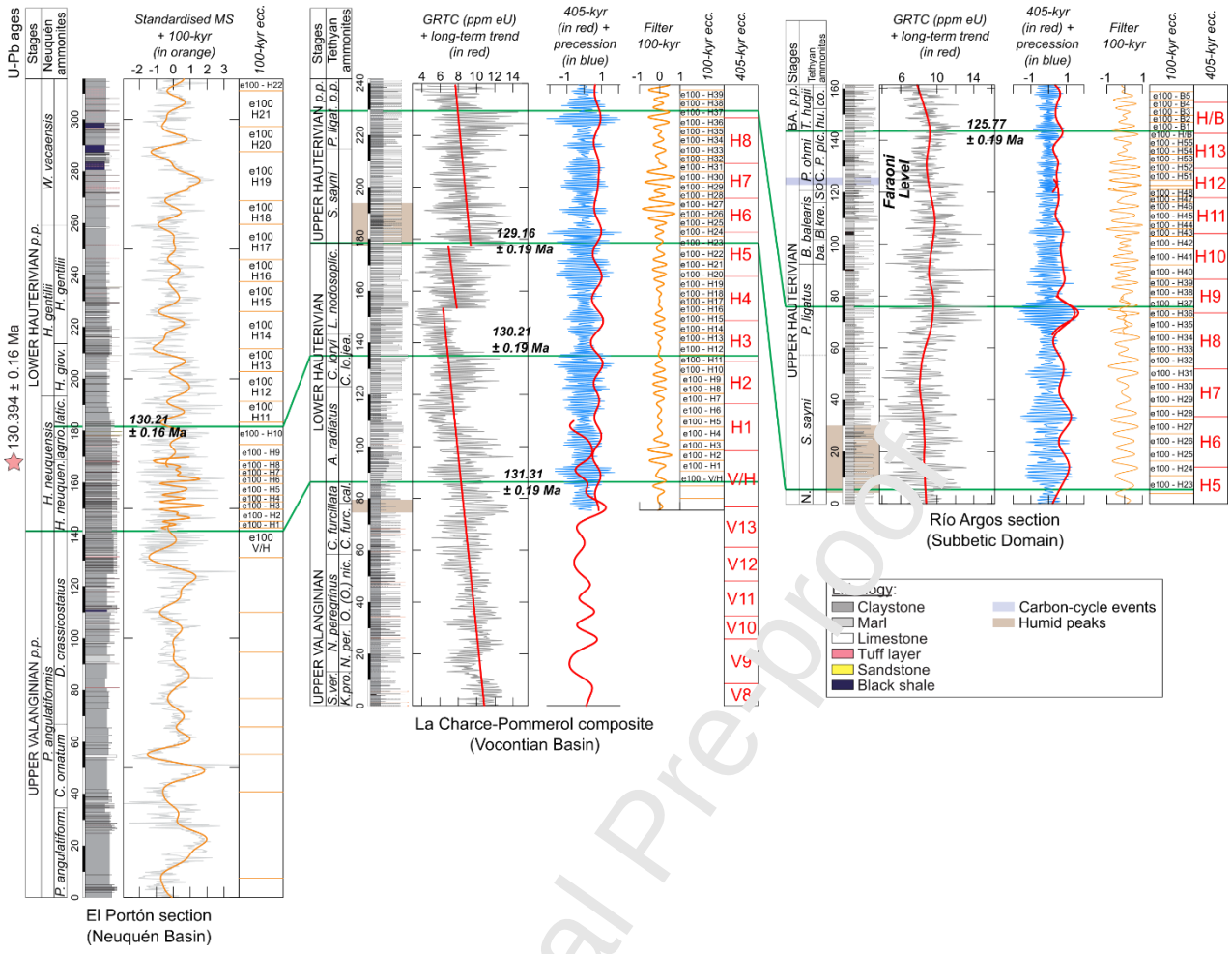

Fig. 17. Correlation of the astrochronologic frameworks from the upper Valanginian to the lowermost Barremian. Magnetic Susceptibility data (MS) is from Aguirre-Urreta et al. (2019). Gamma-Ray Total Count data (GRTC) are from Martinez et al. (2013, 2015).

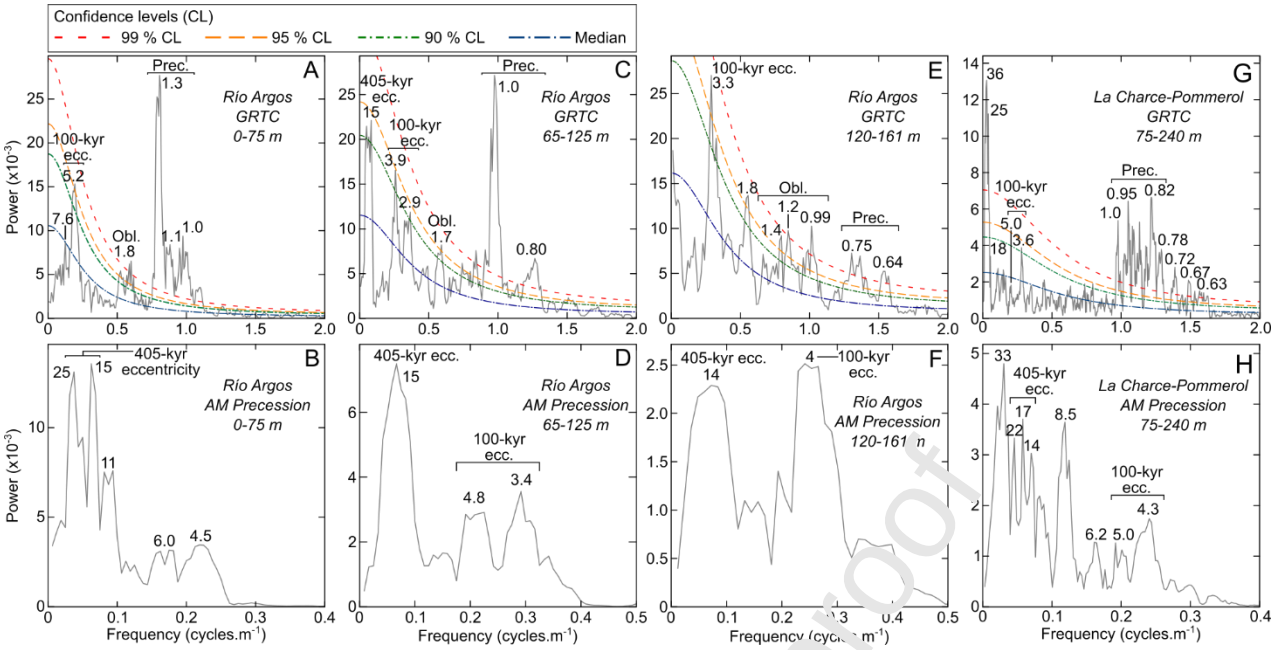

Fig. 18. 2π-Multi-Taper (MTM) spectra of GRTC signals and amplitude modulation of the precession cycles from Río Argos (**A-F**) and La Charce-Pommerol (**G-H**). Periods are labeled in meters; ecc.: eccentricity, obl.: obliquity, prec.: precession.

The spectrum of the GRTC series from 65 to 125 m shows the 405-kyr cycle at 15 m, the 100-kyr cycle from 3.9 to 2.9 m, the obliquity cycle at 1.7 m and the precession cycle from 1.0 to 0.8 m (Fig. 18C). The 100-kyr eccentricity band was filtered applying lower and higher frequency cuts at 0.2133 and 0.4200 cycles.m^{-1}. The precession band was filtered applying lower and higher frequency cuts at 0.8883 and 1.3467 cycles.m^{-1}. The spectrum of the instantaneous amplitude of the precession band shows spectral peaks at 15 m, related to the 405-kyr cycle, and from 4.8 to 3.4 m, related to the 100-kyr eccentricity (Fig. 18D). The 405-kyr band was filtered from the instantaneous amplitude of the precession band using a Taner lowpass filter applying a higher frequency cut at 0.1200 cycles.m^{-1}.

The spectrum of the GRTC series from 120 to 161 m shows the 100-kyr cycle at 3.3 m, the obliquity from 1.4 to 0.99 m and the precession from 0.75 to 0.64 m (Fig. 18E). The 100-kyr eccentricity band was filtered applying lower and higher frequency cuts at 0.2005 and 0.3744 cycles.m^{-1}. The precession band was filtered applying lower and higher frequency cuts at 1.1377 and 1.6304 cycles.m^{-1}. The spectrum of the

instantaneous amplitude of the precession band shows spectral peaks at 14 m, related to the 405-kyr cycle and at 4 m, related to the 100-kyr cycle (Fig. 18F). The 405-kyr band was filtered from the instantaneous amplitude of the precession band using a Taner lowpass filter applying a higher frequency cut at 0.1207 cycles.m^{-1}.

The filter of the 405-kyr band in the instantaneous amplitude of precession in the Río Argos series shows 9 complete 405-kyr eccentricity cycles, labeled H6 to H/B, and 36 repetitions of the 100-kyr eccentricity cycle, labeled "e100-H24"to "e100-B4" (Fig. 17).

6.1.2. Spectral analyses of the La Charce-Pommerol series

The trend of the GRTC series of the La Charce-Pommerol section was calculated using three best-fit linear regressions (Fig. 17). The detrended GRTC series was then standardized. The 2π-MTM spectrum of the GRTC series from 75 to 240 m shows high-power spectral peaks from 36 to 18 m and from 1.0 to 0.78 m (Fig. 18G). Additional peaks are observed with lower amplitudes at 3.6 m and from 0.72 to 0.63 m. The peaks from 1.0 to 0.78 m correspond to the thickness of the marl-limestone alternations and are related to the precession cycles. The band from 5.0 to 3.6 m corresponds to the 100-kyr eccentricity cycle. The spectrum of the instantaneous amplitude of the precession band shows spectral peaks at 33 m, 22 m, 17 m, 14 m, 8.5 m, 6.2 m, 5.0 m and 4.2 m (Fig. 18H). The cluster of peaks from 22 to 14 m reflect the 405-kyr eccentricity cycle, while the peaks from 5.0 to 4.3 m are related to the 100-kyr eccentricity cycles. The precession band was filtered applying a bandpass filter with the lower frequency cut at 0.9318 cycles.m^{-1} and the upper frequency cut at 1.3216 cycles.m^{-1}. The 100-kyr eccentricity band was filtered applying a bandpass filter with lower and upper frenquency cuts at 0.1857 and 0.3076 cycles.m^{-1}. The 405-kyr band was filtered from the instantaneous amplitude of the precession band in the Hauterivian part of the La Charce-Pommerol series using lower and higher frequency cuts of 0.0396 and 0.0761 cycles.m^{-1} (Fig. 18H). The filter of the 405-kyr band in the instantaneous amplitude of precession shows 8 complete repetitions of the 405-kyr cycles in the Hauterivian part of the La Charce-Pommerol section, labeled as H1 to H8 (Fig.17).

6.2. Summary of the calibration of the Hauterivian Stage

From the base of cycle H1 to the top of cycle H8 at La Charce-Pommerol, a total of 34 repetitions of 100-kyr cycles and 162.5 marl-limestone alternations are observed. It leads to average periods of 95.3 and 19.9 kyr for the 100-kyr eccentricity and the precession, respectively. In the El Portón section (Neuquén Basin), *ca.* 22 repetitions of the 100-kyr cycles have been identified in the lower Hauterivian (Aguirre-Urreta et al., 2019), compared to 23 at La Charce-Pommerol (Fig. 17). In the upper Hauterivian, the GRTC of the La Charce-Pommerol and Río Argos sections can be correlated using ammonite zonation and a rapid increase in the GRTC values in the *P. ligatus* Tethyan ammonite Zone (Fig. 17). This interval encompasses *ca.* 3.5 repetitions of the 405-kyr cycles (labeled as H5 to H9), and *ca.* 14 repetitions of the 100-kyr cycles labeled as H23 to H37 in both sections. This new astrochronology of the Hauterivian with the 100-kyr and 405-kyr eccentricity cycles provides a consistent age model between the Neuquén, Vocontian and Subbetic basins. The duration of the Hauterivian Stage revised here from our interpretation of the 405-kyr sequencing is 5.54 Myr.

The band-pass filtering and instantaneous amplitude of the precession cycle at La Charce-Pommerol shows a consistent timescale with the astrochronology of the Pilmatué Member and the number of marl-limestone couplets based on the record of the 405-kyr eccentricity cycle (Fig. 17). The duration of the Late Hauterivian provided here (3.39 Myr) is in addition longer than the duration proposed in Aguirre-Urreta et al. (2019) [3.02 Myr]. The difference is due to the use of the 405-kyr eccentricity cycle to calibrate the Río Argos section in this study, while it was previously calibrated with the 100-kyr eccentricity cycle. Correlations between Río Argos and other sections in the Subbetic Domain (Arroyo Gilico and Barranco Cavila; Martinez et al., 2020a) demonstrates that not all 100-kyr eccentricity cycles are preserved in a given section of the Subbetic Domain, while all the 405-kyr eccentricity cycles are preserved. Calculating stage durations with the 405-kyr eccentricity here prevents underestimation of the stage duration because of non-deposition of the short cycles.

7. Calibration of the Barremian Stage

7.1. Extraction of the 405-kyr eccentricity in the Arroyo Gilico section

The trend of the MS series of the Arroyo Gilico section was calculated using a LOWESS regression with a coefficient of 0.25 (Fig. 19). The 2π-MTM spectrum of the Arroyo Gilico series shows spectral peaks above the 95 % confidence level at 11 m and 6.5 m, attributed to the 405-kyr eccentricity cycle, from 3.6 to 1.6 m, attributed to the 100-kyr eccentricity cycle, and from 0.80 to 0.37 m, attributed to the precession cycle (Fig. 20A). The large variability of each band is due to variations in the sedimentation rate, as depicted in Martinez et al. (2020a). The 2π-MTM spectrum of the instantaneous amplitude of the precession band shows a main spectral peak at 10 m, attributed to the 405-kyr band (Fig. 20B). The precession band was filtered from the MS signal applying a bandpass filter with lower and higher frequency cuts of 1.0433 and 3.0230 cycles.m^{-1}. The 100-kyr eccentricity band was filtered from the MS signal applying a bandpass filter with lower and higher frequency cuts of 0.1873 and 0.6889 cycles.m^{-1}. The 405-kyr eccentricity band was filtered from the MS signal applying a lowpass filter with a higher frequency cut of 0.1873 cycles.m^{-1} and from the instantaneous amplitude of the precession band applying a bandpass filter with lower and higher frequency cut of 0.05350 and 0.1940 cycles.m^{-1}. Maxima of 405-kyr filtered from the MS signal generally correspond to maxima of the 405-kyr filtered from the instantaneous amplitude of the precession cycle. Only one exception is observed at boundary between H/B and B1 (Fig. 19).

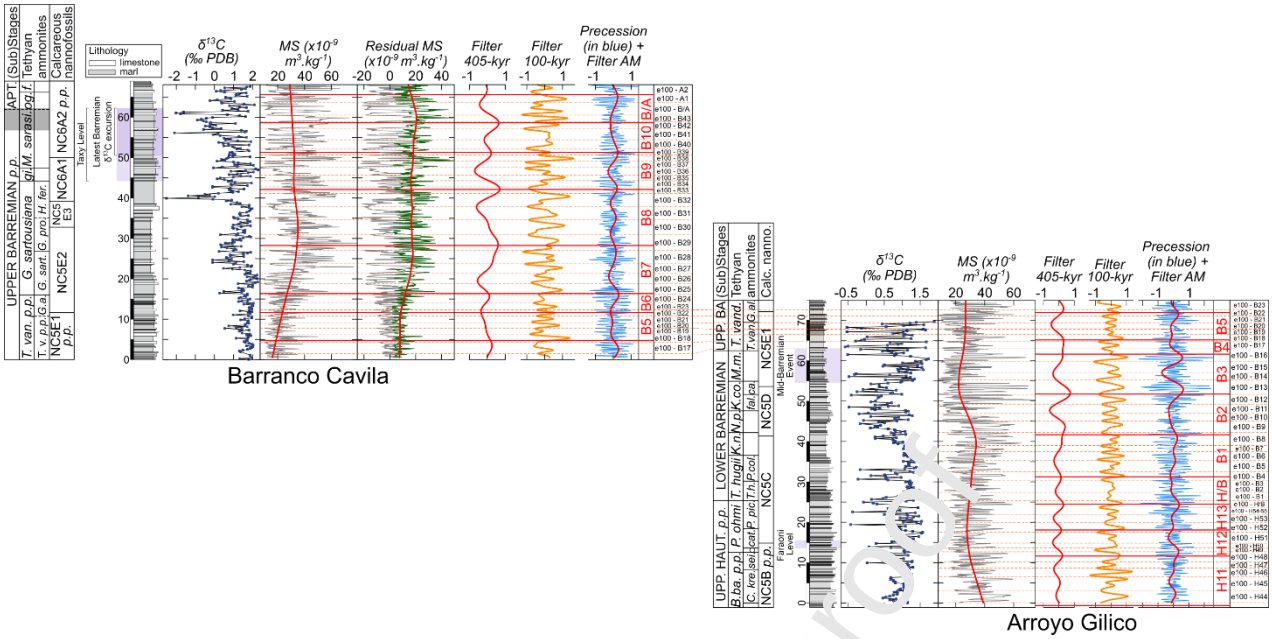

Fig. 19. Correlation of the astrochronologic frameworks from the upper Hauterivian to the lowermost Aptian. Magnetic Susceptibility data (MS) is from Martinez et al. (2020a).

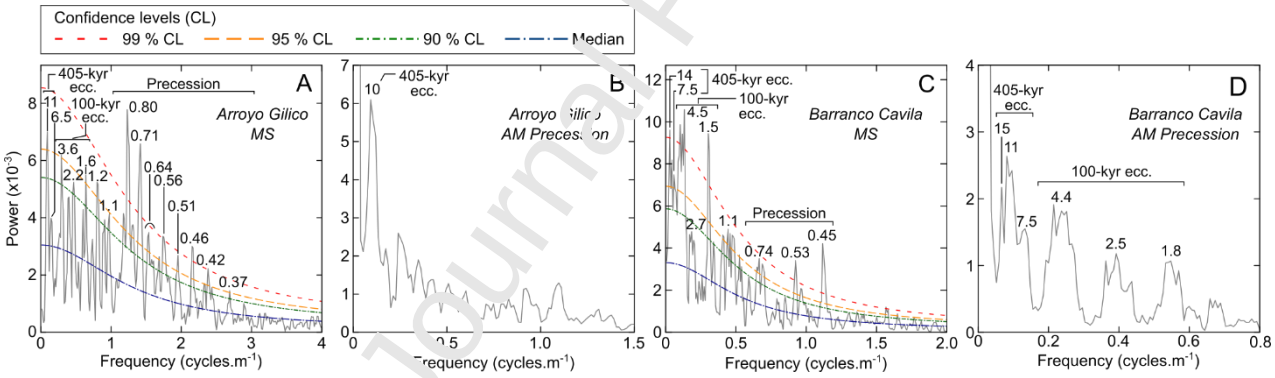

Fig. 20. 2π-Multi-Taper (MTM) spectra of MS signals and amplitude modulation of the precession cycles from Arroyo Gilico (**A-B**) and Barranco de Cavila (**C-D**). Periods are labeled in meters; ecc.: eccentricity, obl.: obliquity, prec.: precession.

7.2. Extraction of the 405-kyr eccentricity in the Barranco de Cavila section

The trend of the MS series of the Barranco de Cavila section was calculated first using a LOWESS regression with a coefficient of 0.5. Then, a LOWESS regression was performed on the instantaneous

amplitude of the residual series with a coefficient of 0.2. The variance of the residual series was detrended by dividing the residual series to the LOWESS regression of the instantaneous amplitude of the residual series (Fig. 19). The 2π-MTM spectrum of the Barranco de Cavila series shows spectral peaks above the 99 % confidence level at 14 m, 4.5 m, 1.5 m, 0.53 m and 0.45 m (Fig. 20C), and spectral peaks above the 95 % confidence level at 7.5 m, 1.1 m and 0.74 m. The 405-kyr eccentricity band ranges from 14 to 7.5 m, and locally to 4.5 m around level 15 m (Martinez et al., 2020a). The 100-kyr eccentricity band ranges from 4.5 to 1.5 m, and the precession band from 0.74 to 0.45 m. The 2π-MTM spectrum of the instantaneous amplitude of the precession band shows spectral peaks from 15 to 7.5 m, attributed to the 405-kyr eccentricity band and from 4.4 to 1.8 m, attributed to the 100-kyr eccentricity band (Fig. 20D). The precession band was filtered from the MS signal applying a bandpass filter with higher and lower frequency cuts of 1.1399 and 2.3686 cycles.m^{-1}. The 100-kyr eccentricity band was filtered from the MS signal applying a bandpass filter with higher and lower frequency cuts of 0.1628 and 0.7476 cycles.m^{-1}. The 405-kyr eccentricity band was filtered from the MS signal applying a lowpass filter with a higher frequency cut of 0.1628 cycles.m^{-1}, and from the instantaneous amplitude of the precession band applying a bandpass filter with lower and higher frequency cuts of 0.0555 and 0.1628 cycles.m^{-1}. Maxima of 405-kyr filtered from the MS signal generally correspond to maxima of the 405-kyr filtered from the instantaneous amplitude of the precession cycle. Two exceptions are observed at boundary between B5-B6 and B10-B/A (Fig. 19).

7.3. Summary of the calibration of the Barremian Stage

The sequencing of the 405-kyr eccentricity cycle in the Barremian Stage is based on the 405-kyr band filtered from the MS signal. The duration of the Barremian Stage remains unchanged compared to Martinez et al. (2020a) at $4.58^{+0.15}_{-0.29}$ Myr.

8. Construction of the Geological Time Scale

8.1. Ages of stages, ammonite zones and calcareous nannofossil zones

At El Portón, the base of the *O. (O.) laticosta* Andean ammonite Subzone is dated at 130.21 ± 0.16 Ma, from integrated radio-astrochronology (Aguirre-Urreta et al., 2017, 2019) (Fig. 17). The base of the *O. (O.) laticosta* Subzone is correlated to the base of the *Olcostephanus (Jeannoticeras) jeannoti* Tethyan ammonite Subzone at La Charce-Pommerol. Counting the 100-kyr cycle from the base of the Hauterivian, this correlation line corresponds to cycle "e100-H10" at El Portón, and to cycle "e100-H11" at La Charce-Pommerol. An additional uncertainty of 0.1 Myr thus arises from the correlation from the Neuquén to the Vocontian Basin. The uncertainty from the U-Pb age (0.16 Myr) is independent from the uncertainty from the Neuquén-Vocontian basins correlation (0.10 Myr). The combined standard uncertainty of the numerical ages in the Vocontian Basin is $\sqrt{0.16^2 + 0.10^2}$ = 0.19 Myr. Anchoring the age of the base of the *O. (J.) jeannoti* Tethyan ammonite Zone at 130.22 ± 0.19 Ma to the 405-kyr sequencing leads to an age of the Valanginian/Hauterivian boundary at 131.25 ± 0.19 Ma, an age of the Berriasian/Valanginian boundary of 137.06 ± 0.19 Ma, an age of the Hauterivian/Barremian boundary at 125.71 ± 0.19 Ma and an age of the Barremian/Aptian boundary at 121.15 ± 0.31 Ma. The uncertainty corresponds to the combined standard uncertainties from the U-Pb age (0.16 Myr), the uncertainty from the Neuquén-Vocontian basins correlation (0.10 Myr) and the biostratigraphic uncertainty on the location of the Barremian-Aptian boundary. In addition, to the ages of the stages, we provide here the ages of Tethyan ammonite zones and subzones and the calcareous nannofossil zones and subzones (Tables 1-3).

A recent U-Pb ID-TIMS age of 123.1 ± 0.3 Ma was calculated on zircons from a bentonite layer calibrated to the uppermost part of magnetochron M1r in Svalbard Islands (Midtkandal et al., 2016; Zhang et al., 2021). This interval stratigraphically corresponds to the transition between the *Toxancyloceras vandenheckii* and the *Gerhardtia sartousiana* Tethyan Ammonite zones, dated in our age model at 122.96 ± 0.19 Ma. ^{40}Ar-^{39}Ar ages indicate an age of chron M0r of 121.2 ± 0.5 Ma (He et al., 2008). In addition, Zhang et al. (2021) extrapolated an age of the base of chron M0r of 121.2 ± 0.4 Ma. Considering that chron M0r occurred within the *I. giraudi–M. sarasini* Tethyan Ammonite Zone (Frau et al., 2018; Aguado et al., 2022), which base and top are respectively dated at 122.01 ± 0.19 Ma and 121.15 ± 0.31 Ma, our age model fit with the age of chron M0r proposed in He et al. (2008) and Zhang et al. (2021).

The Geologic Time Scale 2020 (GTS 2020) proposes an age of the Berriasian/Valanginian boundary of 137.7 ± 0.5 Ma, an age of the Valanginian/Hauterivian boundary of 132.6 ± 0.6 Ma, an age of the Hauterivian/Barremian boundary of 126.5 ± 0.7 Ma, and an age of the Barremian/Aptian boundary of 121.4 ± 0.6 Ma (Gale et al., 2020). Compared to the GTS 2020, the age model proposed here differs by 0.6 Myr for the Berriasian/Valanginian boundary, 1.3 Myr for the Valanginian/Hauterivian boundary, 0.8 Myr for the Hauterivian/Barremian boundary, and 0.2 Myr for the Barremian/Aptian boundary. The age model of the GTS 2020 is a comprise between cyclostratigraphically-derived durations of stages in the Early Cretaceous (Fiet and Gorin, 2000; Martinez et al., 2013, 2015) and smoothing spline (Agterberg et al., 2020), anchored to the age of the Albian-Cenomanian boundary. Thus, the differences between the age model here and the GTS 2020 arise from the new sequencing of the 405-kyr eccentricity cycle, much consistent with the number of precession cycles recorded and with radiometric data, the use of a more precise correlation to anchor the durations a radiometric age (Aguirre-Urreta et al., 2019), and the consistent use of 405-kyr eccentricity cycles identified from measured data.

8.2. Construction of long climatic series

Spectral analyses were performed on marl-limestone alternations using $CaCO_3$ content, gamma-ray total count and magnetic susceptibility. GRTC and MS data are inversely correlated to $CaCO_3$ content so it is possible to approach the $CaCO_3$ content from these signals and perform spectral analyses on long series covering the Berriasian to the Barremian. The GRTC data were converted into $CaCO_3$ by correlating the GRTC and $CaCO_3$ data from Angles and Río Argos (Fig. 21; Giraud, 1994; Martinez et al., 2012, 2013, 2015). As $CaCO_3$ and GRTC data were sampled during different campaigns, they are not exactly at the same level and a sample collected for $CaCO_3$ can be located stratigraphically in between two GRTC measurements. The equivalent GRTC values at levels sampled for $CaCO_3$ were obtained (i) from linear interpolation of the two surrounding GRTC measurements if they were taken in the same bed, (ii) from the closest GRTC value taken at the same bed as the sample taken for $CaCO_3$ measurement (Tables S1-S2). The MS data from Orpierre were converted into $CaCO_3$ content using the correlation between MS and

$CaCO_3$ data from Vergol-Morénas (Martinez et al., 2020b; Fig. 4A). Note that the calculated $CaCO_3$ content reaches values below 0 % in the latest Berriasian and in the earliest Hauterivian, and values above 100 % in the middle Valaginian. This is because the MS values do not only depend on the $CaCO_3$ but also to the type of iron-bearing mineral species and their proportion in the bulk rock. The values of these intervals are not retained in the spliced curve. The data from Reynier are selected as representative from 137.23 to 134.69 Ma and are retained in the spliced curve because this section is devoid of gravity flow deposit and correspond to a continuous, uninterrupted record of marl-limestone alternations in this interval. The data from Vergol-Morénas are selected as representative from 134.69 to 133.68 Ma as the GRTC values in Vergol-Morénas are similar to Angles and La Charce-Pommerol. The data from Orpierre are selected as representative from 133.68 to 132.26 Ma, as they are less affected by hiatuses than Angles and La Charce (Boulila et al., 2015). The data from La Charce-Pommerol are selected from 132.26 to 127.82 Ma, the data from Río Argos from 127.82 to 126.79 Ma, the data from Arroyo Gilico from 126.79 to 123.97 Ma, and the data from Barranco Cavila from 123.97 to 120.86 Ma (Figs. 1, 22).

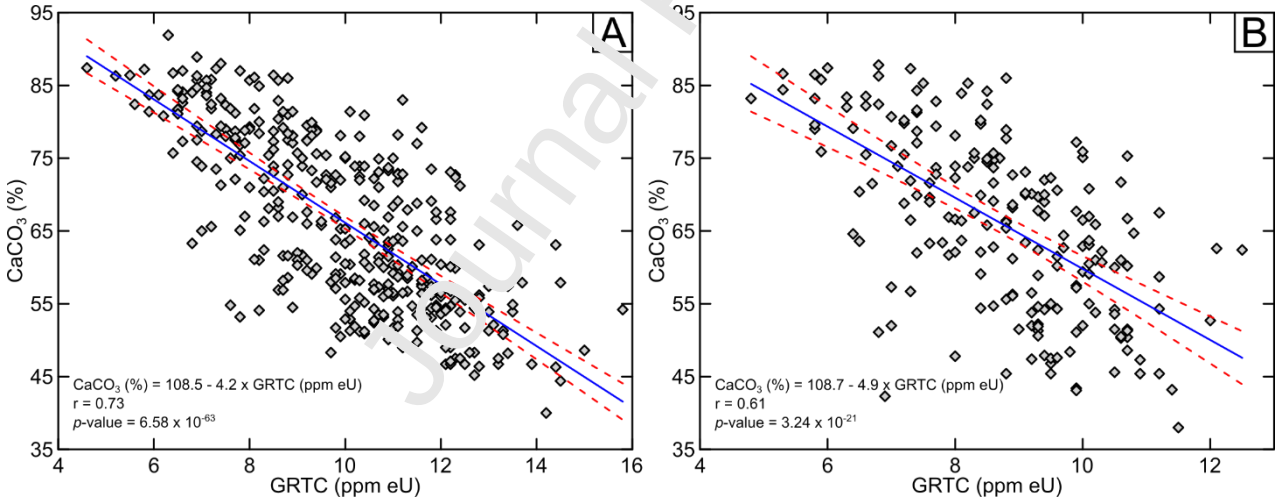

Fig. 21. Cross-plots between the $CaCO_3$ and equivalent GRTC series from (**A.**) the Angles section and (**B.**) the Río Argos section. The solid blue line corresponds to the best-fit linear regression and the dashed red lines to the 95 % confidence intervals.

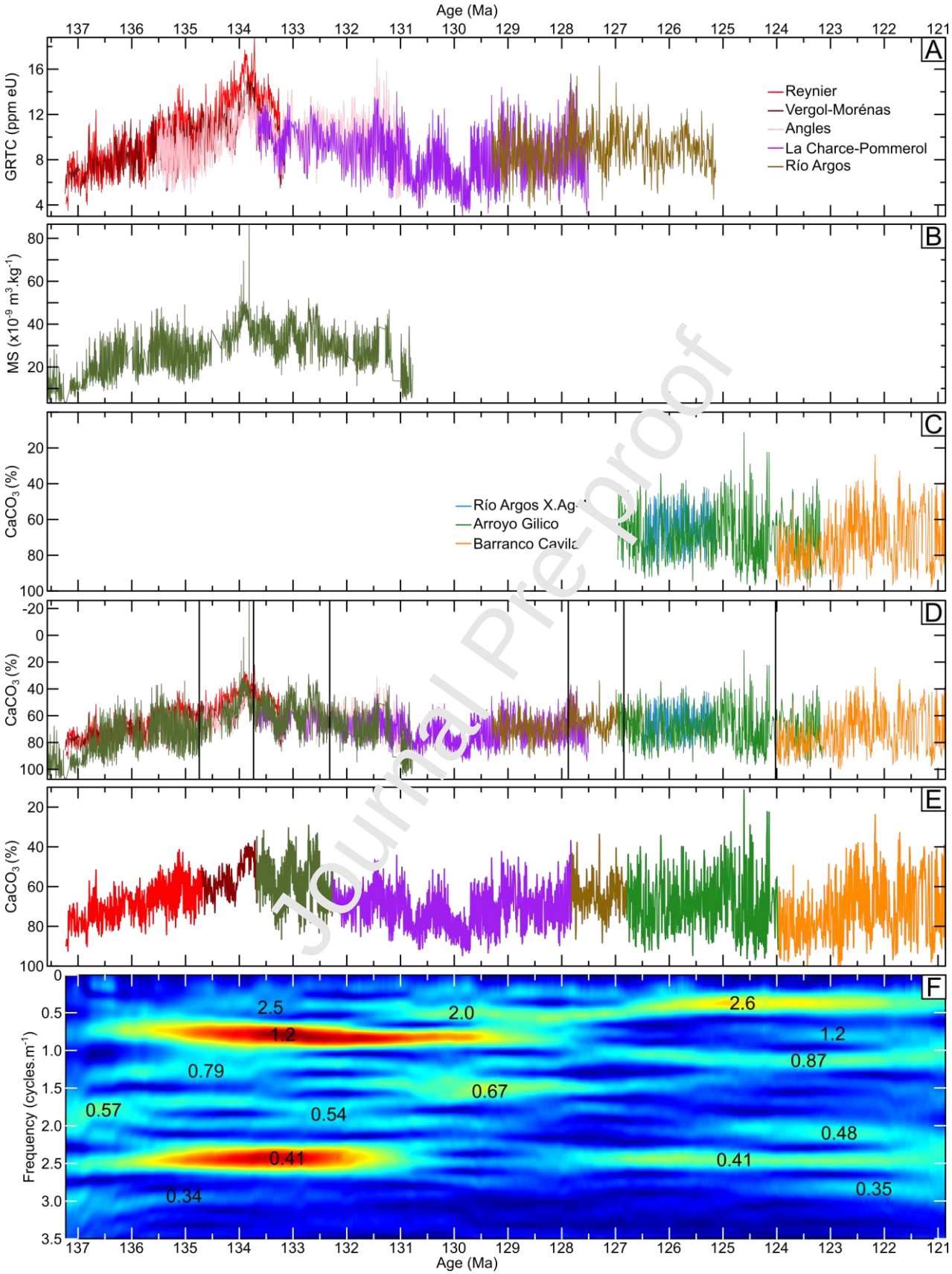

Fig. 22. Construction of the spliced $CaCO_3$ series from the Vocontian Basin and the Subbetic Domain. **A.** GRTC series from Reynier, Vergol-Morénas, Angles, La Charce-Pommerol and Río Argos calibrated into time. **B.** MS series from the Orpierre section. **C.** $CaCO_3$ content series from Río Argos X.Ag-1, Arroyo Gilico and Barranco Cavila calibrated into time. **D.** $CaCO_3$-equivalent series from Reynier, Vergol-Morénas, Angles, La Charce-Pommerol and Río Argos together with $CaCO_3$ series from Río Argos X.Ag-1, Arroyo Gilico and Barranco Cavila calibrated into time. The vertical bars represent where the various series are cut to build the composite series. **E.** Composite $CaCO_3$ series.

The imprint of the long eccentricity cycle on the carbon cycle from the Late Berriasian to the earliest Aptian was tested on compilations of (i) 784 $\delta^{13}C_{bulk}$ data from the Vocontian Basin (Emmanuel and Renard, 1993; Hennig et al., 1999; van de Schootbrugge et al., 2000; Godet et al., 2006; Duchamp-Alphonse et al., 2007; Gréselle et al., 2011; Kujau et al., 2012; Charbonnier et al., 2013; Martinez et al., 2020b; Fig. 23; see Supplements), (ii) 338 $\delta^{13}C_{bel}$ data measured on well-dated belemnite rostra from the Vocontian and the Subbetic basins (van de Schootbrugge et al., 2000; McArthur et al., 2007; Bodin et al., 2009, 2015; Price et al., 2018; Fig. 24; see Supplements) and positioned bed by bed in the sections selected for the spliced $CaCO_3$ series. Only data that could be positioned bed by bed were selected (see correlations available as supplements at: https://zenodo.org/record/5517740). The age of the samples compiled from the latest Berriasian to the earliest Aptian was determined from the astrochronology provided here (Tables 1, 2). The age of the belemnites collected from the *Malbosiceras paramimounum* to the *Tirnovela alpillensis* subzones was calculated proportionally to their position within the ammonite subzone. The durations of the *M. paramimounum* to the *T. alpillensis* subzones is the same as in the Geologic Time Scale 2020 (Gale et al., 2020). The ages of these subzones were anchored to the age of the base of the Valanginian Stage provided here (Table 4). The compilation of stable isotope data on bulk rock together with their age and stratigraphic location is given in supplement. The bulk-rock data from the Subbetic Domain provided here (Fig. 25; see Supplements) were analysed to test the imprint of long orbital cycles in the Barremian Stage of the Subbetic Domain.

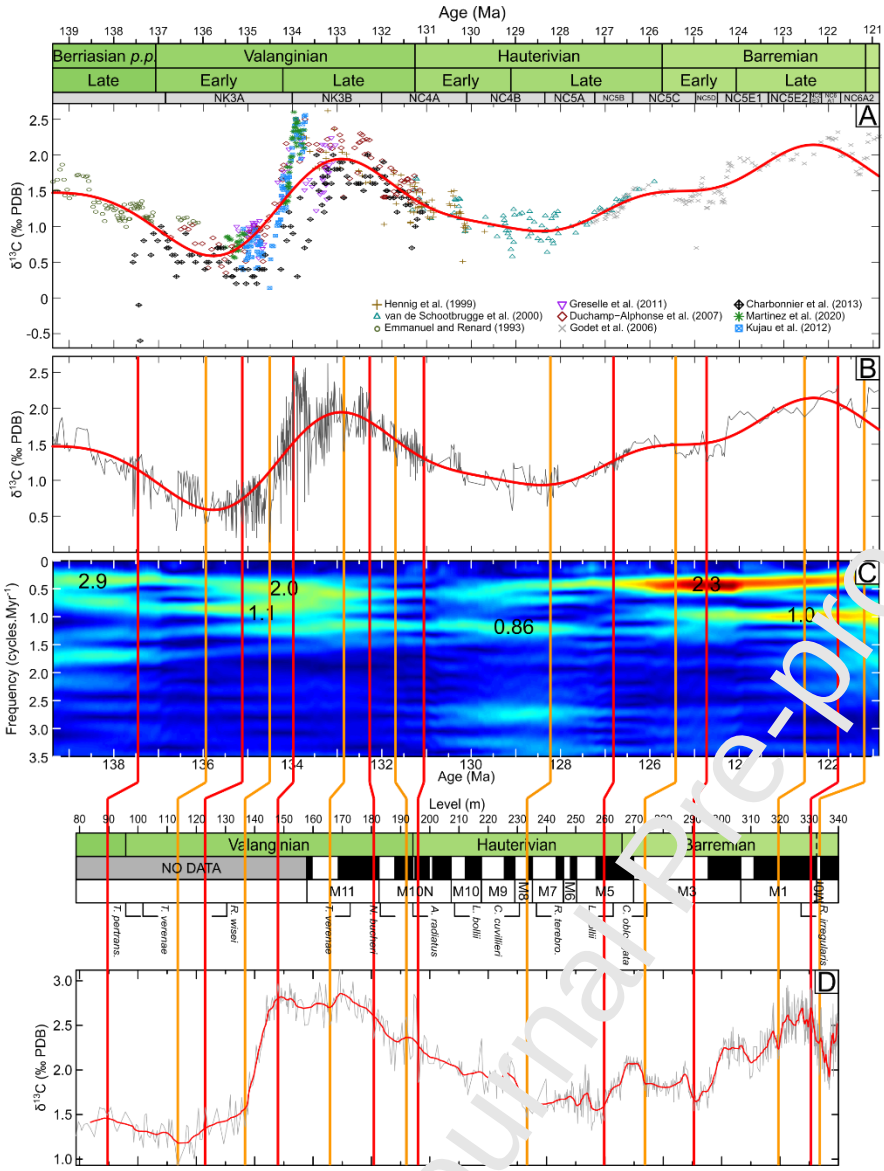

Fig. 23. Evolutive spectral analysis of the $\delta^{13}C_{bulk}$ series from the Vocontian Basin calibrated to time (periods are labeled in Myr) and correlation of this series to the $\delta^{13}C_{bulk}$ from the Maiolica Formation (Umbria-Marche; Sprovieri et al., 2006).

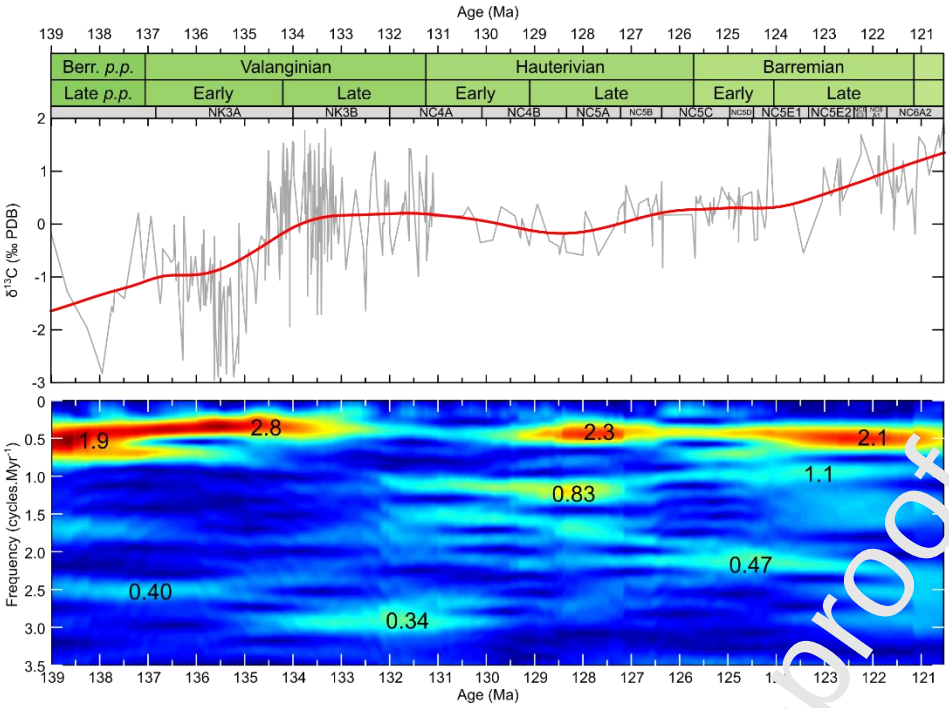

Fig. 24. Evolutive spectral analysis of the $\delta^{13}C_{bel}$ series from western Tethys calibrated to time. Periods are labeled in Myr.

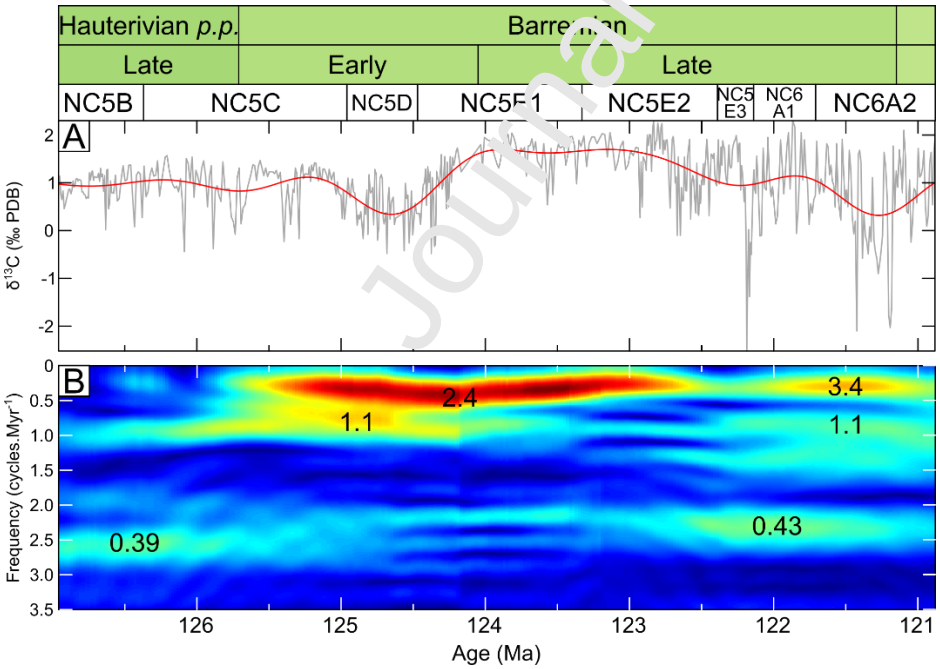

Fig. 25. Evolutive spectral analysis of the $\delta^{13}C_{bulk}$ series from the Subbetic Domain calibrated to time. Periods are labeled in Myr.

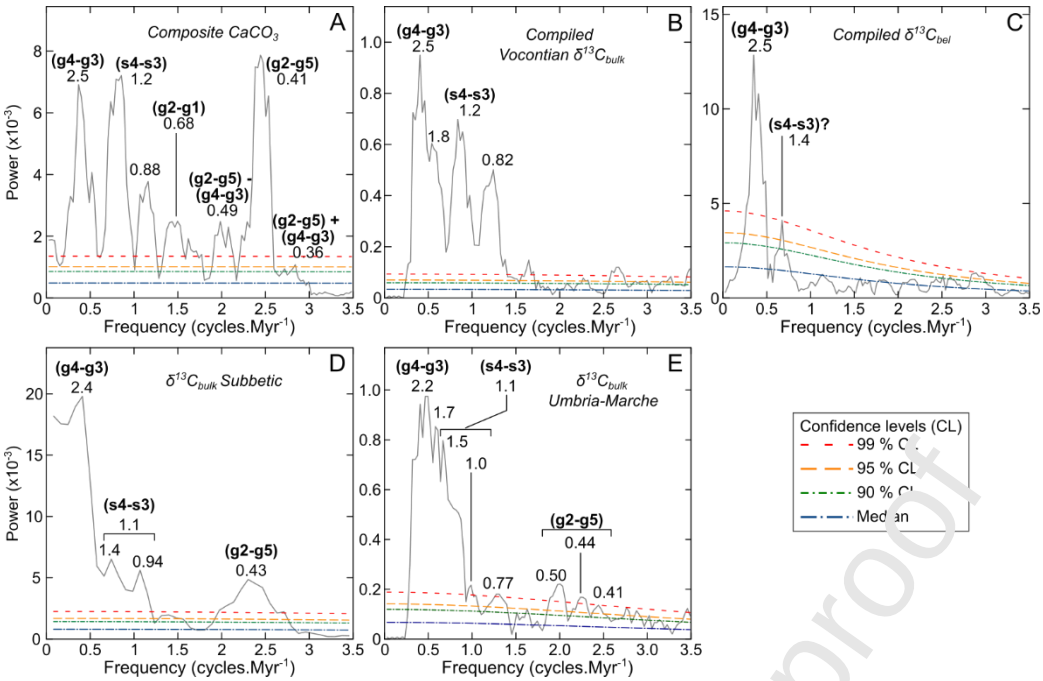

Fig. 26. 2π-Multi-Taper (MTM) spectra (**A.**) the composite $CaCO_3$ series, (**B.**) the compiled $\delta^{13}C_{bulk}$ series from the Vocontian Basin, (**C.**) the compiled $\delta^{13}C_{bel}$ series (**D.**) the $\delta^{13}C_{bulk}$ series from the Subbetic Domain, (**E.**) the $\delta^{13}C_{bulk}$ series from the Umbria-Marche Basin. The periods are labeled in Myr.

8.3. Correlation with magnetochrons

The age model provided here is from sections well dated by biostratigraphy and chemostratigraphy. However, no magnetostratigraphy is available on these sections, likely because of post-deposition remagnetization (Hoedemaeker et al., 1998; Katz et al., 2000). The magnetostratigraphic framework from the Valanginian to the Barremian is available from the Umbria-Marche Basin (Central Italy; Channell et al., 1995, 2000), anchored to calcareous nannofossil and ammonite biostratigraphy and carbon-isotope stratigraphy (Sprovieri et al., 2006). A correlation scheme is proposed here between the carbon-isotope curve from the Vocontian Basin and from the Umbria-Marche Basin (Fig. 23; Table 5). This is based on (i) the Weissert carbon-isotope excursion in the Late Valanginian, (ii) the minimum in $\delta^{13}C$ values in the Early Valanginian, (iii) the minimum in the $\delta^{13}C$ values in the Late Hauterivian, (iv) the positive excursions related to the Faraoni, Mid-Barremian and Taxy events. The proposed ages of the magnetochrons is provided in Table 6. The difference in the age of the bioevents with the Vocontian and Subbetic domains is

provided in Table 7. The ages can show an excellent correspondence for the ages of the FO of ammonites *"T." pertransiens* and *A. radiatus*, the FO of calcareous nannofossil *T. verenae*, *L. bollii* and *R. irregularis*. It can however reach a difference of 0.8 Myr in the LO of calcareous nannofossils *R. wisei* and *R. terebrodentarius*. Aguado et al. (2018) demonstrated that the LO of *R. wisei* is not recorded at the same interval of the Weissert positive carbon-isotope excursion. The difference in age of 0.8 Myr recorded between the Vocontian, Subbetic and Umbria-Marche basins is possibly due to the uncertainty in the stratigraphic location of their first and last occurrences. The top of magnetochron M1r is dated at 123.17 ± 0.19 Ma in our age model from the Umbria-Marche Basin, while Zhang et al. (2021) proposed 123.1 ± 0.3 Ma for the upper part of this chron. Still in our age model from the Umbria-Marche Basin, magnetochron M0r is dated from 121.40 to 121.13 ± 0.19 Ma (Table 7). This is consistent with the age of 121.2 ± 0.5 Ma proposed with Ar-Ar ages by He et al. (2008). Chron M0r occurred within the interval *I. giraudi–M. sarasini* Tethyan ammonite zones (Frau et al., 2018; Aguado et al., 2022), so the age of the start of chron M0r should be in between 122.01 and 121.15 Ma. So the maximum uncertainty of the age of chron M0r calculated here is 0.6 Myr. In summary, our age model is consistent with the numerical ages produced for magnetochrons.

9. Impact of the long orbital cycles on climate and sedimentary series

9.1. Spectral analyes of long climatic series

The spectrum of the composite $CaCO_3$ series indicates prominent cycles at periods of 2.5 Myr related to the eccentricity (g4-g3) cycle (Laskar et al., 2011), at 1.2 Myr related to the long obliquity (s4-s3) cycle (Laskar et al., 2011), and at 0.88 My, 0.68 Myr, 0.49 Myr, 0.41 Myr, 0.36 Myr (Fig. 23A). The three last peaks correspond to the 405-kyr eccentricity (g2-g5) periods and their modulator linked to the 2.4-Myr cycle (Laskar et al., 2011). On the amplitude spectrogram, the 2.5-Myr cycle is expressed through the entire interval studied (Fig. 22F). The 1.2-Myr cycle is observed through the entire interval, except from 127 to 125 Ma. The 0.68-Myr cycle is only observed from 132 to 128 Ma, and is probably too local to bear any astronomical information, despite close affinity to the g2-g1 period in the astronomical solutions

(Laskar et al., 2011). The period of ~0.8 Myr is observed through the entire series. This period could be related to an amplitude modulation of the obliquity cycle related to s4-s3+g4-g3 (Hinnov, 2000) or to the 0.97-Myr eccentricity cycle g1-g5 (Laskar et al., 2011).

The spectrum of the $\delta^{13}C_{bulk}$ compiled from the Vocontian Basin shows outstanding periods at 2.5 Myr, 1.2 Myr and 0.82 Myr (Fig. 23B). As in the $CaCO_3$ series, the 2.5-Myr period is related to the (g4-g3) eccentricity period, and the 1.2-Myr period to the (s4-s3) obliquity period. A period of 0.82 Myr is also observed. On the amplitude spectrogram, the 2.5-Myr cycle is expressed through the studied interval, with a gap in the Early Hauterivian, likely because of the occurrence of the two slumps at La Charce. In the interval equivalent at Pommerol, no bulk carbon-isotope value is available (Fig. 24C).

The spectrum of the $\delta^{13}C_{bel}$ series shows a prominent cycle with a period of 2.5 Myr (Fig. 23C). Another period at 1.4 Myr is also observed. On the amplitude spectrogram (Fig. 25B), the 2.5-Myr period is observed throughout the whole interval with periods ranging from 1.9 to 2.8 Myr related to (g4-g3) eccentricity. Periods around 0.4 Myr in the Berriasian, Valanginien and Early Barremian related to (g2-g5) eccentricity. A period at 1.1 Myr is observed in the Late Barremian and a period at 0.83 Myr is observed in the Late Hauterivian.

The spectrum of the $\delta^{13}C_{bulk}$ series from the Late Hauterivian-Barremian of the Subbetic Domain shows prominent cycles at 2.5 Myr related to (g4-g3) eccentricity, 1.1 Myr on average related to (s4-s3) obliquity and 0.43 Myr related to (g2-g5) eccentricity (Fig. 23D). The amplitude spectrogram shows a period at 2.4 Myr related to the eccentricity cycle (g4-g3) expressed in the Early and lower part of the Late Barremian (Fig. 26B). This period increases to 3.4 Myr in the last part of the Late Barremian, in response of the high-amplitude negative excursions related to the Taxy Event. Another period is observed at 1.1 Myr throughout the Late Hauterivian and Barremian, related to the obliquity (s4-s3). Finally, a period at 0.4 Myr is observed throughout the Late Hauterivian and Barremian, related to the eccentricity (g4-g3).

The spectrum of the $\delta^{13}C_{bulk}$ series from the Maiolica Formation of the Umbria-Marche Basin shows a prominent cycle at 2.2 Myr related to (g4-g3) eccentricity, peaks at 1.5 to 0.99 Myr that we attribute to (s4-s3) obliquity and peaks around 0.41 Myr related to (g2-g5) eccentricity (Fig. 23E). The amplitude

spectrogram shows the period of 2.5 Myr throughout the series with periods ranging from 2.0 to 2.6 Myr (Fig. 27B). The group of periods attributed to (s4-s3) obliquity is expressed throughout the series as well with periods ranging from 1.0 to 1.4 Myr. Finally, the group of periods attributed to the (g2-g5) eccentricity cycle is only expressed from the base of the interval studied to the top of the Valanginian.

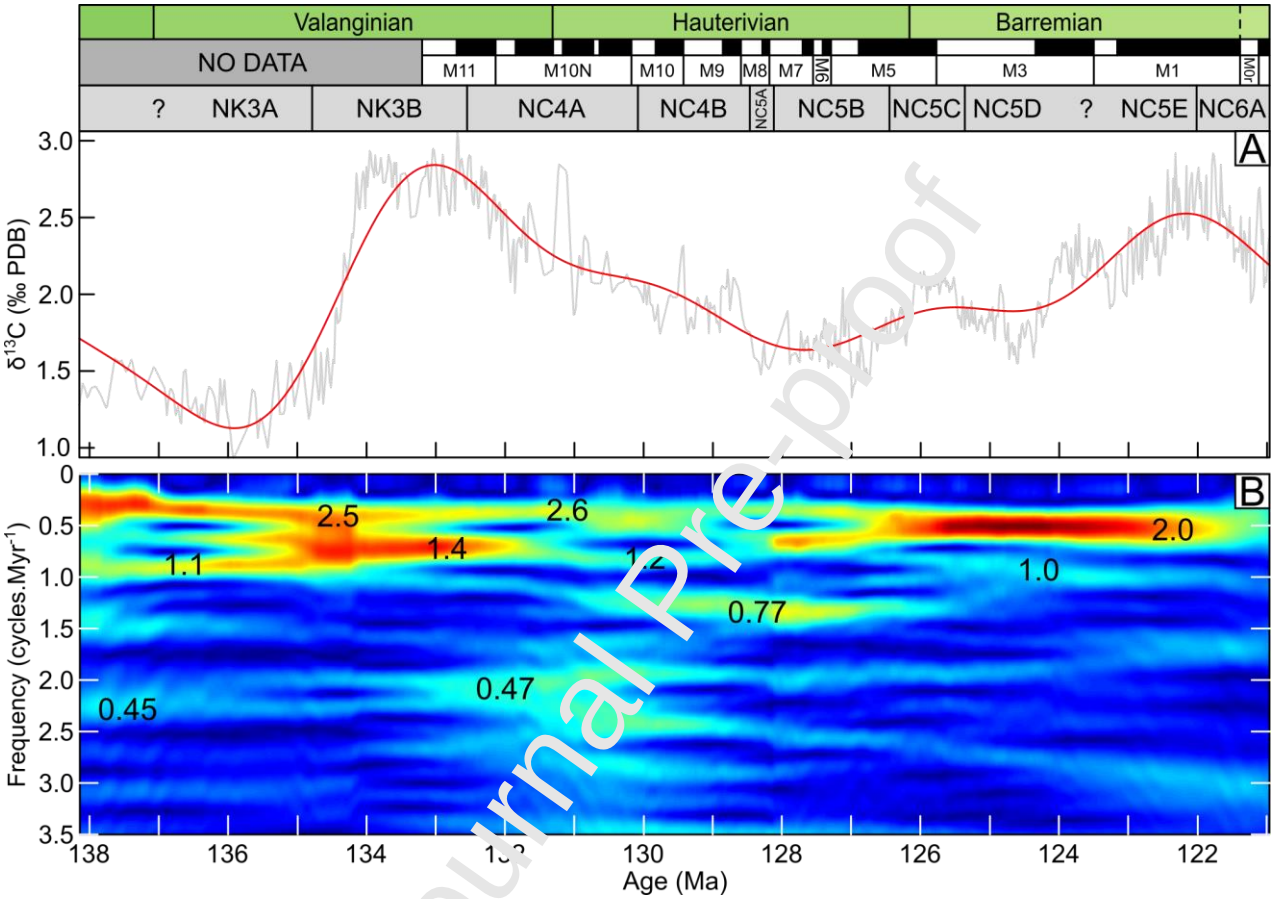

Fig. 27. Evolutive spectral analysis of the $\delta^{13}C_{bulk}$ series from the Umbria-Marche calibrated to time. Periods are labeled in Myr.

9.2. Impact of the long orbital cycles on lithology and carbon isotope ratios

The presence of persistent cycles with 2.5-Myr and 1.2-Myr periods in the composite $CaCO_3$ and $\delta^{13}C$ series demonstrates the role and the outstanding pacing of these long orbital cycles on the lithology and carbon-isotope ratios, at least in the Western Tethys, from the Berriasian to the Barremian stages. From the latest Berriasian to the middle part of the Hauterivian, the filter of 2.4 and 1.2-Myr cycles in the composite

$CaCO_3$ are in opposite phase with their counterpart in the carbon-isotope ratios (Fig. 1). This implies that increased detrital fraction in the sediment in the Vocontian Basin corresponded to periods of increased values of $\delta^{13}C$ both in bulk rock and belemnites. This is consistent with observations in the field (Fig. 5). Analyses of clay mineralogy (Duchamp-Alphonse et al., 2011; Morales et al., 2013; Charbonnier et al., 2016; Martinez et al., 2020b), calcareous nannofossil assemblages (Gréselle et al., 2011; Duchamp-Alphonse et al., 2014; Mattioli et al., 2014) and platform-basin correlations (Gréselle and Pittet, 2010; Morales et al., 2013) point that these periods correspond to increased weathering of continent, increased fertilization of the water masses due to increased nutrient supply and increased sea level. In other words, the $\delta^{13}C$ reaches maximum values when the detrital supply is also maximal, while the neritic carbonate production was minimal. This demonstrates that the long orbital cycles triggered repetitive phases of humid peaks, leading to increase in weathering, detrital supply, fertilization of marine environments, decline in neritic carbonate productivity and increased burial of organic carbon in marine and/or continental environments throughout the Berriasian-Aptian times. The scenario is also consistent with earlier suggestions (Föllmi, 1995; Bodin et al. 2006b) of a positive link in between global oceanic nutrient levels (as deduced from phosphorus accumulation rate) and sea-level fluctuations, given that maximum flooding intervals are characterized by increased clay carbonate ratio in the Lower Cretaceous of the western Tethyan realm (e.g., Godet et al., 2013). From that perspective, the early Valanginian, latest Valanginian and mid-Hauterivian humid events show the same charateristics as the Episodes of Environmental Changes (EECs) described in Föllmi (2012) and can be regarded as such. The humid peak of the Early Valanginian is bounded in the interval of increase in GRTC values at Vergol in between beds B150 and V28 (levels 11.55 m to 27.35 m), at Reynier in between beds R34 and R69 (levels 10.80 m to 28.10 m) and at Orpierre in between 13.97 m and 31.46 m (Figs. 9, 13). This interval is in the middle of the *"T." pertransiens* Tethyan ammonite zone and corresponds to very humid interval in Morales et al. (2013) on the basis of clay mineral and palynologic assemblages. The latest Valanginian event is located at La Charce from bed LCP179 to 183 (levels 74.52 m to 79.55 m, Figs. 10, 15) and at Angles from bed A372 to 376 (levels 203.83 to 210.38 m), at the transition between the *C. furcillata* and *T. callidiscus* Tethyan ammonite

subzones. This interval shows a maximum in humid conditions determined from kaolinite and palynological assemblages (Kujau et al., 2013; Charbonnier et al., 2016). The mid-Hauterivian event corresponds to the increase in GRTC values observed at La Charce from bed LCP 273 to 295 (levels 177.50 to 193.65 m; Figs. 11, 17) around the Marl Interval of Sayni (Fig. 6A). The age of these events in given in Table 8. It shows that these events are separated by an average duration of 2.46 Myr, in line with the cycle observed in the composite $CaCO_3$ and $\delta^{13}C$ series. This demonstrates the outstanding pacing of the 2.4-Myr eccentricity cycle on the recurrence of the EECs in the Early Cretaceous.

From the uppermost Hauterivian to the Barremian, the filters of 2.5 and 1.2-Myr cycles in the composite $CaCO_3$ content turn in phase with their counterpart in the $\delta^{13}C_{bulk}$ series (Fig. 11). In this case, the EECs correspond to periods of increased carbonate content in the Subbetic Domain. This feature has already been noticed in Martinez et al. (2020a) and is associated with decreased sedimentation rate at times of higher sea level, which point to starvation of detrital sediment. Clay mineral and calcareous nannofossil assemblages still indicate that these periods of EECs correspond to increased levels of humidity on continents and fertilization of the water masses, in line with the phasing between EECs and environmental conditions observed during the Valanginian and the Hauterivian stages. This change of phasing between lithology and carbon cycle is an example of the local/regional response of sedimentary systems to a global forcing.

The climatic disturbances associated with the Taxy Event started in the *I. giraudi* Tethyan ammonite zone (Frau et al., 2020; Martinez et al., 2020a). Nonetheless, the fertilization event of water masses occurred during the negative carbon-isotope excursion (Aguado et al., 2022). This negative excursion is interpreted as an increase in influx of dissolved inorganic carbon through increase in oxidation of marine organic matter and/or increase in supply of oxidized terrestrial organic matter (Stein et al., 2012). So the phasing between climate and carbon isotope can also change depending on the source of carbon. It should also be noted that the EECs described have been defined in the peri-Tethys, Northern Atlantic and Northern European areas, all lying in the same climatic belt, from humid subtropical to tropical savannah (Charbonnier et al., 2020; Burgener et al., 2023). The humid phases described here may hence vary in time and space depending on the motions of the climatic belts, themselves orbitally-controlled at Milankovitch

time scales (Armstrong et al., 2016).

It is also noteworthy that from the Hauterivian to the Barremian, the filters of the 2.5-Myr in the $\delta^{13}C_{bel}$ is in opposite phase with their counterparts in the $\delta^{13}C_{bulk}$ (Fig. 1). The reason for this is unclear. It could relate to a lower density of sampling in Hauterivian and Barremian stages, less studied than the Valanginian Stage, which contains the onset of the Weissert Event. It could be also linked to the high variaibility of the $\delta^{13}C_{bel}$ values within a specific level caused by the fact belemnites were nektonic dwellers and they could change depth and cross long distances during their life.

9.3. Orbital configuration at the inception of the Episodes of Environmental Changes

The analysis of the amplitude modulation of the precession cycles shows minimum amplitudes during the Weissert, the Faraoni, Mid-Barremian and Taxy episodes (Figs. 15, 17, 19). The precession cycles show high amplitudes during the Early Valanginian and Mid-Hauterivian events, and variable amplitudes depending on the section in the latest Valanginian event (Fig. 15). High amplitudes of precession during the humid peaks of the Early Valanginian and mid-Hauterivian imply that these events occurred at high eccentricity times leading to high variability in the precession cycles. This context triggers alternate periods of minimum seasonality to extremely high seasonality. In this context, high seasonality favour, for instance, the intensity of the monsoon cycle which can lead to increae in rainfall, weathering of continents and surface of humid areas on continents (e.g., Lézine et al., 2014).

Minimum amplitudes could be explained in the Weissert by the disappearance of carbonate beds, so that the lithology shows less variaibility. In this case, this is not sure whether the low amplitudes observed during the humid peak of the Weissert Episode are related to actual decrease in the eccentricity of the Earth orbit or simply a regional response to a climatic forcing. However, minimum in amplitude of the precession and short eccentricity cycles have been well documented during the Faraoni Event (Martinez et al., 2015). In the Subbetic Domain, increase in clay content generally implies more humid climate (Moiroud et al., 2012). This is not the case during the Faraoni which appears singular from the rest of the analysed series from that point of view (Fig. 5), possibly due to starvation of detrital sediment in a context of 2nd-order

maximum flooding (Martinez et al., 2020a). Such feature occurred in the Mid-Barremian and Taxy events which show some similarities with the Faraoni Event. It is thus intriguing to observe that these three events occurred at time of low amplitude of precession, which implied a long period of moderate seasonality. Martinez and Dera (2015) suggest that this context is favourable to the development of annually humid climate leading to increase in nutrient supply and fertilization of the sea-water masses. Recent investigation of charcoal abundance, elemental composition from XRF and clay mineral analyses in the Early Jurassic appear to corroborate this hypothesis (Hollaar et al., 2022). Variable phasing between the onset of EECs and amplitude of precession cycles needs further investigation from a proxy independent from lithology and more directly linked humid-arid cycles (e.g. Hollaar et al., 2022). Climate simulations performed in the context of the Eocene-Oligocene transition demonstrate that the response of the biota to a given orbital configuration can be heterogeneous in space and time (Tardif et al., 2021). Thus, it is also possible that no simple linear mechanism exists between the onset of the EECs and the change in the orbital configuration and that this relationship may vary through time.

9.4. An orbitally-controlled glacio-eustatism in the Early Cretaceous?

The EECs and related humid peaks are associated with widespread marl deposits and important maximum flooding surfaces in neritic environments (Reboulet et al., 2003; Godet et al., 2013; Morales et al., 2013), as well as faunal exchanges between Tethyan and Boreal realms (Walter, 1996; Mutterlose and Bornemann, 2000), reflecting major sea-level rise events (Matthews and Frohlich, 2002; Frau et al., 2020; Morales et al., 2016). In the Helvetic Platform, three drowning unconformity surfaces (Gemsmättli, Lidernen and Altmann) are associated with the Weissert, Mid-Hauterivian and Faraoni events, respectively (Bodin et al., 2006a; Godet, 2013; Morales et al., 2016). These unconformities reflect rapid sea-level changes (falls and rises) and eutrophication, following increased detrital and nutrient input to the basin (van de Schootbrugge et al, 2003; Bodin et al., 2006b).

Aquifer-eustasy has been proposed to explain these rapid sea-level variations in a supposed equally warm Cretaceous. In this model, sea level decreases because of ground-water storage during the humid phases

(Föllmi, 2012). Here, the opposite is inferred, indicating that aquifer-eustasy cannot explain these Early Cretaceous sea-level variations, as already suggested by Davies et al. (2020). Recent TEX 86 analyses performed on Valanginian (Cavalheiro et al., 2021) and Barremian rocks (Huck and Heimhofer, 2021) suggest that the mid-Valanginian, the mid-Barremian and the Taxy events all corresponded to warming phases. Evidence for glacial sedimentation at high-paleolatitude in Southern Hemisphere supports the idea of persistent polar ice caps during the Late Valanginian (Alley et al., 2020), in line with evidence for a cooling event in the Late Valanginian (McArthur et al., 2007; Price and Passey, 2013; Bodin et al., 2015; Cavalheiro et al., 2021) and frequency of glendonites at high latitudes (Price, 1999).

Interestingly, the end of the Early Valanginian (*K. inostranzewi* Tethyan ammonite Zone, cycle V6; Fig. 15) corresponds to an important regression event preceding an important transgression during the *S. verrucosum* Zone. All these events have several dozens of meters of amplitude (Davies et al., 2020). In the upper Valanginian, the cold interval from the *Olcostephanus (Olcostephanus) nicklesi* to the *Criosarasinella furcillata* Tethyan ammonite subzones (cycles V10-V12; Fig. 15) also corresponds to an important regressive event preceding the transgression at the end of the Valanginian (Ferry, 1987). These cold and regressive events precede the Weissert and the latest Valanginian Event. Their asymmetric nature (Gréselle and Pittet, 2010), amplitude, the fact that they are recognized at large geographic scale and the fact that glacial features have been identified in Australia from the Valanginian to the Albian (Alley et al., 2020) point that these time intervals corresponded to transient polar ice cap development phases. In the mid-Hauterivian, from the *L. nodosoplicatum* to the *S. sayni* Tethyan ammonite zones, the trend in the GRTC values shows a long-tern decrease followed by two steps of rapid increase separated from each other by 0.5 Myr (Fig. 17). Assuming the formation are increasingly carbonated when the sea level decrease, this trend implies a long-term sea level decrease in the Early Hauterivian followed by rapid increase at the beginning of the Late Hauterivian. In the Helvetic Platform, this time interval is represented by the Liedernen drowning unconformity, marked by an important regression followed by important transgressive events (Godet, 2013). As in the middle and Late Valanginian, an important regression event occurred before the rapid transgression, pointing again to glacio-eustatism. The second minimum in GRTC value at

the end of the Early Hauterivian coincides in the Neuquén Basin with a shift from basinal environment to aeolian dunes and fluvial systems. This change could be the local expression of a widespread-identified regression event (Sahagian et al., 1996; Mutterlose and Bornemann, 2000; Pictet, 2021). In the Barremian Stage, Frau et al. (2020) noticed high-amplitude sea level falls around the Baremian-Aptian transition and evoked glacio-eustatism as the most likely mechanism of sea level decrease on the basis of paleotemperature reconstructions (O'Brien et al., 2017), and numerical modeling of climate (Donnadieu et al, 2006; Ladant and Donnadieu, 2016; Pohl et al., 2019).

10. Synchronism between the Paraná-Etendeka LIP and the Weissert Event

The base of the Weissert Event is defined by a worldwide increase in the bulk-rock and organic $\delta^{13}C$ values during the late Early Valanginian (Fig. 2). Detailed bulk-rock stable isotope data accurately position the Weissert Event in the Vergol-Morénas and La Charce-Pommerol series (Hennig et al., 1999; Gréselle et al., 2011; Kujau et al., 2012; Martinez et al., 2020b). From the time scale revised here, the onset of the Weissert carbon isotope excursion is dated at 134.50 ± 0.19 Ma. This new age refines and replaces the previous dating at 135.22 ± 1.00 Ma (Martinez et al., 2015). The end of the rising phase of the carbon-isotope excursion is dated at 133.96 ± 0.19 Ma, and the end of the plateau phase is dated at 132.44 ± 0.19 Ma.

Thiede and Vasconcelos (2010) and Janasi et al. (2011) proposed ages of Paraná continental flood basalt of 134.7 ± 1 Ma, and 134.3 ± 0.8 Ma, from ^{40}Ar-^{39}Ar and U-Pb ID-TIMS analyses, respectively. These ages suggest rapid extrusion of the continental flood basalt, and synchronous to the start of the mid-Valanginian carbon-isotope excursion. However, CA-ID-TIMS U-Pb ages recently provided ages of 133.6 ± 0.12 Ma (Rocha et al., 2020), which lies within the plateau phase of the carbon-isotope excursion. A further compilation and critical review of Ar-Ar and U-Pb ages nonetheless suggests that the activity of main phase of the Paraná-Etendeka Large Igneous Province (LIP) started 135.0 ± 0.6 Ma and ended 133.2 ± 0.2 Ma, with a peak of activity dated at 134.4 ± 0.1 Ma, and eruptions possibly ceasing 132.0 ± 0.2 Ma (Fig. 1) (Gomes and Vasconcelos, 2021). This compilation agrees with recent ^{40}Ar-^{39}Ar ages performed throughout

a vertical stratigrahic profile of the Paraná province and indicating ages from *ca.* 135.5 to *ca.* 133.5 Ma (Bacha et al., 2022). This in line with significant enrichment in mercury measured at the base of the positive carbon-isotope excursion (Charbonnier et al., 2017; Vickers et al., 2023). This synchronicity reinforces the hypothesis of a probable link between the onset of the Weissert Event and the peak of activity of the Paraná-Etendeka province.

Paleomagnetic data suggest the activity of the Etendeka province likely covered 16 magnetochrons suggesting long-lived activity of the Etendeka province (Dodd et al., 2015). Conversely, Mena et al. (2011) shown that the Paraná province covered three to five magnetochrons, starting with normal polarity. Paleomagnetic and carbon-isotope data from the Umbria-Marche Basin show that the Weissert carbon-isotope excursion started within magnetochron M12n (Weissert and Erba, 2004), in line with paleomagnetic data from the Paraná province. If this correlation is correct, this suggest that the majority of the Paraná continental flood basalt were deposited from chrons M12n to M11An.1n, in line with a short-lived activity of the magmatic province (Gomes and Vasconcelos, 2021). If the ages of Rocha et al. (2020) appeared to be the most likely, the correlations between the Paraná province and the magnetochron would shift to the interval from M11An.1n to M11n, still supporting short-lived activity of the province.

The Comei-Bunbury province is another magmatic province active during the Late Valanginian (Zhu et al., 2009; Harry et al., 2020). Unfortunately, the Naturaliste magmatic Plateau (SW Australia), belonging to the Comei-Bunbury province, has not been drilled down the base of the magmatic series. The eldest magnetochron recorded is M11r (Harry et al., 2020), leaving the possibility of the Naturaliste Plateau to be synchronous of the Weissert carbon-isotope excursion. SHRIMP and LA-ICP-MS U-Pb ages performed on the Comei Basalts indicate the activity of the province occurred 131.5 ± 0.8 Ma, which seems to postdate the carbon-isotope excursion (Zhu et al., 2009). The extension of the volcanic centers of the Comei-Bunbury province reaches ~0.13 x 10^6 km^2 (Zhu et al., 2009; Olierook et al., 2017), which is much smaller than the Paraná-Etendeka province (~1 x 10^6 km^2; Frank et al., 2009). The estimated total volume of magma extruded from the Paraná-Etendeka province is comprised between 2 and 3 x 10^6 km^3, with an estimated average effusion rate of 0.9 to 1.7 km^3/yr, in line with other LIPs associated with global

environmental crises (Gomes and Vasconcelos, 2021).

It is however noteworthy that the humid peak related to the Weissert Event still follows the pacing of the 2.4-Myr eccentricity cycle, which demonstrates that the emplacement of the Paraná-Etendeka volcanic province did not modify the pacing of the EECs caused by the long orbital cycles. However, the carbon-isotope excursion which defines the Weissert Event started 0.6 Myr before the humid peak, while the other EECs of the Valanginian-Barremian are all shorter than 0.5 Myr. The long-term trend $CaCO_3$ curve shows minimum values during the Weissert Event (Fig. 1), in line with the neritic carbonate production crisis inferred at this time (Föllmi et al., 2006; Föllmi, 2012). The humid peak related to the Weissert Event also corresponds to a global warming phase, maximum in kaolinite content and eutrophication of the marine environments in the Valanginian series (Duchamp-Alphonse et al., 2014; Charbonnier et al., 2020). Finally, the Late Valanginian cold interval (Bodin et al., 2015; Cavalheiro et al., 2021) has likely lasted more than 1 Myr while the other cold intervals suspected in the Valanginian-Hauterivian have not lasted more than 0.5 Myr. The Weissert Event thus appears as a singularly long event compared to other EECs which had profound impact on climate and marine ecosystems. The release of greenhouse gases during the emplacement of the Paraná-Etendeka may therefore have caused increase in temperature, humid conditions, detrital and nutrient supply to basins, favoring eutrophication of marine environments and crisis in the neritic carbonate productivity. Storage of organic carbon on continents and high latitude marine environments (Westermann et al., 2013; Charbonnier et al., 2020; Cavalheiro et al., 2021; Vickers et al., 2023) may have favored the onset of a long-lasting cold snap in the Late Valanginian by drawdown of atmospheric CO_2. It is thus noteworthy that the onset of the Paraná-Etendeka LIP did not modify the pacing of the carbon and detrital cycles caused by the long orbital cycles. However, it amplified and lengthened the climatic changes provoked by the long eccentricity cycles, triggered a long-lasting carbon isotope excursion in bulk carbonate and a long-lasting cooling event leading to developments of ice caps during the Late Valanginian.

11. Conclusions

Our revised time scale demonstrates that the long orbital cycles paced the occurrence of EECs, through cyclic fluctuations of global precipitation, and likely through glacio-eustatically induced sea levels changes. The concomitant increase in orbitally forced humidity and sea level triggered conditions to increase the burial of organic matter in continental and marine environments. During the late Early Valanginian, the middle Late Valanginian and the end of the Early Hauterivian, high-amplitude sea-level falls, cooling events and subsequent rapid sea-level increases may point to glacial maximum conditions separated by ~2.5 Myr on average. Our time scale clearly demonstrates the synchronicity between the onset of the Weissert Event and the peak of activity of the Paraná-Etendeka large igneous province. Nevertheless, the Weissert Event peak in detrital supply and $\delta^{13}C$ maxima keep following the pacing of the 2.4-Myr eccentricity cycle. The Weissert Event appears thus as a singularly long event with stronger impact on climate and marine ecosystems than other Episodes of Environment Changes defined in Föllmi (2012), which was the consequence of the concomitant effect of the emplacement of the Paraná-Etendeka province and long orbital cycles.

Acknowledgments:

We acknowledge MITI AAP Temps AstroCarb, CONICET, UBA, UNRN, ANPCyT, projects CGL2014-52546-P (Ministerio de Ciencia, Innovación y Universidades, Spain) and P20_00783 (Junta de Andalucía, Spain) for their support in this study. IMM designed the experiment, performed the astrochronology and wrote the manuscript. BAU, ML, JC and MT collected samples and established the stratigraphy in the Neuquén Basin. LO, RA and MC collected samples, established the stratigraphy and provided the bulk-rock stable isotope data from the Subbetic Domain. GD helped in the interpretation of the stable isotope data on belemnites and contributed to the manuscript. SB contributed in linking the climatic to eustatic changes and to the manuscript. This is a contribution R-342 of the Instituto de Estudios Andinos “Don Pablo Groeber” and to RNM-200 and 373 Research Groups (Junta de Andalucía, Spain). A detailed vectorized figure is provided at the following link to show the correlations and the positions of the samples within the sections: https://zenodo.org/record/5517740. We thank Jim Ogg, Stephen Hesselbo, Andy Gale

and an anonymous reviewer for their helpful comments and the editor Christopher Fielding for handling the manuscript. We thank Mario Sprovieri for providing the bulk carbonate $\delta^{13}C$ data from the Umbria-Marche Basin.

References

Agterberg, F.P., Da Silva, A.-C., Gradstein, F.M., 2020. Geomathematical and Statistical Procedures, in: F.M. Gradstein, J.G. Ogg, M.D. Schmitz, G.M. Ogg (Eds.), Geologic Time Scale 2020, vol. 2, chap. 14, Elsevier B.V., Amsterdam, The Netherlands, pp. 402–438. https://doi.org/10.1016/B978-0-12-824360-2.00014-0.

Aguado, R., Company, M., Castro, J.M., de Gea, G. A., Molina, J.M., Nieto, L.M., Ruiz-Ortiz, P.A., 2018. A new record of the Weissert episode from the Valanginian succession of Cehegín (Subbetic, SE Spain): Bio-and carbon isotope stratigraphy. Cretaceous Research 92, 122–137. https://doi.org/10.1016/j.cretres.2018.07.010.

Aguado, R., Company, M., O'Dogherty, L., Sandoval, J., Martinez, M., 2022. New insights into the Barremian–lower Aptian calcareous nannofossils of the Mediterranean Tethys: Chronostratigraphic and paleobiogeographic implications. Marine Micropaleontology 173, 102114. https://doi.org/10.1016/j.marmicro.2022.102114.

Aguado, R., Company, M., O'Dogherty, L., Sandoval, J., Tavera, J.M., 2014. Late Hauterivian–early Barremian calcareous nannofossil biostratigraphy, palaeoceanography, and stable isotope record in the Subbetic domain (southern Spain). Cretaceous Research 49, 105–124. https://doi.org/10.1016/j.cretres.2014.02.006.

Aguirre-Urreta, B., Martinez, M., Schmitz, M., Lescano, M., Omarini, J., Tunik, M., Kuhnert, H., Concheyro, A., Rawson, P.F., Ramos, V.A., Reboulet, S., Noclin, N., Frederichs, T., Nickl, A.-L., Pälike, H., 2019. Interhemispheric radio-astrochronological calibration of the time scales from the Andean and the Tethyan areas in the Valanginian-Hauterivian (Early Cretaceous). Gondwana

Research 70, 104–132. https://doi.org/10.1016/j.gr.2019.01.006.

Aguirre-Urreta, M.B., Price, G.D., Ruffell, A.H., Lazo, D.G., Kalin, R.M., Ogle, N., Rawson, P.F., 2008. Southern Hemisphere early Cretaceous (Valanginian-early Barremian) carbon and oxygen isotope curves from the Neuquen Basin, Argentina. Cretaceous Research 29, 87–99. https://doi.org/10.1016/j.cretres.2007.04.002.

Aguirre-Urreta, B., Schmitz, M., Lescano, M., Tunik, M., Rawson, P.F., Concheyro, A., Buhler, M., Ramos, V.A., 2017. A high precision U–Pb radioisotopic age for the Agrio Formation, Neuquén Basin, Argentina: Implications for the chronology of the Hauterivian Stage. Cretaceous Research 75, 193–204. https://doi.org/10.1016/j.cretres.2017.03.027.

Alley, N.F., Hore, S.B., Frakes, L.A., 2020. Glaciations at high-latitude Southern Australia during the Early Cretaceous. Australian Journal of Earth Sciences 67, 1045–1065. https://doi.org/10.1080/08120099.2019.1590457.

Armstrong, H.A., Wagner, T., Herringshaw, L.G., Farnsworth, A.J., Lunt, D.J., Harland, M., Imber, J., Loptson, C., Atar, E.F., 2016. Hadley circulation and precipitation changes controlling black shale deposition in the Late Jurassic Boreal Seaway. Paleoceanography 31, 1041–1053. https://doi.org/10.1002/2015PA002911.

Bacha, R.R.B., Waichel, B.L., Ernst, R.E., 2022. The mafic volcanic climax of the Paraná-Etendeka Large Igneous Province as the trigger of the Weissert Event. Tera Nova 34, 28–36. https://doi.org/10.1111/ter.12558.

Barrier, E., Vrielynck, B., Brouillet, J.-F., Brunet, M.-F., 2018. Map 7: Hauterivian, in: Barrier, E., Vrielynck, B., Brouillet, J.-F., Brunet, M.-F. (Eds.), Darius Program: Paleotectonic Reconstruction of the Central Tethyan Realm: Tectonono-Sedimentary-Palinspastic Maps from Late Permian to Pliocene: Atlas of 20 Maps. Commission for the Geological Map of the World, Paris, France.

Barbarin, N., Bonin, A., Mattioli, E., Pucéat, E., Cappetta, H., Gréselle, B., Pittet, B., Vennin, E., Joachimski, M., 2012. Evidence for a complex Valanginian nannoconid decline in the Vocontian basin (South East France). Marine Micropaleontology 84, 37–53.

https://doi.org/10.1016/j.marmicro.2011.11.005.

Baudin, F., 2005. A Late Hauterivian short-lived anoxic event in the Mediterranean Tethys: the 'Faraoni Event'. Comptes Rendus Geoscience 337, 1532–1540. https://doi.org/10.1016/j.crte.2005.08.012.

Baudin, F., Riquier, L., 2014. The late Hauterivian Faraoni 'oceanic anoxic event': an update. Bulletin de la Société Géologique de France 185, 359–377. https://doi.org/10.2113/gssgfbull.185.6.359.

Baudin, F., Bulot, L.G., Cecca, F., Coccioni, R., Gardin, S., Renard, M., 1999. Un équivalent du" Niveau Faraoni" dans le Bassin du Sud-Est de la France, indice possible d'un événement anoxique fini-hauterivien étendu à la Téthys méditerranéenne. Bulletin de la Société géologique de France 170, 487–498.

Baudin, F., Cecca, F., Galeotti, S., Coccioni, R., 2002. Palaeoenvironmental controls of the distribution of organic matter within a Corg-rich marker bed (Faraoni level, uppermost Hauterivian, central Italy). Eclogae Geologicae Helvetiae 95, 1–13. https://doi.org/10.5169/seals-168942.

Blanc, E., 1996. Transect plate-forme-bassin dans les séries carbonatées du Berriasien supérieur et du Valanginien inférieur (domaines jurassien et nord vocontien): chronostratigraphie-transferts des sédiments (Doctoral dissertation, Université Joseph-Fourier-Grenoble I), Grenoble, France. https://hal.archives-ouvertes.fr/tel-00723723/.

Blard, P.-H., Suchéras-Marx, B., Suan, G., Godet, B., Dutilleul, J., Mezine, T., Adatte, T., 2023. Are marl-limestone alternations mainly driven by $CaCO_3$ variations at the astronomical timescale? New insights from extraterrestrial ^{3}He. Earth and Planetary Science Letters, in review. https://doi.org/10.31223/X5807J.

Bodin, S., Fiet, N., Godet, A., Matera, V., Westermann, S., Clément, A., Janssen, N.M.M., Stille, P., Föllmi, K.B., 2009. Early Cretaceous (late Berriasian to early Aptian) palaeoceanographic change along the northwestern Tethyan margin (Vocontian Trough, southeastern France): $\delta^{13}C$, $\delta^{18}O$ and Sr-isotope belemnite and whole-rock records. Cretaceous Research 30, 1247–1262. https://doi.org/10.1016/j.cretres.2009.06.006.

Bodin, S., Godet, A., Föllmi, K.B., Vermeulen, J., Arnaud, H., Strasser, A., Fiet, N., Adatte, T., 2006a. The

Late Hauterivian Faraoni oceanic anoxic event in the western Tethys: Evidence from phosphorus burial rates. Palaeogeography, Palaeoclimatology, Palaeoecology 235, 245–264. https://doi.org/10.1016/j.palaeo.2005.09.030.

Bodin, S., Godet, A., Vermeulen, J., Linder, P., Föllmi, K.B., 2006b. Biostratigraphy, sedimentology and sequence stratigraphy of the latest Hauterivian–Early Barremian drowning episode of the Northern Tethyan margin (Altmann Member, Helvetic nappes, Switzerland). Eclogae Geologicae Helvetiae 99, 157–174. https://doi.org/10.1007/s00015-006-1188-7.

Bodin, S., Meissner, P., Janssen, N.M.M., Steuber, T., Mutterlose, J., 2015. Large igneous provinces and organic carbon burial: Controls on global temperature and continental weathering during the Early Cretaceous. Global and Planetary Change 133, 238–253. https://doi.org/10.1016/j.gloplacha.2015.09.001.

Bornemann, A., Mutterlose, J., 2008. Calcareous nannofossil and δ13C records from the Early Cretaceous of the Western Atlantic Ocean: evidence for enhanced fertilization across the Berriasian–Valanginian transition. Palaios 23, 821–832. https://doi.org/10.2110/palo.2007.p07-076r.

Boulila, S., Charbonnier, G., Galbrun, B., Gardin, S., 2015. Climatic precession is the main driver of Early Cretaceous sedimentation in the Vocontian Basin (France): Evidence from the Valanginian Orpierre succession. Sedimentary Geology 324, 1–11. https://doi.org/10.1016/j.sedgeo.2015.04.014.

Bralower, T.J., Arthur, M.A., Leckie, R.M., Sliter, W.V., Allard, D.J., Schlanger, S.O., 1994. Timing and paleoceanography of oceanic dysoxia/anoxia in the Late Barremian to Early Aptian (Early Cretaceous). Palaios 9, 335–369. https://doi.org/10.2307/3515055.

Bulot, L.G., Thieuloy, J.-P., Blanc, E., Klein, J., 1992. Le cadre stratigraphique du Valanginien supérieur et de l'Hauterivien du Sud-Est de la France : définition des biochronozones et caractérisation de nouveaux biohorizons. Géologie alpine 68, 13–56. http://geologie-alpine.ujf-grenoble.fr/articles/GA_1992__68__13_0.pdf.

Bulot, L.G., 1996. The Valanginian Stage. Bulletin de l'Institut Royal des Sciences Naturelles de Belgique

66(Supplement), 11–18.

Burgener, L., Hyland, E., Reich, B.J., Scotese, C., 2023. Cretaceous climates: Mapping paleo-Köppen climatic zones using a Bayesian statistical analysis of lithologic, paleontologic, and geochemical proxies. Palaeogeography, Palaeoclimatology, Palaeoecology 613, 111373. https://doi.org/10.1016/j.palaeo.2022.111373.

Busnardo, R., Thieuloy, J.-P., Moullade, M., 1979. Hypostratotype mésogéen de l'étage Valanginien (Sud-Est de la France). Editions du C.N.R.S., Paris, France.

Cavalheiro, L., Wagner, T., Steinig, S., Bottini, C., Dummann, W., Esegbue, O., Gambacorta, G., Giraldo-Gómez, V., Farnworsth, A., Flögel, S., Hofmann, P., Lunt, D.J., Rethmeyer, J., Torricelli, S., Erba, E., 2021. Impact of global cooling on Early Cretaceous high pCO_2 world during the Weissert Event. Nature Communications 12, 5411. https://doi.org/10.1038/s41467-021-25706-0.

Cecca, F., Marini, A., Pallini, G., Baudin, F., Begouen, V., 1994. A guide-level of the uppermost Hauterivian (Lower Cretaceous) in the pelagic succession of Umbria-Marche Apennines (Central Italy): the Faraoni Level. Rivista italiana di Paleontologia e Stratigrafia 99, 551–568.

Channell, J.E.T., Cecca, F., Erba, E., 1995. Correlations of Hauterivian and Barremian (Early Cretaceous) stage boundaries to polarity chrons. Earth and Planetary Science Letters 134(1-2), 125–140. https://doi.org/10.1016/0012-821X(95)00111-O.

Channell, J.E.T., Erba, E., Muttoni, G., Tremolada, F., 2000. Early Cretaceous magnetic stratigraphy in the APTICORE drill core and adjacent outcrop at Cismon (Southern Alps, Italy), and correlation to the proposed Barremian-Aptian boundary stratotype. Geological Society of America Bulletin 112, 1430–1443. https://doi.org/10.1130/0016-7606(2000)112<1430:ECMSIT>2.0.CO;2.

Charbonnier, G., Boulila, S., Gardin, S., Duchamp-Alphonse, S., Adatte, T., Spangenberg, J.E., Föllmi, K., Colin, C., Galbrun, B., 2013. Astronomical calibration of the Valanginian "Weissert" episode: The Orpierre marl–limestone succession (Vocontian Basin, southeastern France). Cretaceous Research 45, 25–42. https://doi.org/10.1016/j.cretres.2013.07.003.

Charbonnier, G., Duchamp-Alphonse, S., Adatte, T., Föllmi, K.B., Spangenberg, J.E., Gardin, S., Galbrun,

B., Colin, C., 2016. Eccentricity paced monsoon-like system along the northwestern Tethyan margin during the Valanginian (Early Cretaceous): New insights from detrital and nutrient fluxes into the Vocontian Basin (SE France). Palaeogeography, Palaeoclimatology, Palaeoecology 443, 145–155. https://doi.org/10.1016/j.palaeo.2015.11.027.

Charbonnier, G., Duchamp-Alphonse, S., Deconinck, J.-F., Adatte, T., Spangenberg, J. E., Colin, C., Föllmi, K.B., 2020. A global palaeoclimatic reconstruction for the Valanginian based on clay mineralogical and geochemical data. Earth-Science Reviews 202, 103092. https://doi.org/10.1016/j.earscirev.2020.103092.

Charbonnier, G., Morales, C., Duchamp-Alphonse, S., Westermann, S., Adatte, T. and Föllmi, K.B., 2017. Mercury enrichment indicates volcanic triggering of Valanginian environmental change. Scientific Reports 7, 40808. https://doi.org/10.1038/srep40808.

Cleveland, W.S., 1979. Robust Locally Weighted Regression and Smoothing Scatterplots. Journal of American Statistical Association 74, 829–836. https://doi.org/10.2307/2286407.

Coccioni, R., Galeotti, S., Sprovieri, M., 2003. The Mid-Barremian Event (MBE): the prelude to the OAE1a. In AGU Fall Meeting Abstracts (Vol. 2003, pp. PP41B-0835). https://ui.adsabs.harvard.edu/abs/2003AGUFMPP41B0835C/abstract.

Company, M., Sandoval, J., Tavera, J.M., 2003. Ammonite biostratigraphy of the uppermost Hauterivian in the Betic Cordillera (SE Spain). Geobios 36, 685–694. https://doi.org/10.1016/j.geobios.2002.12.001.

Company, M., Aguado, R., Sandoval, J., Tavera, J.M., de Cisneros, C.J., Vera, J.A., 2005. Biotic changes linked to a minor anoxic event (Faraoni Level, latest Hauterivian, Early Cretaceous). Palaeogeography, Palaeoclimatology, Palaeoecology 224, 186–199. https://doi.org/10.1016/j.palaeo.2005.03.034.

Cotillon, P., 1971. Le Crétacé inférieur de l'arc subalpin de Castellane entre l'Asse et le Var, stratigraphie et sédimentologie. Mémoires du BRGM, Orléans, France.

Cotillon, P., Rio, M., 1984. Cyclic sedimentation in the Cretaceous of Deep Sea Drilling Project sites 534

and 540 (Gulf of Mexico), 534 (Centrl Atlantic), and in the Vocontian Basin (France), in: Bufler, R. T., Schlager, W., et al., Initial Reports DSDP 77, Washington (U.S. Govt. Printing Office), USA, pp. 339–376.

Cotillon, P., Ferry, S., Gaillard, C., Jautée, E., Latreille, G., Rio, M., 1980. Fluctuation des paramètres du milieu marin dans le domaine vocontien (France Sud-Est) au Crétacé inférieur : mise en évidence par l'étude des formations marno-calcaires alternantes. Bulletin de la Société Géologique de France 7-XXII, 735–744. https://doi.org/10.2113/gssgfbull.S7-XXII.5.735.

Davies, A., Gréselle, B., Hunter, S.J., Baines, G., Robson, C., Haywood, A.M., Ray, D.C., Simmons, M.D., van Buchem, F.S.P., 2020. Assessing the impact of aquifer-eustasy on short-term Cretaceous sea-level. Cretaceous Research 112, 104445. https://doi.org/10.1016/j.cretres.2020.104445.

Deconinck, J.-F., Chamley, H., 1983. Héritage et diagenèse des minéraux argileux dans les alternances marno-calcaires du Crétacé inférieur du domaine subalpin. Comptes-rendus des séances de l'Académie des sciences. Série 2, Mécanique-physique, chimie, sciences de l'univers, sciences de la terre 297, 589–594.

Delanoy, G., 1997. Biostratigraphie des faunes d'ammonites à la limite Barrémien–Aptien dans la région d'Angles–Barrême–Castellane. Etude particulière de la famille des Heteroceratidae Spath, 1922 (Ancyloceratina, Ammonoidea). Annales du Muséum d'Histoire Naturelle de Nice 12, 1–270.

Dodd, S.C., Mac Niocaill, C., Muxworthy, A.R., 2015. Long duration (> 4 Ma) and steady-state volcanic activity in the early Cretaceous Paraná–Etendeka Large Igneous Province: New palaeomagnetic data from Namibia. Earth and Planetary Science Letters 414, 16–29. http://doi.org/10.1016/j.epsl.2015.01.009.

Donnadieu, Y., Pierrehumbert, R., Jacob, R., Fluteau, F., 2006. Modelling the primary control of paleogeography on Cretaceous climate. Earth and Planetary Science Letters 248, 426–437. https://doi.org/10.1016/j.epsl.2006.06.007.

Duchamp-Alphonse, S., Fiet, N., Adatte, T., Pagel, M., 2011. Climate and sea-level variations along the northwestern Tethyan margin during the Valanginian C-isotope excursion: mineralogical evidence

from the Vocontian Basin (SE France). Palaeogeography, Palaeoclimatology, Palaeoecology 302, 243–254. https://doi.org/10.1016/j.palaeo.2011.01.015.

Duchamp-Alphonse, S., Gardin, S., Bartolini, A., 2014. Calcareous nannofossil response to the Weissert episode (Early Cretaceous): Implications for palaeoecological and palaeoceanographic reconstructions. Marine Micropaleontology 113, 65–78. https://doi.org/10.1016/j.marmicro.2014.10.002.

Duchamp-Alphonse, S., Gardin, S., Fiet, N., Bartolini, A., Blamart, D., Pagel, M., 2007. Fertilization of the northwestern Tethys (Vocontian basin, SE France) during the Valanginian carbon isotope perturbation: evidence from calcareous nannofossils and trace element data. Palaeogeography, Palaeoclimatology, Palaeoecology, 243, 132–151. https://doi.org/10.1016/j.palaeo.2006.07.010.

Emmanuel, L., Renard, M., 1993. Carbonate geochemistry (Mn, $\delta^{13}C$, $\delta^{18}O$) of the late Tithonian–Berriasian pelagic limestones of the Vocontian trough (SE France). Bulletin du Centre de Recherche et d'Exploration d'Elf-Aquitaine 17, 205–221.

Erba, E., Bartolini, A., Larson, R. L., 2004. Valanginian Weissert oceanic anoxic event. Geology, 32, 149–152. https://doi.org/10.1130/G20008.1.

Ferry, S., 1987. Le détritisme carbonate profond dans le Crétacé inférieur du sud-est français. Ses rapports avec l'eustatisme. Géologie alpine, Mémoires H.S. n°13.

Ferry, S. Monier, P., 1987. Correspondances entre alternances marno-calcaires de bassin et de plate-forme (Crétacé du SE de la France). Bulletin de la Société géologique de France 3, 961–963.

Fesneau, C., 2008. Enregistrement des changements climatiques dans le Domaine Téthysien au Valanginien (Doctoral dissertation, Université de Bourgogne), Dijon, France.

Fesneau, C., Deconinck, J.-F., Pellenard, P., Reboulet, S., 2009. Evidence of aerial volcanic activity during the Valanginian along the northern Tethys margin. Cretaceous Research 30, 533–539. https://doi.org/10.1016/j.cretres.2008.09.004.

Fiet, N., Gorin, G., 2000. Lithological expression of Milankovitch cyclicity in carbonate-dominated, pelagic, Barremian deposits in central Italy. Cretaceous Research 21, 457–467.

https://doi.org/10.1006/cres.2000.0220.

Fiet, N., Quidelleur, X., Parize, O., Bulot, L.G., Gillot, P.Y., 2006. Lower Cretaceous stage durations combining radiometric data and orbital chronology: towards a more stable relative time scale? Earth and Planetary Science Letters 246, 407–417. https://doi.org/10.1016/j.epsl.2006.04.014.

Föllmi, K.B., 1995. 160 m.y. record of marine sedimentary phosphorus burial: Coupling of climate and continental weathering under greenhouse and icehouse conditions. Geology 23, 859–862. https://doi.org/10.1130/0091-7613(1995)023<0503:MYROMS>2.3.CO;2.

Föllmi, K.B., 2012. Early Cretaceous life, climate and anoxia. Cretaceous Research 35, 230–257. https://doi.org/10.1016/j.cretres.2011.12.005.

Föllmi, K.B., Bôle, M., Jammet, N., Froidevaux, P., Godet, A., Bodin, S., Adatte, T., Matera, V., Fleitmann, D, Spangenberg, J.E., 2012. Bridging the Faraoni and Selli oceanic anoxic events: late Hauterivian to early Aptian dysaerobic to anaerobic phases in the Tethys. Climate of the Past 8, 171–189. https://doi.org/10.5194/cp-8-171-2012.

Föllmi, K.B., Godet, A., Bodin, S., Linder, P., 2006. Interactions between environmental change and shallow water carbonate buildup along the northern Tethyan margin and their impact on the Early Cretaceous carbon isotope record. Paleoceanography 21, PA4211. https://doi.org/10.1029/2006PA001313.

Föllmi, K.B. Weissert, H., Bisping, M., Funk, H., 1994. Phosphogenesis, carbon-isotope stratigraphy, and carbonate-platform evolution along the Lower Cretaceous northern Tethyan margin. Geological Society of America Bulletin, 106, 729–746. https://doi.org/10.1130/0016-7606(1994)106<0729:PCISAC>2.3.CO;2.

Frank, H.T., Gomes, M.E.B., Formoso, M.L.L., 2009. Review of the areal extent and the volume of the Serra Geral Formation, Paraná Basin, South America. Pesquisas em Geociências 36, 49–57. https://doi.org/10.22456/1807-9806.17874.

Frau, C., Bulot, L.G., Delanoy, G., Moreno-Bedmar, J.A., Masse, J.P., Tendil, A.J., Lanteaume, C., 2018. The Aptian GSSP candidate at Gorgo a Cerbara (Central Italy): an alternative interpretation of the

bio-, litho-and chemostratigraphic markers. Newsletters on Stratigraphy 51, 311–326. https:/doi.org/10.1127/nos/2017/0422.

Frau, C., Tendil, A.J.B., Pohl, A., Lanteaume, C., 2020. Revising the timing and causes of the Urgonian rudistid-platform demise in the Mediterranean Tethys. Global and Planetary Change 187, 103124. https://doi.org/10.1016/j.gloplacha.2020.103124.

Frizon de Lamotte, D., Fourdan, B., Leleu, S., Leparmentier, F., Clarens, P. de, 2015. Style of rifting and the stages of Pangea breakup. Tectonics 34, 1009–1029. https://doi.org/10.1002/2014TC003760.

Gale, A.S., Mutterlose, J., Batenburg, S., 2020. The Cretaceous Period, in: F.M. Gradstein, J.G. Ogg, M.D. Schmitz, G.M. Ogg (Eds.), Geologic Time Scale 2020, vol. 2, chap. 27, Elsevier B.V., Amsterdam, The Netherlands, pp. 1023–1086. https://doi.org/10.1016/B978-0-12-824360-2.00027-9.

Gardin, S., 2008. The nannofossil succession of la Charce across the Valanginian-Hauterivian boundary, in: E. Mattioli (Ed.), 12th Meeting of the International Nannoplankton Association (Lyon, September 7-10, 2008). http://paleopolis.rediris.es/cg/BOOKS/CG2008_B01/index.html.

Ghirardi, J., Deconinck, J.-F., Pellenard, P., Martinez, M., Bruneau, L., Amiotte-Suchet, P. and Pucéat, E., 2014. Multi-proxy orbital chronology in the aftermath of the Aptian Oceanic anoxic event 1a: Palaeoceanographic implications (Serre Chaitieu section, Vocontian Basin, SE France). Newsletters on Stratigraphy 47, 247–262. https://doi.org/10.1127/0078-0421/2014/0046.

Giraud, F., 1994. Recherche des périodicités astronomiques et des fluctuations du niveau marin à partir de l'étude du signal carbonaté des séries pélagiques alternantes. Application au Crétacé inférieur du Sud-Est de la France (Bassin Vocontien), de l'Atlantique Central (Site 534 DSDP) et du Golfe du Mexique (Site 535 DSDP) (Doctoral dissertation, Université Claude Bernard Lyon 1), Lyon, France. https://www.persee.fr/doc/geoly_0750-6635_1995_mon_134_1.

Giraud, F., Beaufort, L., Cotillon, P., 1995. Periodicities of carbonate cycles in the Valanginian of the Vocontian Trough: a strong obliquity control. Geological Society, London, Special Publications 85, 143–164. https://doi.org/10.1144/GSL.SP.1995.085.01.09.

Giraud, F., Reboulet, S., Deconinck, J.-F., Martinez, M., Carpentier, A., Bréziat, C., 2013. The Mid-

Cenomanian Event in southeastern France: evidence from palaeontological and clay mineralogical data. Cretaceous Research 46, 43–58. https://doi.org/10.1016/j.cretres.2013.09.004.

Godet, A., 2013. Drowning unconformities: Palaeoenvironmental significance and involvement of global processes. Sedimentary Geology 293, 45–66. https://doi.org/10.1016/j.sedgeo.2013.05.002.

Godet, A., Bodin, S., Föllmi, K.B., Vermeulen, J., Gardin, S., Fiet, N., Adatte, T., Berner, Z., Stüben, D., van de Schootbrugge, B., 2006. Evolution of the marine stable carbon-isotope record during the early Cretaceous: A focus on the late Hauterivian and Barremian in the Tethyan realm. Earth and Planetary Science Letters 242, 254–271. https://doi.org/10.1016/j.epsl.2005.12.011.

Godet, A., Föllmi, K.B., Spangenberg, J.E., Bodin, S., Vermeulen, J., Adatte, T., Bonvallet, L., Arnaud, H., 2013. Deciphering the message of Early Cretaceous drowning surfaces from the Helvetic Alps: What can be learnt from platform to basin correlations? Sedimentology 60, 152–173.

Godet, A., Föllmi, K.B., Stille, P., Bodin, S., Matera, V., Adatte, T., 2011. Reconciling strontium-isotope and K–Ar ages with biostratigraphy: the case of the Urgonian platform, Early Cretaceous of the Jura Mountains, Western Switzerland. Swiss Journal of Geosciences, 104, 147–160. https://doi.org/10.1007/s00015-011-0053-5.

Gomes, A.S., Vasconcelos, P.M., 2021. Geochronology of the Paraná-Etendeka large igneous province. Earth-Science Reviews 220, 103716. https://doi.org/10.1016/j.earscirev.2021.103716.

Graciansky, P.-C. de, Lemoine, M., 1988. Early Cretaceous extensional tectonics in the southwestern French Alps; a consequence of North-Atlantic rifting during Tethyan spreading. Bulletin de la Société Géologique de France 8-IV, 733–737. https://doi.org/10.2113/gssgfbull.IV.5.733.

Gréselle, B., Pittet, B., 2010. Sea-level reconstructions from the Peri-Vocontian Zone (South-east France) point to Valanginian glacio-eustasy. Sedimentology 57, 1640–1684. https://doi.org/10.1111/j.1365-3091.2010.01159.x.

Gréselle, B., Pittet, B., Mattioli, E., Joachimski, M., Barbarin, N., Riquier, L., Reboulet, S., Pucéat, E., 2011. The Valanginian isotope event: A complex suite of palaeoenvironmental perturbations. Palaeogeography, Palaeoclimatology, Palaeoecology 306, 41–57.

https://doi.org/10.1016/j.palaeo.2011.03.027.

Gröcke, D.R., Price, G.D., Robinson, S.A., Baraboshkin, E.Y., Mutterlose, J., Ruffell, A.H., 2005. The Upper Valanginian (Early Cretaceous) positive carbon–isotope event recorded in terrestrial plants. Earth and Planetary Science Letters 240, 495–509. https://doi.org/10.1016/j.epsl.2005.09.001.

Hardenbol, J., Thierry, J., Farley, M.B., Jacquin, T., de Graciansky, P.-C., Vail, P.R., 1998. Mesozoic and Cenozoic sequence stratigraphy of European basins. SEPM Special Publications 60, Tulsa, OK.

Harry, D.L., Tejada, M.L.G., Lee, E.Y., Wolfgring, E., Wainman, C.C., Brumsack, H.J., Schnetger, B., Kimura, J.I., Riquier, L., Borissova, I., Hobbs, R.W., Jiang, T., Li, Y. Y., Mariati, A., Martinez, M., Richter, C., Tagliaro, G., White, L.T., 2020. Evolution of the southwest Australian rifted continental margin during breakup of East Gondwana: Results from International Ocean Discovery Program Expedition 369. Geochemistry, Geophysics, Geosystems 21, e2020GC009144. https://doi.org/10.1029/2020GC009144.

He, H., Pan, Y., Tauxe, L., Qin, H., Zhu, R., 2008. Toward age determination of the M0r (Barremian–Aptian boundary) of the Early Cretaceous. Physics of the Earth and Planetary Interiors 169, 41–48. https://doi.org/10.1016/j.pepi.2008.07.014.

Hennig, S., Weissert, H., Bulot, L., 1999. C-isotope stratigraphy, a calibration tool between ammonite-and magnetostratigraphy: the Valanginian–Hauterivian transition. Geologica Carpathica 50, 91–95. http://www.geologicacarpathica.com/browse-journal/volumes/50-1/article-120.

Hinnov, L.A., 2000. New perspectives on Orbitally Forced Stratigraphy. Annual Review of Earth and Planetary Sciences 28, 419–475. https://doi.org/10.1146/annurev.earth.28.1.419.

Hinnov, L.A., 2018. Cyclostratigraphy and Astrochronology in 2018, in: M. Montenari (Ed.), Stratigraphy and Timescales: Cyclostratigraphy and Astrochronology, Vol. 3, Elsevier B.V., Amsterdam, The Netherlands, pp. 1–80. https://doi.org/10.1016/bs.sats.2018.08.004.

Hinnov, L.A., Schulz, M., Yiou, P., 2002. Interhemispheric space–time attributes of the Dansgaard–Oeschger oscillations between 100 and 0 ka. Quaternary Science Reviews 21, 1213–1228. https://doi.org/10.1016/S0277-3791(01)00140-8.

Hoedemaeker, P.J., Leereveld, H., 1995. Biostratigraphy and sequence stratigraphy of the Berriasian-lowest Aptian (Lower Cretaceous) of the Rio Argos succession, Caravaca, SE Spain. Cretaceous Research 16, 195–230. https://doi.org/10.1006/cres.1995.1016.

Hoedemaeker, P. J., Krs, M., Man, O., Pares, J.M., Pruner, P., Venhodova, D., 1998. The Neogene remagnetization and petromagnetic study of the Early Cretaceous limestone beds from the Río Argos (Caravaca, Province of Murcia, SE Spain). Geologica Carpathica 49, 15–32.

Hollaar, T.P., Hesselbo, S.P., Deconinck, J.-F., Damaschke, M., Ullmann, C.V., Jiang, M., Belcher, C.M., 2022. Environmental changes during the onset of the Late Pliensbachian Event (Early Jurassic) in the Mochras Borehole, Cardigan Bay Basin, NW Wales. Climate of the Past Discussions, in review. https://doi.org/10.5194/cp-2022-87.

Homberg, C., Schnyder, J., Benzaggagh, M., 2013. Late Jurassic-Early Cretaceous faulting in the Southeastern French basin: does it reflect a tectonic reorganization? Bulletin de la Société Géologique de France 184, 501–514. https://doi.org/10.2113/gssgfbull.184.4-5.501.

Huang, Z., Ogg, J.G., Gradstein, F.M., 1993. A quantitative study of Lower Cretaceous cyclic sequences from the Atlantic Ocean and the Vocontian Basin (SE France). Paleoceanography, 8, 275–291. https://doi.org/10.1029/93PA00253

Huck, S., Heimhofer, U., 2021. Early Cretaceous sea surface temperature evolution in subtropical shallow seas. Scientific Reports 11, 15765. https://doi.org/10.1038/s41598-021-99094-2.

Janasi, V.A., de Freitas, V.A., Heaman, L.H., 2011. The onset of flood basalt volcanism, Northern Paraná Basin, Brazil: A precise U–Pb baddeleyite/zircon age for a Chapecó-type dacite. Earth and Planetary Science Letters 302, 147–153. https://doi.org/10.1016/j.epsl.2010.12.005.

Jerolmack, D.J., Paola, C., 2010. Shredding of environmental signals by sediment transport. Geophysical Research Letters, L19401, 37. 10.1029/2010GL044638.

Katz, B., Elmore, R.D., Cogoini, M., Engel, M.H., Ferry, S., 2000. Associations between burial diagenesis of smectite, chemical remagnetization, and magnetite authigenesis in the Vocontian trough, SE France. Journal of Geophysical Research: Solid Earth 105(B1), 851–868.

https://doi.org/10.1029/1999JB900309.

Kenjo, S., Reboulet, S., Mattioli, E., Ma'louleh, K., 2021. The Berriasian–Valanginian boundary in the Mediterranean Province of the Tethyan Realm: Ammonite and calcareous nannofossil biostratigraphy of the Vergol section (Montbrun-les-Bains, SE France), candidate for the Valanginian GSSP. Cretaceous Research 121, 104738. https://doi.org/10.1016/j.cretres.2020.104738.

Kuhnt, W., Moullade, M., Masse, J.P. and Erlenkeuser, H., 1998. Carbon isotope stratigraphy of the lower Aptian historical stratotype at Cassis-La Bédoule (SE France). Géologie Méditerranéenne 25, 63–79. https://doi.org/10.3406/geolm.1998.1625.

Kujau, A., Heimhofer, U., Hochuli, P.A., Pauly, S., Morales, C., Adatte, T., Föllmi, K., Ploch, I., Mutterlose, J., 2013. Reconstructing Valanginian (Early Cretaceous) mid-latitude vegetation and climate dynamics based on spore–pollen assemblages. Review of Palaeobotany and Palynology 197, 50–69. https://doi.org/10.1016/j.revpalbo.2013.05.003.

Kujau, A., Heimhofer, U., Ostertag-Henning, C., Gréselle, B., Mutterlose, J., 2012. No evidence for anoxia during the Valanginian carbon isotope event—an organic-geochemical study from the Vocontian Basin, SE France. Global and Planetary Change 92, 92–104. https://doi.org/10.1016/j.gloplacha.2012.04.007.

Ladant, J.-B., Donnadieu, Y., 2016. Palaeogeographic regulation of glacial events during the Cretaceous supergreenhouse. Nature Communications 7, 1–9. https://doi.org/10.1038/ncomms12771.

Laskar, J., Fienga, A., Gastineau, M., Manche, H., 2011. La2010: a new orbital solution for the long-term motion of the Earth. Astronomy & Astrophysics 532, A89. https://doi.org/10.1051/0004-6361/201116836.

Laskar, J., Robutel, P., Joutel, F., Gastineau, M., Correia, A.C.M., Levrard, B., 2004. A long-term numerical solution for the insolation quantities of the Earth. Astronomy & Astrophysics 428, 261–285. https://doi.org/10.1051/0004-6361:20041335

Lehmann, J., Ifrim, C., Bulot, L., Frau, C., 2015. Paleobiogeography of Early Cretaceous ammonoids. in:

Klug, C., et al. (Eds.), Ammonoid Paleobiology: From Macroevolution to Paleogeography. Topics in Geobiology vol. 44, pp. 229–258. https://doi.org/10.1007/978-94-017-9633-0_9.

Lemoine, M., Bas, T., Arnaud-Vanneau, A., Arnaud, H., Dumont, T., Gidon, M., Bourbon, M., Graciansky, P.-C. de, Rudkiewicz, J.-L., Megard-Galli, J., Tricart, P., 1986. The continental margin of the Mesozoic Tethys in the Western Alps. Marine and Petroleum Geology 3, 179–199. https://doi.org/10.1016/0264-8172(86)90044-9.

Lézine, A.M., Bassinot, F., Peterschmitt, J.Y., 2014. Orbitally-induced changes of the Atlantic and Indian monsoons over the past 20,000 years: New insights based on the comparison of continental and marine records. Bulletin de la Société Géologique de France 185, 3–12. https://doi.org/10.2113/gssgfbull.185.1.3.

Lin, H., 2011. Three principles of soil change and pedogenesis in time and space. Soil Science Society of America Journal 75, 2049–2070. https://doi.org/10.2136/sssaj2011.0130.0.

Lini, A., Weissert, H., Erba, E., 1992. The Valanginian carbon isotope event: a first episode of greenhouse climate conditions during the Cretaceous. Terra Nova 4, 374–384. https://doi.org/10.1111/j.1365-3121.1992.tb00826.x.

Malkoč, M., Mutterlose, J., 2010. The early Barremian warm pulse and the late Barremian cooling: a high-resolution geochemical record of the Boreal Realm. Palaios 25, 14–23. https://doi.org/10.2110/palo.2010.p09-029r.

Mann, M.E., Lees, J.M., 1996. Robust estimation of background noise and signal detection in climatic time series. Climatic change 33, 409–445. https://doi.org/10.1007/BF00142586.

Martín-Chivelet, J., López-Gómez, J., et al. (44 co-authors), 2019. The Late Jurassic–Early Cretaceous Rifting, in: Quesada, C., Oliveira, J.T. (Eds.), The Geology of Iberia: A Geodynamic Approach: The Alpine Cycle, Vol. 3, Springer Nature Switzerland, Cham, Switzerland, pp. 169–249. https://doi.org/10.1007/978-3-030-11295-0_5.

Martinez, M., 2018. Mechanisms of preservation of the eccentricity and longer-term Milankovitch cycles in detrital supply and carbonate production in hemipelagic marl-limestone alternations, in: M.

Montenari (Ed.), Stratigraphy and Timescales: Cyclostratigraphy and Astrochronology, Vol. 3, Elsevier B.V., Amsterdam, The Netherlands, pp. 189–219. https://doi.org/10.1016/bs.sats.2018.08.002.

Martinez, M., Dera, G., 2015. Orbital pacing of carbon fluxes by a ~9-My eccentricity cycle during the Mesozoic. Proceedings of the National Academy of Sciences of the United States of America 112, 12604–12609. https://doi.org/10.1073/pnas.1419946112.

Martinez, M., Aguado, R., Company, M., Sandoval, J., O'Dogherty, L., 2020a. Integrated astrochronology of the Barremian Stage (Early Cretaceous) and its biostratigraphic subdivisions. Global and Planetary Change 195, 103368. https://doi.org/10.1016/j.gloplacha.2020.103368.

Martinez, M., Deconinck, J.-F., Pellenard, P., Reboulet, S., Riquier, L., 2013. Astrochronology of the Valanginian Stage and palaeoenvironmental implications for the Weissert Event. Palaeogeography, Palaeoclimatology, Palaeoecology 376, 91–102. https://doi.org/10.1016/j.palaeo.2013.02.021.

Martinez, M., Deconinck, J.-F., Pellenard, P., Riquier, L., Company, M., Reboulet, S., Moiroud, M., 2015. Astrochronology of the Valanginian-Hauterivian stages (Early Cretaceous): Chronological relationships between the Paraná-Etendeka large igneous province and the Weissert and the Faraoni events. Global and Planetary Change 131, 158–173. https://doi.org/10.1016/j.gloplacha.2015.06.001.

Martinez, M., Guillois, L., Boulvais, P., Deconinck, J.-F., 2020b. Inverted responses of the carbon cycle to orbital forcing in Mesozoic periplatform marginal basins: Implications for astrochronology. Paleoceanography and Paleoclimatology 35, e2019PA003705. https://doi.org/10.1029/2019PA003705.

Martinez, M., Pellenard, P., Deconinck, J.-F., Monna, F., Riquier, L., Boulila, S., Moiroud, M., Company, M., 2012. An orbital floating time scale of the Hauterivian/Barremian GSSP from a magnetic susceptibility signal (Río Argos, Spain). Cretaceous Research 36, 106–115. https://doi.org/10.1016/j.cretres.2012.02.015.

Mattioli, E., Pittet, B., Riquier, L., Grossi, V., 2014. The mid-Valanginian Weissert Event as recorded by

calcareous nannoplankton in the Vocontian Basin. Palaeogeography, Palaeoclimatology, Palaeoecology 414, 472–485. https://doi.org/10.1016/j.palaeo.2014.09.030.

Matthews, R.K., Frohlich, C., 2002. Maximum flooding surfaces and sequence boundaries: comparisons between observations and orbital forcing in the Cretaceous and Jurassic (65-190 Ma). GeoArabia 7, 503–538.

McArthur, J.M., Janssen, N.M.M., Reboulet, S., Leng, M.J., Thirlwall, M.F., van de Schootbrugge, B., 2007. Palaeotemperatures, polar ice-volume, and isotope stratigraphy (Mg/Ca, δ18O, δ13C, 87Sr/86Sr): The Early Cretaceous (Berriasian, Valanginian, Hauterivian). Palaeogeography, Palaeoclimatology, Palaeoecology 248, 391–430. https://doi.org/10.1016/j.palaeo.2006.12.015.

Mena, M., Goguitchaichvili, A., Solano, M.C., Vilas, J.F., 2011. Paleosecular variation and absolute geomagnetic paleointensity records retrieved from the Early Cretaceous Posadas Formation (Misiones, Argentina). Studia Geophysica et Geodaetica 55, 279–309. https://doi.org/10.1007/s11200-011-0016-3.

Midtkandal, I., Svensen, H.H., Planke, S., Corfu, F., Polteau, S., Torsvik, T. H., Faleide, J.I., Grundvåg, S.-A., Selnes, H., Kürschner, W., Olausser, S., 2016. The Aptian (Early Cretaceous) oceanic anoxic event (OAE1a) in Svalbard, Barents Sea, and the absolute age of the Barremian-Aptian boundary. Palaeogeography, Palaeoclimatology, Palaeoecology 463, 126-135. https://doi.org/10.1016/j.palaeo.2016.09.023.

Moiroud, M., Martinez, M., Deconinck, J.-F., Monna, F., Pellenard, P., Riquier, L., Company, M., 2012. High-resolution clay mineralogy as a proxy for orbital tuning: Example of the Hauterivian–Barremian transition in the Betic Cordillera (SE Spain). Sedimentary Geology 282, 336–346. https://doi.org/10.1016/j.cretres.2012.02.015.

Morales, C., Gardin, S., Schnyder, J., Spangenberg, J., Arnaud-Vanneau, A., Arnaud, H., Adatte, T., Föllmi, K.B., 2013. Berriasian and early Valanginian environmental change along a transect from the Jura Platform to the Vocontian Basin. Sedimentology 60, 36–63. https://doi.org/10.1111/sed.12019.

Morales, C., Spangenberg, J.E., Arnaud-Vanneau, A., Adatte, T., Föllmi, K.B., 2016. Evolution of the northern Tethyan Helvetic Platform during the late Berriasian and early Valanginian. The Depositional Record 2, 47–73. https://doi.org/10.1002/dep2.13.

Moullade, M., Tronchetti, G., Busnardo, R., Masse, J.-P., 1998. Description lithologique des coupes types du stratotype historique de l'Aptien inférieur dans la région de Cassis-La Bédoule (SE France). Géologie Méditerranéenne 25, 15–29. https://doi.org/10.3406/geolm.1998.1621.

Mutterlose, J., Bornemann, A., 2000. Distribution and facies patterns of Lower Cretaceous sediments in northern Germany: a review. Cretaceous Research 21, 733–759. https://doi.org/10.1006/cres.2000.0232.

Mutterlose, J., Ruffell, A., 1999. Milankovitch-scale palaeoclimate changes in pale–dark bedding rhythms from the Early Cretaceous (Hauterivian and Barremian) of eastern England and northern Germany. Palaeogeography, Palaeoclimatology, Palaeoecology 154, 133–160. https://doi.org/10.1016/S0031-0182(99)00107-8.

Mutterlose, J., Malkoc, M., Schouten, S., Sinninghe Damsté, J.S., Forster, A., 2010. TEX_{86} and stable $\delta^{18}O$ paleothermometry of early Cretaceous sediments: Implications for belemnite ecology and paleotemperature proxy application. Earth and Planetary Science Letters 298, 286–298. https://doi.org/10.1016/j.epsl.2010.07.043.

Mutterlose, J., Malkoc, M., Schouten, S., Sinninghé Damsté, J.S., 2012. Reconstruction of vertical temperature gradients in past oceans—proxy data from the Hauterivian–early Barremian (Early Cretaceous) of the Boreal Realm. Palaeogeography, Palaeoclimatology, Palaeoecology 363, 135–143. https://doi.org/10.1016/j.palaeo.2012.09.006.

Mutterlose, J., Pauly, S., Steuber, T., 2009. Temperature controlled deposition of early Cretaceous (Barremian–early Aptian) black shales in an epicontinental sea. Palaeogeography, Palaeoclimatology, Palaeoecology 273, 330–345. https://doi.org/10.1016/j.palaeo.2008.04.026.

Mutterlose, J., Rawson, P. F., Reboulet, S., Baudin, F., Bulot, L., Emmanuel, L., Gardin, S., Martinez, M., Renard, M., 2021. The Global Boundary Stratotype Section and Point (GSSP) for the base of the

Hauterivian Stage (Lower Cretaceous), La Charce, southeast France. Episodes Journal of International Geoscience 44 129–150. https://doi.org/10.18814/epiiugs/2020/02007.

Myers, K.J., Wignall, P.B., 1987. Understanding Jurassic organic-rich mudrocks — new concepts using gamma-ray spectrometry and palaeoecology: examples from the Kimmeridge Clay of Dorset and the Jet Rock of Yorkshire. In: Legget, J.K., Zuffa, G.G. (Eds.), Marine Clastic Environments: Concepts and Case Studies. Graham and Trotman, London, pp. 172–189. https://doi.org/10.1007/978-94-009-3241-8_9.

O'Brien, C.L., Robinson, S.A., Pancost, R.D., Sinninghe Damsté, J.S., Schouten, S., Lunt, D.J., Alsenz, H., Bornemann, A., Bottini, C., Brassell, S.C., Farnsworth, A., Forster, A., Huber, B.T., Inglis, G.N., Jenkyns, H.C., Linnert, C., Littler, K., Markwick, P., McAnena, A., Mutterlose, J., Naafs, B.D.A., Püttmann, W., Sluijs, A., van Helmond, N.A.G.M., Vellekoop, J., Wagner, T., Wrobel, N.E., 2017. Cretaceous sea-surface temperature evolution: Constraints from TEX86 and planktonic foraminiferal oxygen isotopes. Earth-Science Reviews 172, 224–247. https://doi.org/10.1016/j.earscirev.2017.07.012.

Olierook, H.K.H., Merle, R.E., Jourdan, F., 2017. Toward a Greater Kerguelen large igneous province: Evolving mantle source contributions in and around the Indian Ocean. Lithos 282–283, 163–172. https://doi.org/10.1016/j.lithos.2017.03.007.

Pauly, S., Mutterlose, J., Wray, D.S., 2013. Palaeoceanography of Lower Cretaceous (Barremian–Lower Aptian) black shales from northwest Germany evidenced by calcareous nannofossils and geochemistry. Cretaceous Research 42, 28–43. https://doi.org/10.1016/j.cretres.2013.01.001.

Pictet, A., 2021. New insights on the Early Cretaceous (Hauterivian–Barremian) Urgonian lithostratigraphic units in the Jura Mountains (France and Switzerland): the Gorges de l'Orbe and the Rocher des Hirondelles formations. Swiss Journal of Geoscience 114, 18. https://doi.org/10.1186/s00015-021-00395-5.

Pittet, B., 2006. Les alternances marno-calcaires ou l'enregistrement de la dynamique de production et d'export des plates-formes carbonatées (Habilitation dissertation, Université Claude Bernard Lyon

1), Lyon, France.

Pittet, B., Strasser, A., 1998. Depositional sequences in deep-shelf environments formed through carbonate-mud import from the shallow platform (Late Oxfordian, German Swabian Alb and eastern Swiss Jura). Eclogae Geologicae Helvetiae 91, 149–170.

Pittet, B., Strasser, A., Mattioli, E., 2000. Depositional sequences in deep-shelf environments: a response to sea-level changes and shallow-platform carbonate productivity (Oxfordian, Germany and Spain). Journal of Sedimentary Research 70, 392–407. https://doi.org/10.1306/2DC40918-0E47-11D7-8643000102C1865D.

Pohl, A., Laugié, M., Borgomano, J., Michel, J., Lanteaume, C., Scotese, C.R., Frau, C., Poli, E., Donnadieu, Y., 2019. Quantifying the paleogeographic drivers of Cretaceous carbonate platform development using paleoecological niche modeling. Palaeogeography, Palaeoclimatology, Palaeoecology 514, 222–232. https://doi.org/10.1016/j.palaeo.2018.10.017.

Price, G.D., 1999. The evidence and implications of polar ice during the Mesozoic. Earth-Science Reviews 48, 183–210. https://doi.org/10.1016/S0012-8252(99)00048-3.

Price, G.D., Passey, B.H., 2013. Dynamic polar climates in a greenhouse world: Evidence from clumped isotope thermometry of Early Cretaceous belemnites. Geology 41, 923–926.

Price, G.D., Janssen, N.M.M., Martinez, M., Company, M., Vandevelde, J.H., Grimes, S.T., 2018. A High-Resolution Belemnite Geochemical Analysis of Early Cretaceous (Valanginian-Hauterivian) Environmental and Climatic Perturbations. Geochemistry, Geophysics, Geosystems 19, 3832–3843. https://doi.org/10.1029/2018GC007676.

Quesne, D., Ferry, S., 1994. Correlation de detail entre prismes bioclastiques de plate-forme et cycles marne-calcaire pelagiques (Barremien du SE de la France). Bulletin de la Société Géologique de France, 165, 261-272.

Quesne, D., Ferry, S., 1995. Detailed relationships between platform and pelagic carbonates (Barremian, SE France). Geological Society, London, Special Publications 85, 165–176. https://doi.org/10.1144/GSL.SP.1995.085.01.10.

Ray, D.C., van Buchem, F.S., Baines, G., Davies, A., Gréselle, B., Simmons, M.D., Robson, C., 2019. The magnitude and cause of short-term eustatic Cretaceous sea-level change: A synthesis. Earth-Science Reviews 197, 102901. https://doi.org/10.1016/j.earscirev.2019.102901.

Reboulet, S., 1995. L'évolution des ammonites du Valanginien-Hauterivien inférieur du bassin vocontien et de la plate-forme provençale (Sud-Est de la France) : relations avec la stratigraphie séquentielle et implications biostratigraphiques (Doctoral dissertation, Université Claude Bernard Lyon I). https://www.persee.fr/doc/geoly_0750-6635_1995_mon_137_1_1785.

Reboulet, S., Atrops, F., 1999. Comments and proposals about the Valanginian-Lower Hauterivian ammonie zonation of south-east France. Eclogae Geologicae Helvetiae 92, 183–197. https://doi.org/10.5169/seals-168660.

Reboulet, S., Mattioli, E., Pittet, B., Baudin, F., Olivero, D., Proux, O., 2003. Ammonoid and nannoplankton abundance in Valanginian (early Cretaceous) limestone–marl successions from the southeast France Basin: carbonate dilution or productivity? Palaeogeography, Palaeoclimatology, Palaeoecology 201, 113–139. https://doi.org/10.1016/S0031-0182(03)00541-8.

Reboulet, S., Jaillard, E., Shmeit, M., Giraud, F., Nasrour, M., Spangenberg, J.E., 2022. Biostratigraphy, carbon isotope and sequence stratigraphy of South Tethyan Valanginian successions in the Essaouira-Agadir Basin (Morocco). Cretaceous Research 140, 105341. https://doi.org/10.1016/j.cretres.2022.105341.

Reboulet, S., Szives, O., Aguirre-Urreta, B., Barragán, R., Company, M., Frau, C., Kakabadze, M.V., Klein, J., Moreno-Bedmar, J.A., Lukeneder, A. and Pictet, A., Ploch, I., Raisossadat, S.N., Vašíček, Baraboshkin, E.J., Mitta, V.V., 2018. Report on the 6th International Meeting of the IUGS Lower Cretaceous Ammonite Working Group, the Kilian Group (Vienna, Austria, 20th August 2017). Cretaceous Research 91, 100–110. https://doi.org/10.1016/j.cretres.2018.05.008.

Rio, M., Ferry, S., Cotillon, P., 1989. Périodicités dans les séries pélagiquies alternantes et variations de l'orbitre terrestre. Exemple du Crétacé inférieiur dans le Sud-Est de la France. Comptes rendus de l'Académie des sciences. Série 2, Mécanique, Physique, Chimie, Sciences de l'univers, Sciences de

la Terre 309, 73–79.

Rocha, B.C., Davies, J.H.F.L., Janasi, V.A., Schaltegger, U., Nardy, A.J.R., Greber, D., Lucchetti, A.C.F., Polo, L.A., 2020. Rapid eruption of silicic magmas from the Paraná magmatic province (Brazil) did not trigger the Valanginian event. Geology 48, 1174–1178. https://doi.org/10.1130/G47766.1.

Rudra, A., Sanei, H., Nytoft, H.P., Petersen, H.I., Blok, C., Bodin, S., Bojesen-Koefoed, J.A., 2021. Organic matter characterization of the Lower Cretaceous tight reservoirs in the Danish North Sea. International Journal of Coal Geology 238, 103714. https://doi.org/10.1016/j.coal.2021.103714.

Ruiz-Ortiz, P.A., Bosence, D.W.J., Rey, J., Nieto, L.M., Castro, J.M. and Molina, J.M., 2004. Tectonic control of facies architecture, sequence stratigraphy and drowning of a Liassic carbonate platform (Betic Cordillera, Southern Spain). Basin Research 16, 235–257. https://doi.org/10.1111/j.1365-2117.2004.00231.x.

Sahagian, D., Pinous, O., Olferiev, A. and Zakharov, V., 1996. Eustatic curve for the Middle Jurassic—Cretaceous based on Russian Platform and Siberian stratigraphy: Zonal resolution. AAPG bulletin 80, 1433–1458. https://doi.org/10.1306/64ED9A56-1724-11D7-8645000102C1865D.

Schlager, W., Reijmer, J.J., Droxler, A., 1994. Highstand shedding of carbonate platforms. Journal of Sedimentary Research 64, 270–281. https://doi.org/10.1306/D4267FAA-2B26-11D7-8648000102C1865D.

Sprovieri, M., Coccioni, R., Lirer, F., Pelosi, N., Lozar, F., 2006. Orbital tuning of a lower Cretaceous composite record (Maiolica Formation, central Italy). Paleoceanography 21, PA4212. https://doi.org/10.1029/2005PA001224.

Stein, M., Föllmi, K.B., Westermann, S., Godet, A., Adatte, T., Matera, V., Fleitmann, D. and Berner, Z., 2011. Progressive palaeoenvironmental change during the late Barremian–early Aptian as prelude to Oceanic Anoxic Event 1a: Evidence from the Gorgo a Cerbara section (Umbria-Marche basin, central Italy). Palaeogeography, Palaeoclimatology, Palaeoecology 302, 396–406. https://doi.org/10.1016/j.palaeo.2011.01.025.

Stein, M., Westermann, S., Adatte, T., Matera, V., Fleitmann, D., Spangenberg, J.E., Föllmi, K.B., 2012.

Late Barremian–Early Aptian palaeoenvironmental change: The Cassis-La Bédoule section, southeast France. Cretaceous Research 37, 209–222. https://doi.org/10.1016/j.cretres.2012.03.021.

Strasser, A., 2018. Cyclostratigraphy of shallow-marine carbonates–limitations and opportunities, in: M. Montenari (Ed.), Stratigraphy and Timescales: Cyclostratigraphy and Astrochronology, Vol. 3, Elsevier B.V., Amsterdam, The Netherlands, pp. 151–187. https://doi.org/10.1016/bs.sats.2018.07.001.

Tardif, D., Toumoulin, A., Fluteau, F., Donnadieu, Y., Le Hir, G., Barbolini, N., Licht, A., Ladant, J.-B., Sepulchre, P., Viovy, N., Hoorn, C., Dupont-Nivet, G., 2021. Orbital variations as a major driver of climate and biome distribution during the greenhouse to icehouse transition. Science advances 7, eabh2819. https://doi.org/ 10.1126/sciadv.abh2819.

Thomson, D.J., 1982. Spectrum estimation and harmonic analysis. Proceedings of the IEEE 70, 1055–1096. https://doi.org/10.1109/PROC.1982.12433.

Thomson, D.J., 1990. Quadratic-inverse spectrum estimates: applications to palaeoclimatology. Philosophical Transactions of the Royal Society of London, Series A 332, 539–597. https://doi.org/10.1098/rsta.1990.0130.

Thiede, D.S., Vasconcelos, P.M., 2010. Paraná flood basalts: rapid extrusion hypothesis confirmed by new $^{40}Ar/^{39}Ar$ results. Geology 38, 747–750. https://doi.org/10.1130/G30919.1.

Thierstein, H.R., 1973. Lower Cretaceous calcareous nannoplankton biostratigraphy. Abhandlungen der Geologischen Bundesanstalt 29, 1–52.

Tremolada, F., Erba, E. and Bralower, T.J., 2006. Late Barremian to early Aptian calcareous nannofossil paleoceanography and paleoecology from the Ocean Drilling Program Hole 641C (Galicia Margin). Cretaceous Research 27, 887–897. https://doi.org/10.1016/j.cretres.2006.04.007.

van de Schootbrugge, B., Föllmi, K.B., Bulot, L.G., Burns, S.J., 2000. Paleoceanographic changes during the early Cretaceous (Valanginian–Hauterivian): evidence from oxygen and carbon stable isotopes. Earth and Planetary Science Letters 181, 15–31. https://doi.org/10.1016/S0012-821X(00)00194-1.

van de Schootbrugge, B., Kuhn, O., Adatte, T., Steinmann, P., Föllmi, K.B., 2003. Decoupling of P- and

Corg-burial following Early Cretaceous (Valanginian-Hauterivian) platform drowning along the NW Tethyan margin. Palaeogeography, Palaeoclimatology, Palaeoecology 199, 315–331.

Vaughan, S., Bailey, R.J., Smith, D.G., 2015. Cyclostratigraphy: data filtering as a source of spurious spectral peaks. Geological Society, London, Special Publications, 404, 151-156. https://doi.org/10.1144/SP404.1.

Vera, J.A., 2004. Geología de España. Instituto Geológico y Minero de España, Madrid, España.

Vickers, M.L., Jelby, M.E., Śliwińska, K.K., Percival, L.M., Wang, F., Sanei, H., Price, G.D., Ullmann, C.V., Grasby, S.E., Reinhardt, L., Mather, T.A., Frieling, J., Korte, C., Jerrett, R.M., Jones, M.T., Midtkandal, I., Galloway, J.M., 2023. Volcanism and carbon cycle perturbations in the High Arctic during the Late Jurassic–Early Cretaceous. Palaeogeography, Palaeoclimatology, Palaeoecology 613, 111412. https://doi.org/10.1016/j.palaeo.2023.111412.

Walter, B., 1996. The bryozoan fauna of the Hauterivian transgression in the Paris Basin. Geobios 29, 5–11. https://doi.org/10.1016/S0016-6995(96)80066-0.

Waltham, D., 2015. Milankovitch period uncertainties and their impact on cyclostratigraphy. Journal of Sedimentary Research 85, 990–998. https://doi.org/10.2110/jsr.2015.66.

Weissert, H., Erba, E., 2004. Volcanism, CO_2 and palaeoclimate: a Late Jurassic–Early Cretaceous carbon and oxygen isotope record. Journal of the Geological Society 161, 695–702. https://doi.org/10.1144/0016-764903-087.

Weissert, H., Lini, A., Föllmi, K.B., Kuhn, O., 1998. Correlation of Early Cretaceous carbon isotope stratigraphy and platform drowning events: a possible link? Palaeogeography, Palaeoclimatology, Palaeoecology 137, 189–203. https://doi.org/10.1016/S0031-0182(97)00109-0.

Westermann, S., Duchamp-Alphonse, S., Fiet, N., Fleitmann, D., Matera, V., Adatte, T., Föllmi, K.B., 2013. Paleoenvironmental changes during the Valanginian: new insights from variations in phosphorus contents and bulk-and clay mineralogies in the western Tethys. Palaeogeography, Palaeoclimatology, Palaeoecology 392, 196–208. https://doi.org/10.1016/j.palaeo.2013.09.017.

Westermann, S., Föllmi, K.B., Adatte, T., Matera, V., Schnyder, J., Fleitmann, D., Fiet, N., Ploch, I.,

Duchamp-Alphonse, S., 2010. The Valanginian $\delta^{13}C$ excursion may not be an expression of a global oceanic anoxic event. Earth and Planetary Science Letters 290, 118–131. https://doi.org/10.1016/j.epsl.2009.12.011.

Wilpshaar, M., Leereveld, H., Visscher, H., 1997. Early Cretaceous sedimentary and tectonic development of the Dauphinois Basin (SE France). Cretaceous Research 18, 457–468. https://doi.org/10.1006/cres.1997.0062.

Wissler, L., Weissert, H., Masse, J.P. and Bulot, L., 2002. Chemostratigraphic correlation of Barremian and lower Aptian ammonite zones and magnetic reversals. International Journal of Earth Sciences 91, 272–279. https://doi.org/10.1007/s005310100210.

Wortmann, U.G., Weissert, H., 2000. Tying platform drowning to perturbations of the global carbon cycle with a $\delta^{13}C_{Org}$-curve from the Valanginian of DSDP Site 416. Terra Nova 12, 289–294. https://doi.org/10.1046/j.1365-3121.2000.00312.x.

Wulff, L., Mutterlose, J., Bornemann, A., 2020. Size variations and abundance patterns of calcareous nannofossils in mid Barremian black shales of the Boreal Realm (Lower Saxony Basin). Marine Micropaleontology 156, 101853. https://doi.org/10.1016/j.marmicro.2020.101853.

Yilmaz, I.O., Altiner, D., Tekin, U.K., Ocakoglu, F., 2012. The first record of the "Mid-Barremian" Oceanic Anoxic Event and the Late Hauterivian platform drowning of the Bilecik platform, Sakarya Zone, western Turkey. Cretaceous Research 38, 16–39. https://doi.org/10.1016/j.cretres.2012.04.010.

Zhang, Y., Ogg, J.G., Minguez, D., Hounslow, M.W., Olaussen, S., Gradstein, F.M., Esmeray-Senlet, S., 2021. Magnetostratigraphy of U-Pb–dated boreholes in Svalbard, Norway, implies that magnetochron M0r (a proposed Barremian-Aptian boundary marker) begins at 121.2 ± 0.4 Ma. Geology 49, 733–737. https://doi.org/10.1130/G48591.1.

Zhu, D.C., Chung, S.L., Mo, X.X., Zhao, Z.D., Niu, Y., Song, B., Yang, Y.H., 2009. The 132 Ma Comei-Bunbury large igneous province: Remnants identified in present-day southeastern Tibet and southwestern Australia. Geology 37, 583–586. https://doi.org/10.1130/G30001A.1.

Figure captions

Fig. 1. Time scale calculated here of stages, substages, Tethyan ammonite zones, calcareous nannofossil zone, magnetochrons, orbital cycles, composite $CaCO_3$ series and various $\delta^{13}C_{carb}$ series

Fig. 2. A. Paleogeographic map of the Early Cretaceous with locations of the Late Jurassic and Early Cretaceous continental rifts (Frizon de Lamotte et al., 2015). Abbreviations: NB: Neuquén Basin, SD: Subbetic Domain, VB: Vocontian Basin. **B.** Map of the Neuquén Basin with location of the El Portón section. **C.** Map of the Vocontian Basin with location of the La Charce-Pont-Lemerol section and other sections mentioned. **D.** Map of the Betic Range with location of the Río Argos section and other mentioned sections. **E.** Detail of the El Portón section showing the tuff layer dated within the marl-limestone alternations. **F.** Detail of the marl-limestone alternations of the La Charce section. **G.** Details of the marl-limestone alternations of the Río Argos section. Abbreviations: Prec.: Precession; Obl.: Obliquity.

Fig. 3. Behavior of Magnetic Susceptibility (MS), CaCO3 content d13C and clay mineral assemblage over several marl-limestone alternations of the Vergol section (up; from Martinez et al. (2020b) and the Río Argos section (down; from Martinez et al., 2012; Moiroud et al., 2012).

Fig. 4. Cross plots between the MS, CaCO3 content and clay species content. **From A to E**: data from Vergol-Morénas (Martinez et al., 2020b). **From F to I**: data from Río Argos (Martinez et al., 2012; Moiroud et al., 2012). The blue line indicates the best fit and the red lines the 95 % confidence intervals.

Fig. 5. $\delta^{13}C$, Gamma-Ray Total Count (GRTC), Magnetic Susceptibility (MS) and clay mineral assemblages from the Vergol-Morénas section. The $\delta^{13}C$ data are from Gréselle et al. (2011), Kujau et al. (2012), Martinez et al. (2020b). The two pictures to the right are from Vergol-Morénas.

Fig. 6. Examples of bundles and beds used are correlation markers throughout the Vocontian Basin. **A.** The

Sayni Marl Interval (Upper Hauterivian) at La Charce section. Beds numberd are labelled according to Martinez et al. (2013) following Reboulet and Atrops (1999) numbering scheme. **B.** Furcillata Marl Interval and Radiatus Bundle at the Valanginian-Hauterivian boundary of the La Charce section. **C.** Bentonite O3 in the *N. neocomiensiformis* Tethyan Ammonite Zone (Lower Valanginian) at the Angles section. Bed number is from Busnardo et al. (1979). **D.** Close-up view of bentonite O3. **E.** View of the Otopeta Bundle at the Vergol ection. Bed number is from Kenjo et al. (2021). **F.** View of the Otopeta Bundle at the Reynier section. Note the interval of more difficult outcropping conditions due to increase of clay content. This outcropping condition is also observed at Vergol.

Fig. 7. Correspondance between the Gamma-Ray Total Count (GRTC) signal, the 405-kyr eccentricity cycles and the lithology in the Pronecostatum, Median and Nicklesi bundles (Upper Valanginian) of the La Charce section. Ammonite zonation is from Bulot et al. (1992) and Reboulet and Atrops (1999). Calcareous nannofossil biostratigraphy is from Barbarin et al. (2012).

Fig. 8. Correspondance between the Gamma-Ray Total Count (GRTC) signal, the 405-kyr, 100-kyr eccentricity cycles and the lithology in the Radiatus Bundle (Lower Hauterivian) of the La Charce section. Bed number and biostratigraphy are available in Mutterlose et al. (2021).

Fig. 9. Biostratigraphic framework of the Berriasian-Valanginian transition. Ammonite and calcareous nannofossil data are from Kenjo et al. (2021). Calcareous nannofossil and calpionellid data are from Charbonnier et al. (2013). The Gamma-Ray Total Count (GRTC) data is from Martinez et al. (2013) and the Magnetic Susceptibility data (MS) is from Charbonnier et al. (2013). The ammonite zonation at Reynier and Orpierre is extrapolated from Vergol by correlation of GRTC and MS signals. Boundaries of calcareous nannofossil zone boundaries are located at the FAD or LAD of the index species within the Vocontian Basin, determined by correlation of GRTC and MS signals.

Fig. 10. Biostratigraphic framework of the analysed sections from the lower Valanginian to the lower Hauterivian. Ammonite data are from Bulot et al. (1992), Reboulet (1995), Reboulet and Atrops (1999) and Mutterlose et al. (2021). Calcareous nannofossil data are from Duchamp-Alphonse et al. (2007), Gréselle et al. (2011), Barbarin et al. (2012) and Charbonnier et al. (2013). The boundaries of the ammonite and calcareous nannofossil zones are fixed at the FO or LO of the considered species index in the Vocontian Basin and corralted to the other sections using the Gamma-Ray Total Count (GRTC) and Magnetic Susceptibility (MS) signals. The GRTC signals are from Martinez et al. (2013). The MS signal is from Charbonnier et al. (2013).

Fig. 11. Biostratigraphic framework of the analysed sections from the upper Valanginian to the lower Barremian in the Neuquén Basin, Vocontian Basin and Subbetic Domain. The ammonite data are from Bulot et al. (1992), Reboulet and Atrops (1999), Aguirre-Urreta et al. (2019), Hoedemaeker and Leereveld (1995) and Company et al. (2003). The calcareous nannofossil data are from Thierstein (1973), Gardin (2008), Hoedemaeker and Leereveld (1995) and Company et al. (2005) and Aguado et al. (2014). The pink star at El Portón indicates the stratigraphic location of a CA-ID-TIMS U-Pb age on zircons from Aguirre-Urreta et al. (2017).

Fig. 12. Biostratigraphic framework from the upper Hauterivian to the lowermost Aptian. The ammonite data are from Aguado et al. (2014) and calcareous nannofossil data from Aguado et al. (2014, 2022).

Fig. 13. Correlation of the astrochronologic frameworks in the lower part of the Valanginian series. The $\delta^{13}C_{bulk}$ data of Vergol is from Gréselle et al. (2011), Kujau et al. (2012), Martinez et al. (2020b). The $\delta^{13}C_{bulk}$ data from Orpierre is from Charbonnier et al. (2013).

Fig. 14. 2π-Multi-Taper (MTM) of the direct signals and amplitude modulation of the precession cycles from Reynier (**A-D**), Angles (**E-H**), Vergol-Morénas (**I-L**) and Orpierre (**M-P**). Periods are lebelled in

meters above correspondant spectral peaks. ecc.: eccentricity, obl.: obliquity, prec.: precession.

Fig. 15. Correlation of the astrochronologic frameworks from the lower Valanginian to the lower Hauterivian. The $\delta^{13}C_{bulk}$ from La Charce is from Gréselle et al. (2011), Hennig et al. (1999) and van de Schootbrugge et al. (2000). The $\delta^{13}C_{bulk}$ from Angles is from Duchamp-Alphonse et al. (2007). The $\delta^{13}C_{bulk}$ from Orpierre is from Charbonnier et al. (2013).

Fig. 16. 2π-Multi-Taper (MTM) spectra of the direct signals and amplitude modulation of the precession cycles from Orpierre (**A-B**), Angles (**C-D)** and La Charce (**E-F**). Periods are labeled in meters above the correspondant spectral peak. ecc.: eccentricity, obl.: obliquity, prec.: precession.

Fig. 17. Correlation of the astrochronologic frameworks from the upper Valanginian to the lowermost Barremian. Magnetic Susceptibility data (MS) is from Aguirre Urreta et al. (2019). Gamma-Ray Total Count data (GRTC) are from Martinez et al. (2013, 2015).

Fig. 18. 2π-Multi-Taper (MTM) spectra of GRTC signals and amplitude modulation of the precession cycles from Río Argos (**A-F**) and La Charce Pommerol (**G-H**). Periods are labeled in meters; ecc.: eccentricity, obl.: obliquity, prec.: precession.

Fig. 19. Correlation of the astrochronologic frameworks from the upper Hauterivian to the lowermost Aptian. Magnetic Susceptibility data (MS) is from Martinez et al. (2020a).

Fig. 20. 2π-Multi-Taper (MTM) spectra of MS signals and amplitude modulation of the precession cycles from Arroyo Gilico (**A-B**) and Barranco de Cavila (**C-D**). Periods are labeled in meters; ecc.: eccentricity, obl.: obliquity, prec.: precession.

Fig. 21. Cross-plots between the $CaCO_3$ and equivalent GRTC series from (**A.**) the Angles section and (**B.**) the Río Argos section. The solid blue line corresponds to the best-fit linear regression and the dashed red lines to the 95 % confidence intervals.

Fig. 22. Construction of the spliced $CaCO_3$ series from the Vocontian Basin and the Subbetic Domain. **A.** GRTC series from Reynier, Vergol-Morénas, Angles, La Charce-Pommerol and Río Argos calibrated into time. **B.** MS series from the Orpierre section. **C.** $CaCO_3$ content series from Río Argos X.Ag-1, Arroyo Gilico and Barranco Cavila calibrated into time. **D.** $CaCO_3$-equivalent series from Reynier, Vergol-Morénas, Angles, La Charce-Pommerol and Río Argos together with $CaCO_3$ series from Río Argos X.Ag-1, Arroyo Gilico and Barranco Cavila calibrated into time. The vertical bars represent where the various series are cut to build the composite series. **E.** Composite $CaCO_3$ series.

Fig. 23. Evolutive spectral analysis of the $\delta^{13}C_{bulk}$ series from the Vocontian Basin calibrated to time (periods are labeled in Myr) and correlation of this series to the $\delta^{13}C_{bulk}$ from the Maiolica Formation (Umbria-Marche; Sprovieri et al., 2006).

Fig. 24. Evolutive spectral analysis of the $\delta^{13}C_{bel}$ series from western Tethys calibrated to time. Periods are labeled in Myr.

Fig. 25. Evolutive spectral analysis of the $\delta^{13}C_{bulk}$ series from the Subbetic Domain calibrated to time. Periods are labeled in Myr.

Fig. 26. 2π-Multi-Taper (MTM) spectra (**A.**) the composite $CaCO_3$ series, (**B.**) the compiled $\delta^{13}C_{bulk}$ series from the Vocontian Basin, (**C.**) the compiled $\delta^{13}C_{bel}$ series, (**D.**) the $\delta^{13}C_{bulk}$ series from the Subbetic Domain, (**E.**) the $\delta^{13}C_{bulk}$ series from the Umbria-Marche Basin. The periods are labeled in Myr.

Fig. 27. Evolutive spectral analysis of the $\delta^{13}C_{bulk}$ series from the Umbria-Marche calibrated to time.

Periods are labeled in Myr.

Table 1. Age models of the different sections studied

Label	Numerical age (Ma)	Bed no Barranco Cavila	Level Barranco Cavila (m)	Bed no Arroyo Gilico	Level Arroyo Gilico (m)	Bed no Rio Argos	Level Rio Argos (m)	Bed no La Charce-Pommerol	Level La Charce-Pommerol (m)	Bed no Angles	Level Angles (m)	Bed no Orpierre	Level Orpierre (m)	Bed no Vergol-Morénas	Level Vergol-Morénas (m)	Bed no Reynier	Level Reynier (m)
Base.A1	**120.91**	marl BC101b-102	67.12														
Base.BA	**121.31**	marl BC98-98b	58.56														
Base.B10	**121.72**	marl BC94-95	49.89														
Base.B9	**122.12**	marl BC87-88	42.17														
Base.B8	**122.53**	marl BC81b-81c	28.26														
Base.B7	**122.93**	marl BC75-76	16.34														
Base.B6	**123.34**	marl BC71-72	11.61	marl AG84-85	71.90												
Base.B5	**123.74**	marl BC65-66	4.88	marl AG71-72	65.13												
Base.B4	**124.15**			marl AG67-68	61.60												
Base.B3	**124.55**			limestone AG52	51.75												
Base.B2	**125.96**			limestone AG38	41.64												
Base.B1	**125.36**			marl AG28-29	31.24	marl RA185-186	1[illegible]4.67										
Base.HB	**125.77**			marl AG15-16	24.45	mar[illegible] RA170[illegible] -170c	1[illegible]2.67										
Base.H13	**126.17**			marl AG8-9	18.08	ma[illegible] [illegible]155-156	129.27										
Base.H12	**126.58**			marl AG minus1-1	11.6	marl RA5 11-12	117.87										
Base.H11	**127.98**			marl AG minus1[illegible] minus16	-0.60	marl RA137-138	104.07										
Base.H10	**127.38**					limestone RA118	86.47										
Base.H9	**127.79**					marl RA105-106	73.47	marl LCP 375b-376	226.63								
Base.H8	**128.20**					marl RA89-90	51.87	marl LCP 313-314	208.92								
Base.H7	**128.60**					marl RA73-74	33.47	marl LCP 297-298	195.65								
Base.H6	**129.01**					marl RA55-56	14.07	marl LCP 279-280	182.42								
Base.H5	**129.41**							limestone LCP259	165.63								
Base.H4	**129.82**							marl LCP 241K-241L	148.50								
Base.H3	**130.22**							marl LCP231-232	132.58								
Base.H2	**130.63**							marl LCP215H-	116.46								

					215i												
Base.H1	**131.03**				limestone LCP203	98.24											
Base.VH	**131.44**				marl LCP180-181	76.48	marl A373-374	206.25	marl Orp800-801	223.51							
Base.V13	**131.84**				limestone LCP166a	60.92	limestone 361a	188.87	limestone Orp 763	206.37							
Base.V12	**132.25**				limestone LCP156a	48.02	limestone A354a	174.85	limestone Orp727	187.88							
Base.V11	**132.65**				marl LCP136-138	34.30	marl A342-343a	156.72	marl Orp697-69[illegible]	170.87							
Base.V10	**133.06**				limestone LCP128	25.57	limestone 338a	147.00	limestone Orp662	153.56							
Base.V9	**133.46**				marl LCP109-110	8.30	marl A321-322a	24.44	marl Orp613-614	129.25	marl VM118b-118c	148.60	marl R190c-191	130.42			
Base.V8	**133.87**						marl 306b-307	105.01	marl Orp598-599	112.76	marl VM107c-108	124.17	limestone R171	111.42			
Base.V7	**134.27**						marl A303c-303d	85.74	N.A.	96.11	marl V.VM97f-98	97.81	marl R156-157	94.82			
Base.V6	**134.68**						marl A296a-296b	71.20	marl Orp567-568	88.59	marl VM90-91	87.19	marl R143-144	81.52			
Base.V5	**135.08**						limestone A281	53.29	limestone Orp539	71.83	limestone VM75b	71.48	limestone R123	63.45			
Base.V4	**135.49**						limestone A259	35.00	limestone Orp526	52.65	limestone VM56	55.12	limestone R102	45.95			
Base.V3	**135.89**								marl Orp498-499	37.03	marl V.VM35-36	33.40	marl R76-77	32.25			
Base.V2	**136.30**								limestone Orp481	25.40	limestone V.VM16	21.15	limestone R57	22.05			
Base.V1	**136.70**								limestone Orp456	16.54	limestone VM3	13.98	limestone R38	13.05			
Base.BV	**137.11**								marl Orp427-428	9.25	marl B.VM134-135	4.95	marl R15-16	3.05			

Table 2. Calculated age of the ammonite zones. The selected age is from the Reynier section from the base of the series to 134.69 Ma, from Vergol-Morénas from 134.69 to 133.68 Ma, from Orpierre from 133.68 to 132.26 Ma, from La Charce-Pommerol from 132.26 to 127.82 Ma, from Río Argos from 127.82 to 126.79 Ma, from Arroyo Gilico from 126.79 to 123.97 Ma and from Barranco Cavila from 123.97 Ma to the top of the series.

Biochron	Age Barranco Cavila (Ma)	Age Arroyo Gilico (Ma)	Age Río Argos (Ma)	Age La Charce-Pommerol (Ma)	Age Angles (Ma)	Age Orpierre (Ma)	Age Vergol-Morénas (Ma)	Age Reynier (Ma)	Selected age (Ma)	Comment
Base Forbesi Zone	120.95								120.95	
Base Oglanlensis Zone	**121.15**								**121.15**	**Base Aptian**
Base Sarasini Zone	121.85								121.85	
Base Giraudi Zone	122.01								122.01	
Base Feraudianus Subzone	*122.33*								*122.33*	
Base Provincialis Subzone	*122.57*								*122.57*	
Base Sartousiana Zone	122.96								122.96	
Base Alpinum Subzone	*123.39*	*123.48*							*123.48*	
Base Vandenheckii Zone		**124.05**							**124.05**	**Base Late Barremian**
Base Moutonianum Zone		124.42							124.42	
Base Cailladiscus Subzone		*124.56*							*124.56*	
Base Compressissima Zone / Fallax Subzone		124.72							124.72	
Base Pulchella Zone		124.93							124.93	
Base Nicklesi Zone		125.15	125.17						125.15	
Base Colombiana Subzone		*125.42*	*125.44*						*125.42*	
Base Hugii Zone		**125.71**	**125.74**						**125.71**	**Base Barremian**
Base Picteti Subzone		*126.15*	*126.15*						*126.15*	

Base Mortilleti/Catulloi Subzone	*126.45*	*126.39*					*126.45*	
Base Ohmi Zone	126.52	126.47					126.52	
Base Angulicostata / Seitzi Subzone	*126.69*	*126.63*					*126.69*	
Base Krenkeli Subzone	*126.96*	*126.94*					*126.94*	
Base Binelli Subzone		*127.03*					*127.03*	
Base Balearis Zone		127.25					127.25	
Base Ligatus Zone		128.06	128.06				128.06	
Base Sayni Zone		**129.19**	**129.10**				**129.10**	**Base Late Hauterivian**
Base Nodosoplicatum Zone			129.[illegible]				129.95	
Base Jeannoti Subzone			*130.22*				*130.22*	
Base Loryi Zone			130.46				130.46	
Base Radiatus Zone			**131.25**	**131.12**			**131.25**	**Base Hauterivian**
Base Callidiscus Subzone			*131.41*	*131.39*	*131.41*		*131.41*	
Base Furcillata Zone			131.92	131.92	132.01		131.92	
Base Nicklesi Subzone			*132.83*	*132.85*	*132.91*		*132.91*	
Base Peregrinus Zone			133.35	133.36	133.36	133.34	133.36	
Base Pronecostatum Subzone				*133.70*	*133.72*	*133.73*	*133.71*	*133.73*	
Base Verrucosum Zone				**134.16**	**134.18**	**134.20**	**134.18**	**134.20**	**Base Late Valanginian**
Base Platycostatus Subzone				*134.52*	*within slump*	*134.53*	*134.52*	*134.53*	
Base Inostranzewi Zone				134.83	134.86	134.82	134.82	134.82	
Base Neocomiensiformis Zone					135.85	135.86	135.85	135.85	
Top Premolicus Subzone					*136.35*	*136.36*	*136.34*	*136.34*	
Base Pertransiens Zone					**137.06**	**137.08**	**137.06**	**137.06**	**Base Valanginian**

Table 3. Calculated age of the calcareous nannofossil zones. The selected age is from the Reynier section from the base of the series to 134.69 Ma, from Vergol-Morénas from 134.69 to 133.68 Ma, from Orpierre from 133.68 to 132.26 Ma, from La Charce-Pommerol from 132.26 to 127.82 Ma, from Río Argos from 127.82 to 126.79 Ma, from Arroyo Gilico from 126.79 to 123.97 Ma and from Barranco Cavila from 123.97 Ma to the top of the series.

Base nannofossil zone	Age Barranco Cavila (Ma)	Age Arroyo Gilico (Ma)	Age Rio Argos (Ma)	Age La Charce-Pommerol (Ma)	Age Angles (Ma)	Age Orpierre (Ma)	Age Vergol-Morénas (Ma)	Age Reynier (Ma)	Selected Age (Ma)
NC6A2	121.71								121.71
NC6A1	122.21								122.21
NC5E3	122.39								122.39
NC5E2	123.33	123.32							123.33
NC5E1		124.47							124.47
NC5D		124.97							124.97
NC5C		126.37	126.39						126.37
NC5B			127.22						127.22
NC5A			128.34	128.34					128.34
NC4B				130.09					130.09
NC4A				132.00	132.03	132.09			132.00
NK3B					133.98	133.99	134.01	133.99	134.01
NK3A						136.88	136.88	136.85	136.85

Table 4. Calculated ages of the ammonite zones in the Berriasian Stage. The durations of the ammonite zones in the Berriasian are the same as in the Geologic Time Scale 2020.

Base zones in Berriasian	Age.Ma
"Thurmanniceras" Otopeta Subzone	*137.49*
***Tirnovella alpillensis* Zone**	**137.95**
Berriasella picteti Subzone	*138.54*
***Fauriella boissieri* Zone / *Malbosiceras paramimounum* Subzone**	**139.39**

Table 5. Age model of the correlations between the carbon-isotope curves between the composite Vocontian and the composite Umbria-Marche basins.

Level Maiolica (m)	Age Vocontian and Subbetic (Ma)
336.82	121.19
330.58	121.78
319.44	122.54
290.52	124.72
273.69	125.41
259.75	126.74
233.28	128.30
195.98	131.01
191.98	131.65
180.82	132.23
165.80	132.81
147.98	133.95
136.70	134.52
123.04	135.10
113.64	135.92
89.62	137.46

Table 6. Calculated ages of magnetochrons in the Maiolica Formation. Levels are from Sprovieri et al. (2006).

Base magnetochron	Level (m)	Absolute age (Ma)
C34n	333.93	121.13
M0r	332.55	121.40
M1n	311.13	123.17
M1r	306.55	123.51
M3n	295.42	124.35
M3r	269.83	125.78
M5n	256.96	126.90
M5r	250.31	127.30
M6n	248.25	127.42
M6r	245.8	127.56
M7n	243.35	127.71
M7r	235.18	128.19
M8n	233.39	128.29
M8r	229.16	128.60
M9n	225.58	128.86
M9r	217.68	129.43
M10n	212.24	129.83
M10r	207.38	130.18
M10Nn.1n	201.04	130.64
M10Nn.1r	199.8	130.73
M10Nn.2n	195.01	131.17
M10Nn.2r	194.08	131.31
M10Nn.3n	188.05	131.85
M10Nr	182.61	132.14
M11n	168.69	132.70
M11r.1r	159.67	133.20

Table 7. Age of bioevents in the Maiolica Formation and comparison with the Vocontian Basin and Subbetic Domain

Age Model Maiolica	Comparison Vocontian and Subbetic

Event	Depth (m)	Age (Ma)	Age (Ma)	Absolute difference in age (Ma)
FO R. irregularis	327.23	122.01	121.91	0.10
LO C. oblongata	274.37	125.38	124.97	0.41
Base T. hugii	265.87	126.16	125.71	0.45
LO L. bollii	262.83	126.45	126.37	0.08
FO R. terebrodentarius	236.73	128.10	127.22	0.88
LO C. cuvillieri	230.68	128.49	128.34	0.15
FO L. bollii	208.50	130.10	130.09	0.01
Base A. radiatus	194.23	131.29	131.25	0.04
FO N. bucheri	183.05	132.11	131.49	0.62
LO T. verenae	172.70	132.54	132.00	0.54
LO R. wisei	130.45	134.79	134.01	0.78
FO T. verenae	101.73	136.68	136.74	0.06
Base T. pertransiens	95.83	137.06	137.06	0.00

Table 8. Calculated ages of the climatic events. The selected age is from the Reynier section from the base of the series to 134.69 Ma, from Vergol-Morénas from 134.69 to 133.68 Ma, from Orpierre from 133.68 to 132.26 Ma, from La Charce-Pommerol from 132.26 to 127.82 Ma, from Río Argos from 127.82 to 126.79 Ma, from Arroyo Gilico from 126.79 to 123.97 Ma and from Barranco Cavila from 123.97 Ma to the top of the series.

Event	Age Barranco Cavila (Ma)	Age Arroyo Gilico (Ma)	Age Rio Argos (Ma)	Age La Charce-Pommerol (Ma)	Age Reynier (Ma)	Age Vergol-Morénas (Ma)	Age Orpierre (Ma)	Age Angles (Ma)	Selected age (Ma)	Duration between events (Myr)
Top Taxy	121.19								121.19	
Base d13C Taxy anomaly	121.74								121.74	
Base Taxy	122.07								122.07	2.42
Top MBE		124.04							124.04	
Base MBE		124.49							124.49	2.02
Top Faraoni		126.39	126.36						126.39	
Base Faraoni		126.51	126.46						126.51	2.67
Top Mid Hauterivian Event			128.70	128.71					128.71	
Base Mid Hauterivian Event			129.24	129.18					129.18	2.40
Top End Valanginian Event				131.46				131.44	131.46	
Base End Valanginian Event				131.58				131.58	131.58	2.38
Top climax Weissert					133.74	133.75		133.72	133.75	
Base climax Weissert					133.97	133.96		133.96	133.96	2.52
Base Weissert					134.56	134.58		134.56	134.56	
Top Early Valanginian Event					136.11	136.18			136.11	
Base Early Valanginien Event					136.85	136.90			136.85	

Declaration of interests

☒The authors declare that they have no known competing financial interests or personal relationships that could have appeared to influence the work reported in this paper.

☐The authors declare the following financial interests/personal relationships which may be considered as potential competing interests:

Graphical abstract

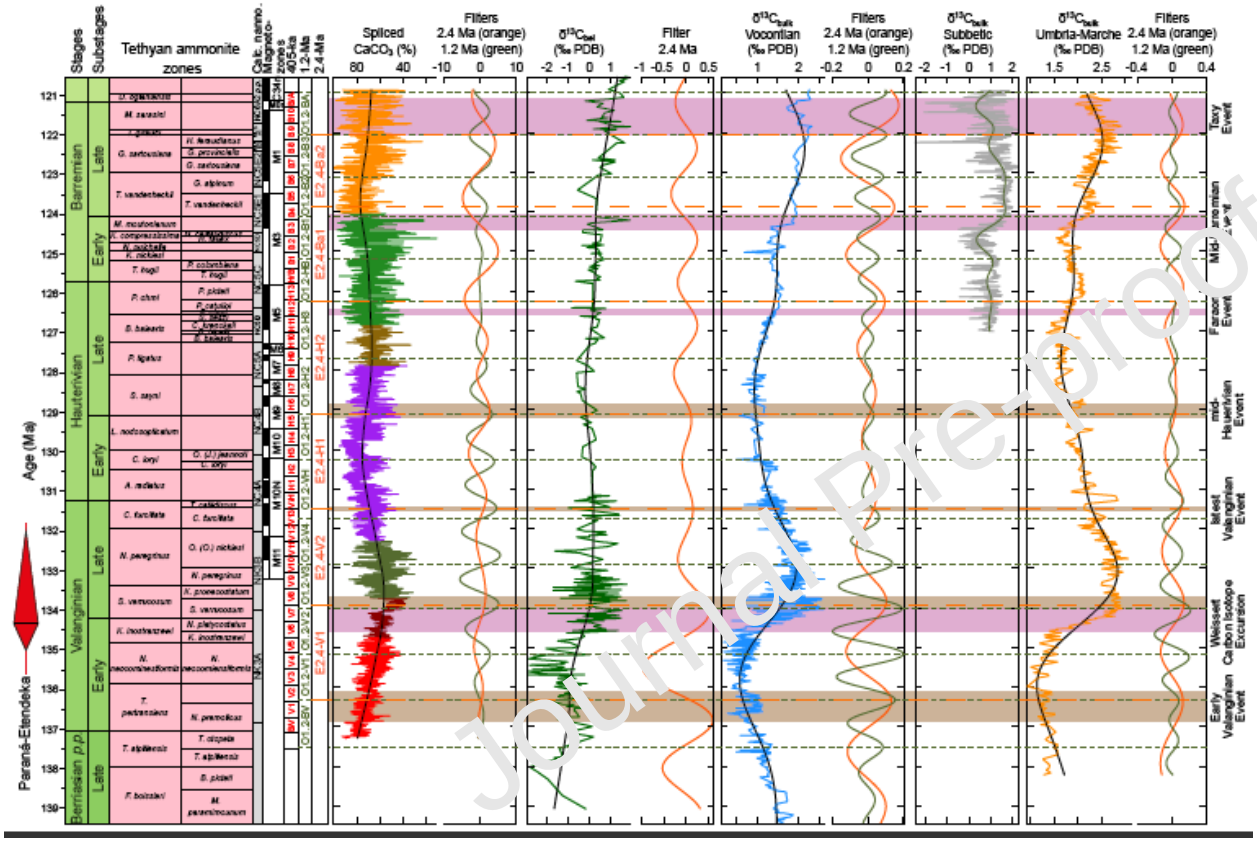

- New time scale proposed from the Valanginian to the Barremian
- Onset of the Weissert Event synchronous to the Paraná-Etendeka Large Igneous Province
- Control of long obliquity and eccentricity on detrital and carbon cycles